

# Plasma Synthetic Jet Actuator

From characterisation to separation flow control.

T. van Pelt

Technische Universiteit Delft



# Plasma Synthetic Jet Actuator

From characterisation to separation flow control.

by

**T. van Pelt**

in partial fulfilment of the requirements for the degree of

**Master of Science**  
Aerodynamics

at the Delft University of Technology,  
to be defended publicly on Friday February 1, 2019 at 03:00 PM.

Supervisor:	Dr. M. Kotsonis	TU Delft
Thesis committee:	Dr. ir. Bas van Oudheusden,	TU Delft
	Dr. ir. W.-P. Breugem,	TU Delft
	Dr. ir. H. Zong,	TU Delft

*This thesis is confidential and cannot be made public until February 1, 2019.*

An electronic version of this thesis is available at <http://repository.tudelft.nl/>.



# ABSTRACT

*Timo van Pelt*

*Plasma Synthetic Jet Actuator: From Characterisation to Separation Flow Control.*

*Supervisors: M. Kotsonis & H. Zong*

This project proposes a series of experiments that involve plasma synthetic jet actuators. The first experiment will perform a jet characterisation experiment that will research the effect of orifice geometry on the overall performance of the actuator. The second experiment will be built upon the first experiment and will use a plasma synthetic jet array to combat leading edge separation of a NACA 0015 airfoil at  $Re = 1.7 \cdot 10^5$  and  $U_\infty = 10 \text{ m/s}$  and improve the overall performance of this particular airfoil. Special focus will be put in uncovering the underlying mechanics of plasma synthetic jet actuation operating in leading edge separation conditions and how performance is dependent on the actuation frequency.

From the jet characterisation experiments a clear performance trend of actuator efficiency with respect to the converging cone angle  $\theta$  is found. The optimal optimal orifice angle is expected to lie between  $45^\circ < \theta < 69^\circ$ . These geometries experience  $\sim 20\%$  higher jet velocities than the baseline ‘straight’ orifice, which results in larger mass expulsions and an overall more efficient operation of the actuator. Additionally it is found that adding a small diverging section to the orifice improves upon the electro-mechanical efficiency of the plasma synthetic jet actuator. PIV measurements show that this is due to the increased effective orifice area which allows for higher mass flows through the orifice but also the jet velocities remained of similar order as the optimal converging geometries.

The flow control experiments show that plasma synthetic jet actuators can indeed improve the performance of a NACA 0015 airfoil at  $Re = 1.7 \cdot 10^5$  and  $U_\infty = 10 \text{ m/s}$ . The force balance measurements show that PSJ actuation suppresses the hysteresis loop present when actuation is absent. Furthermore the angle at which maximum lift is achieved is shifted by  $\sim 7^\circ$  increasing the maximum achieved lift by  $\sim 23\%$ . Additionally, flow separation can be delayed by about  $2^\circ$  reducing the drag by about  $\sim 40\%$ . Furthermore, the PIV measurements show the mechanisms behind flow separation control. At moderate stall angles flow reattachment is feasible if the actuation frequency is high enough. At higher angles of attack the separation point moves upstream of the actuators and renders the array incapable to suppress flow separation. However, at these conditions the actuators are still able to influence the separation region and higher frequencies, with an optimum of  $F^* = 1$ , are capable to suppress the separation area more.

If the above-mentioned experiments translate to aeronautical applications plasma synthetic jets might be a game changer when it comes to demanding flight conditions. Not only is plasma synthetic jet actuation capable of diminishing the hysteresis effect it is also capable of considerably increasing the lift and decreasing the drag forces. These effects can considerably improve the safety of aircraft as the omission of hysteresis can reduce unwanted unsteady loads that advance structural fatigue and the higher lift coefficients reduce the need of high lift devices allowing them to become smaller and less complex in the future. Overall this allows aircraft to fly at more demanding flight conditions than previously feasible.



To my parents who have supported me, my studies and my travels for all these years.



# ACKNOWLEDGEMENTS

This thesis owes a lot of thanks to many people. First and foremost I want to thank Haohua Zong as my daily supervisor. Your help has been priceless especially during the experiments and I have learnt a lot from my time with you.

I would also like to thank Marios Kotsonis who, as my thesis supervisor, had to deal with the chaos that comes when your student pursues two separate master studies.

My thanks also goes to Ruud van Luijk who has proofread this thesis and helped getting many errors out of my text and never forget my parents who have funded me all those years.

My last thanks goes to all my friends and family that have been part of my life during my studies and supporting my any way feasible. Life has been very joyful with you all around me to distract me from my student tasks.

Thank you all.



# Contents

<b>ABSTRACT</b>	<b>iii</b>
<b>ACKNOWLEDGEMENTS</b>	<b>vii</b>
<b>List of Figures</b>	<b>xi</b>
<b>List of Tables</b>	<b>xv</b>
<b>I Literature survey.</b>	<b>1</b>
<b>1 Literature survey.</b>	<b>3</b>
1.1 Flow control devices. . . . .	4
1.1.1 Passive flow control. . . . .	4
1.1.2 Active flow control. . . . .	6
1.2 Plasma Synthetic Jet Actuators. . . . .	13
1.2.1 Basic discharge . . . . .	13
1.2.2 PSJA geometries. . . . .	14
1.3 Knowledge gaps. . . . .	17
1.3.1 PSJA characterisation. . . . .	17
1.3.2 Flow separation control experiment. . . . .	17
1.4 Thesis lay-out. . . . .	18
<b>II PSJA characterisation.</b>	<b>19</b>
<b>2 Methodology.</b>	<b>21</b>
2.1 Measurement techniques. . . . .	21
2.1.1 PIV measurements. . . . .	21
2.1.2 Electrical measurements. . . . .	21
2.2 Experimental setup. . . . .	21
2.2.1 Actuator model. . . . .	22
2.2.2 Electrical circuit. . . . .	22
2.3 Post processing. . . . .	23
<b>3 Results.</b>	<b>25</b>
3.1 Phase averaged velocity fields. . . . .	25
3.2 Jet parameters. . . . .	30
<b>4 Conclusion</b>	<b>35</b>
<b>III PSJA separation control.</b>	<b>37</b>
<b>5 Methodology.</b>	<b>39</b>
5.1 Measurement techniques. . . . .	39
5.1.1 Force balance measurements. . . . .	39
5.1.2 PIV measurements. . . . .	39
5.1.3 Electrical measurements. . . . .	40
5.2 Experimental setup. . . . .	40
5.2.1 Electrical circuit. . . . .	40
5.2.2 Model. . . . .	42
5.3 Post processing. . . . .	45
5.3.1 Force balance corrections. . . . .	45
5.3.2 PIV. . . . .	46

---

<b>6</b>	<b>Results.</b>	<b>47</b>
6.1	Force balance measurements. . . . .	47
6.1.1	First experiment. . . . .	47
6.1.2	Second experiment. . . . .	48
6.1.3	The effect of PSJA density and placement. . . . .	51
6.1.4	Power consumption and the effect of duty cycle. . . . .	52
6.2	PIV results. . . . .	53
6.2.1	Time averaged velocity fields for the baseline cases. . . . .	53
6.2.2	Leading edge separation control at $\alpha = 15.5^\circ$ (upstream actuation). . . . .	54
6.2.3	Leading edge separation control at $\alpha = 22^\circ$ (downstream actuation). . . . .	59
6.2.4	Startup and quenching process of PSJ actuation. . . . .	64
6.2.5	Increasing the free stream velocity. . . . .	66
<b>7</b>	<b>Conclusion.</b>	<b>69</b>
	<b>Bibliography</b>	<b>71</b>

# List of Figures

1.1	Different approach strategies. . . . .	3
1.2	Classification of passive flow control techniques according to Joshi and Gujarathi [26]. . . . .	5
1.3	Example of a Gurney flap. . . . .	5
1.4	Basic principle of vortex generators according to Joshi and Gujarathi [26]. . . . .	6
1.5	Classification of active flow control techniques according to Cattafesta and Sheplak [7]. . . . .	7
1.6	Varying large scale structures at various actuation frequencies and $U_j > U_\infty$ [29]. The dotted line is the modulated flow by the jet. . . . .	11
1.7	Three different phases in a PSJA cycle. . . . .	13
1.8	Losses experienced during PSJ actuation according to Zong et al. [64]. . . . .	14
1.9	Different discharge circuits for a single PSJ actuator according to Emerick et al. [14] . . . . .	15
1.10	Different discharge circuits for a single PSJ actuator. . . . .	15
2.1	Actuator structure: Ceramic cavity (left) and brass cap (right). . . . .	22
2.2	Three types of caps used, with $\theta$ being the cap angle. . . . .	22
2.3	Electrical circuit. $R1 = 100\Omega$ , $R2 = 100\Omega$ & $C1 = 1\mu F$ . . . . .	23
3.1	Phased average velocity fields at various times after discharge of the baseline case of $\theta = 90^\circ$ . $U_{xy}$ is the Euclidean sum of the two velocity components such that $U_{xy} = \sqrt{u^2 + v^2}$ , the black box denotes the orifice location and the dark grey contours are the Q-criterion of $Q/Q_{pk} = 0.25$ . The red dashed line shows the division between the up- and downward moving air and the red dot represents the location of the stagnation point. . . . .	25
3.1	Phased average velocity fields at various times after discharge of the baseline case of $\theta = 90^\circ$ . $U_{xy}$ is the Euclidean sum of the two velocity components such that $U_{xy} = \sqrt{u^2 + v^2}$ , the black box denotes the orifice location and the dark grey contours are the Q-criterion of $Q/Q_{pk} = 0.25$ . The red dashed line shows the division between the up- and downward moving air and the red dot represents the location of the stagnation point. . . . .	26
3.1	Phased average velocity fields at various times after discharge of the baseline case of $\theta = 90^\circ$ . $U_{xy}$ is the Euclidean sum of the two velocity components such that $U_{xy} = \sqrt{u^2 + v^2}$ , the black box denotes the orifice location and the dark grey contours are the Q-criterion of $Q/Q_{pk} = 0.25$ . The red dashed line shows the division between the up- and downward moving air and the red dot represents the location of the stagnation point. . . . .	27
3.2	Phase averaged velocity fields of all orifice geometries at $t = 150 \mu s$ . The plotting methods are copied from figure 3.1. . . . .	27
3.2	Phase averaged velocity fields of all orifice geometries at $t = 150 \mu s$ . The plotting methods are copied from figure 3.1. . . . .	28
3.3	Phase averaged velocity fields at $t = 250 \mu s$ . The plotting methods are copied from figure 3.1. . . . .	28
3.3	Phase averaged velocity fields at $t = 250 \mu s$ . The plotting methods are copied from figure 3.1. . . . .	29
3.4	Streamlines showing a tertiary vortex ring for the $60^\circ$ geometry. . . . .	30
3.5	Phase averaged velocity fields at $t = 800 \mu s$ . The plotting methods are copied from figure 3.1. . . . .	30
3.6	Schematic representation of how $v_j$ is derived. . . . .	31
3.7	Jet velocity curve for all orifice geometries. . . . .	32
3.8	The total absolute vorticity (solid lines) and absolute vorticity of the front vortex ring (dash-dotted lines). . . . .	32
3.9	Exit density for various nozzle shapes. $\rho_{eUL}$ (solid lines) and $\rho_{eLL}$ (dashed lines) are the upper and lower limit of the exit density respectively. . . . .	33

5.1	Power supply system proposed by Zhang et al. [56]. Each set of 2 actuators are noted by a number and the actuators themselves are modelled as circles with two electrodes inside, also known as a neon lamp symbol. . . . .	41
5.2	Voltage and current waveforms of the PSJA array containing 26 actuators. . . . .	42
5.3	Standalone PSJA used for the first experiment. . . . .	42
5.4	X-1 setup. . . . .	43
5.5	PSJA array and cap. . . . .	43
5.6	X-2 setup. . . . .	44
5.7	Drag analysis of a lifting wing, courtesy of Maskell [33]. . . . .	45
6.1	Lift and drag polar at $U_\infty = 10m/s$ and $Re = 1.65 \cdot 10^5$ . BL is the baseline case without actuation. . . . .	48
6.2	Dynamic response of the lift force to non-dimensional discharge frequencies of $F^* = 0.25$ and $F^* = 1$ , at $\alpha = 15.5^\circ$ during a square wave test. The on or off indicate whether actuation is turned on or not. . . . .	48
6.3	Lift and drag polar at $U_\infty = 10m/s$ and $Re = 1.65 \cdot 10^5$ . BL represents the baseline case without actuation. . . . .	49
6.4	Lift and drag polar at $U_\infty = 15m/s$ and $Re = 2.48 \cdot 10^5$ . The remaining plotting methods are consistent with figure 6.3 . . . . .	50
6.5	Lift and drag polar at $U_\infty = 20m/s$ and $Re = 3.31 \cdot 10^5$ . The remaining plotting methods are consistent with figure 6.3 . . . . .	50
6.6	Lift and drag polar at $U_\infty = 30m/s$ and $Re = 4.96 \cdot 10^5$ The remaining plotting methods are consistent with figure 6.3 . . . . .	51
6.7	Jet piercing through the boundary layer. . . . .	52
6.8	Effect of duty cycle on the aerodynamic performance of NACA 0015. Solid line represents the lift curves, whilst the dotted line represents the drag curves. . . . .	53
6.9	Time averaged velocity fields without actuation and for various angles of attack. The Euclidean sum of the velocity components (denoted as $\sqrt{u^2 + v^2} = U_{xy}$ ) are shown as contours. Furthermore, the velocity profiles at various locations are shown. The solid black line represents the dividing streamline and the dashed black line denotes the location at which the condition $u = 0$ , henceforth denoted as the zero-velocity line, is reached. The location of the actuators is denoted by the green x. . . . .	54
6.10	Time averaged velocity fields with actuation at $\alpha = 15.5^\circ$ . The remaining plotting methods are consistent with figure 6.9. . . . .	55
6.11	(a) Effect of actuation frequency on lift coefficient, separation area and separation length at $\alpha = 15.5^\circ$ . (b) Varying shape factor throughout the chord for various actuation frequencies at $\alpha = 15.5^\circ$ . . . . .	55
6.12	Reynolds normal stress of the $u$ velocity component, $\frac{\sqrt{u'^2}}{U_\infty}$ , for various actuation frequencies at $\alpha = 15.5^\circ$ . . . . .	56
6.13	Reynolds normal stress of the $v$ velocity component, $\frac{\sqrt{v'^2}}{U_\infty}$ , for various actuation frequencies at $\alpha = 15.5^\circ$ . . . . .	57
6.14	(a) Chordwise variation of the peak velocity fluctuation in $y$ -direction, $\overline{v'}$ , at $\alpha = 15.5^\circ$ for varying frequencies. (b) Frequency spectra probed in the dividing streamline at $x/c = 0.7$ . . . . .	57
6.15	(a) Phased averaged separation area at $\alpha = 15.5^\circ$ . (b) Comparison between the phase averaged separation area and dynamic lift coefficient at $\alpha = 15.5^\circ$ and $F^* = 0.25$ . The markings show the instances shown in figure 6.15 . . . . .	58
6.16	Phase averaged velocity fields at $F^* = 0.25$ and $\alpha = 15.5^\circ$ . The in plane velocity is represented by black arrows and dimensionless vorticity is shown by the red contours. The borders of the separation area, $u = 0$ , are shown by the blue lines, whereas the thin grey lines represent streamlines. Vortex locations are marked by blue dots. . . . .	58
6.17	Time averaged velocity fields with actuation at $\alpha = 22^\circ$ . The remaining plotting methods are consistent with figure 6.9. . . . .	59
6.18	(a) Effect of actuation frequency on lift coefficient, separation area and separation length at $\alpha = 22^\circ$ . (b) Varying shape factor throughout the chord for various actuation frequencies at $\alpha = 22^\circ$ . . . . .	60

6.19	Reynolds normal stress of the $u$ velocity component, $\frac{\sqrt{w^2}}{U_\infty}$ , for various actuation frequencies at $\alpha = 22^\circ$ .	60
6.20	Reynolds normal stress of the $v$ velocity component, $\frac{\sqrt{v^2}}{U_\infty}$ , for various actuation frequencies at $\alpha = 22^\circ$ .	60
6.21	(a) Chordwise variation of the peak velocity fluctuation in $y$ -direction, $\bar{v}'$ , at $\alpha = 15.5^\circ$ for varying frequencies. (b) Frequency spectra probed in the dividing streamline at $x/c = 0.7$ .	61
6.22	(a) Phased averaged separation area at $\alpha = 22^\circ$ . (b) Comparison between the phase averaged separation area and dynamic lift coefficient at $\alpha = 22^\circ$ and $F^* = 0.25$ . The markings show the instances shown in figure 6.23	62
6.23	Phase averaged velocity fields at $F^* = 0.25$ and $\alpha = 22^\circ$ . The plotting methods are copied from figure 6.16	62
6.24	Phase averaged velocity fields at $F^* = 1$ and $\alpha = 22^\circ$ . The plotting methods are copied from figure 6.16	63
6.25	Phase averaged velocity fields at $F^* = 2$ and $\alpha = 22^\circ$ . The magenta triangle represents an estimated vortex based on other results, the remaining plotting methods are copied from figure 6.16	64
6.26	Instantaneous flow fields at $F^* = 1$ and $\alpha = 15.5^\circ$ during the startup phase of PSJ actuation. The plotting methods are copied from figure 6.16	64
6.27	Quenching process for $F^* = 1$ and $\alpha = 15.5^\circ$ . The red markings correspond to the time instances from figure 6.28.	65
6.28	Instantaneous flow fields at $F^* = 1$ and $\alpha = 15.5^\circ$ during the cool down phase of PSJ actuation. The plotting methods are copied from figure 6.16	65
6.29	Time averaged velocity fields with actuation directly post stall at (a) $\alpha = 15.5^\circ$ and $U_\infty = 10$ m/s and (b) $\alpha = 18^\circ$ and $U_\infty = 20$ m/s. For both cases the non-dimensional frequency is $F^* = 1$ . The remaining plotting methods are consistent with figure 6.9.	66
6.30	Time averaged velocity fields with actuation at $\alpha_{C_{L,max}}$ stall at (a) $\alpha = 22^\circ$ and $U_\infty = 10$ m/s and (b) $\alpha = 22^\circ$ and $U_\infty = 20$ m/s. The remaining plotting methods are consistent with figure 6.9.	66
6.31	Phase averaged velocity fields at $F^* = 1$ and $\alpha = 18^\circ$ . The plotting methods are copied from figure 6.16	67
6.32	Phase averaged velocity fields at $F^* = 1$ and $\alpha = 22^\circ$ . The plotting methods are copied from figure 6.16	68



# List of Tables

1.1	Basic Suction/Blowing parameters from references, $Re$ =Reynolds, $C_\mu$ = momentum coefficient, $U_{s/b}$ =blowing or suction velocity . . . . .	7
1.2	Basic DBD data from references, $Re$ =Reynolds, $C_\mu$ = momentum coefficient, $U_{ew}$ =electric wind velocity . . . . .	9
1.3	Lift and drag characteristics of a NACA 0015 airfoil at $Re = 8.96 \cdot 10^5$ with and without SJ actuation. . . . .	10
1.4	Basic Plasma Synthetic Jet parameters from references, $Re$ =Reynolds, $C_\mu$ = momentum coefficient, $U_j$ =jet velocity . . . . .	11
1.5	Basic Synthetic Jet parameters from references, $Re$ =Reynolds, $C_\mu$ = momentum coefficient, $U_j$ =jet velocity . . . . .	12
2.1	Input parameters for the PSJA. . . . .	22
3.1	Jet parameters for various orifice geometries. . . . .	31
3.2	Key performance parameters of PSJA. . . . .	34
3.3	Suggested PSJ characterisation parameter. . . . .	34
5.1	Key parameters electric circuit. . . . .	41
5.2	Key performance parameters of PSJA array (26 PSJAs). . . . .	44



# Nomenclature

## Acronyms

Symbol	Description	Dimensions	Units
AFC	Active Flow Control		
AR	Aspect Ratio		
BL	Boundary Layer/Base Line		
CBL	Cross Boundary Layer		
CDA	Continuous Descent Approach		
CDA+	Enhanced Continuous Descent Approach		
CJA	Continuous Jet Actuator		
DBD	Dielectric Barrier Discharge		
DC	Duty Cycle		
FSC	Flow Separation Control		
KH	Kelvin-Helmholtz		
LFOV	Large Field Of View		
PFC	Passive Flow Control		
PIV	Particle Image Velocimetry		
PSJ	Plasma Synthetic Jet		
PSJA	Plasma Synthetic Jet Actuator		
RMS	Root Mean Square		
SDBD	Single Dielectric Barrier Discharge		
SFOV	Small Field Of View		
SJ	Synthetic Jet		
SJA	Synthetic Jet Actuator		
SWBLI	Shock Wave Boundary Layer Interaction		
TBL	Tangential Boundary Layer		
TRPIV	Time Resolved Particle Image Velocimetry		
VG	Vortex Generator		
VR	Velocity Ratio		
ZNMF	Zero-Net Mass Flux		

**Dimensionless numbers**

Symbol	Description	Dimensions	Units
$C_D$	Drag coefficient	–	–
$C_L$	Lift coefficient	–	–
$C_\mu$	Momentum coefficient	–	–
$F^*$	Dimensionless discharge frequency/ Strouhal number	–	–
$M$	Mach number	–	–
$Re$	Reynolds number	–	–
$T^*$	Dimensionless time unit	–	–

**Greek Symbols**

Symbol	Description	Dimensions	Units
$\alpha$	Angle of attack	–	°
$\Delta$	Difference	–	–
$\delta^*$	Displacement thickness	–	–
$\eta$	Efficiency	–	–, %
$\omega$	Vorticity	$\frac{1}{T}$	$\frac{1}{s}$
$\rho$	Density	$\frac{M}{L^3}$	$\frac{kg}{m^3}$
$\tau$	Vortex power?	$\frac{ML^2}{T^3}$	W
$\theta$	Cone angle of PSJA cap/ momentum thickness	–	°/ –
$\varepsilon$	energy disposition ratio/blockage	–	–
$\zeta$	Damping coefficient	–	–

**Roman Symbols**

Symbol	Description	Dimensions	Units
$A$	Area	$L^2$	$m^2$
$AR$	Aspect Ratio	–	–
$b$	Span	$L$	$m$
$C$	Capacitance/wind tunnel cross-section area/Specific energy	$\frac{T^4 L^2}{L^2 M} / L^2 / \frac{L^2}{T^2 \Theta}$	$F/m^2 / \frac{J}{kg \cdot K}$
$c$	Chord	$L$	$m$
$D$	Drag/Diameter	$\frac{M \cdot L}{T^2} / L$	$N/m$
$d$	Distance	$L$	$m$
$E$	Energy	$\frac{ML^2}{T^2}$	$J$
$f$	Frequency	$\frac{1}{T}$	$Hz$
$H$	Shape factor	–	–

$h$	Height	$L$	$m$
$I$	Impulse	$\frac{ML}{T}$	$N \cdot s$
$L$	Lift/length	$\frac{M \cdot L}{T^2} / L$	$N/m$
$M$	Moment	$\frac{M \cdot L^2}{T^2}$	$N \cdot m$
$m$	Mass	$M$	$kg$
$n$	Number	–	–
$P$	Power	$\frac{ML^2}{T^3}$	$W$
$p$	Performance	–	–
$Q$	Energy stored within capacitor	$\frac{L^2 M}{T^2}$	$J$
$q$	Dynamic pressure	$\frac{M}{LT^2}$	$Pa$
$R$	Ideal gas constant	$\frac{L^2 M}{NT^3}$	$\frac{J}{molK}$
$r$	Radius	$L$	$m$
$S$	Surface	$L^2$	$m^2$
$T$	Temperature/period	$\Theta/T$	$K/s$
$t$	Time/thickness	$T/L$	$s/m$
$U$	Velocity	$\frac{L}{T}$	$\frac{m}{s}$
$u$	Local $x$ –velocity component	$\frac{L}{T}$	$\frac{m}{s}$
$V$	Volume	$L^3$	$m^3$
$v$	Local $y$ –velocity component	$\frac{L}{T}$	$\frac{m}{s}$
$x$	Local horizontal in-plane coordinate	$L$	$m$
$y$	Local vertical in-plane coordinate	$L$	$m$
$z$	Local out of plane coordinate	$L$	$m$

### Superscripts

Symbol	Description	Dimensions	Units
'	Fluctuation		
*	Specific/non-dimensional		

### Subscripts

Symbol	Description	Dimensions	Units
0	Initial condition/parasitic		
$\infty$	Infinity/free stream		
$a$	Actuators		
$ac$	Actuation		
$bd$	Break down		
$c$	Cap/corrected/chord		

---

<i>ca</i>	Cavity
<i>d</i>	Discharge
<i>e</i>	Electrode/expelled/exit
<i>ew</i>	Electric wind
<i>h</i>	Heating
<i>hys</i>	Hysteresis
<i>i</i>	Induced
<i>j</i>	Jet
<i>l</i>	Limiting
<i>le</i>	Leading edge
<i>m</i>	Mechanical
<i>max</i>	Maximum
<i>o</i>	Orifice
<i>o<sub>e</sub></i>	Effective orifice
<i>p</i>	Parallel/virtual relay/plasma
<i>pk</i>	Peak
<i>r</i>	Reset
<i>s</i>	Sampling/separation
<i>sb</i>	Solid blockage
<i>te</i>	Trailing edge
<i>v</i>	Volume
<i>vf</i>	Vortex front
<i>vr</i>	Vortex ring
<i>w</i>	Wing
<i>wb</i>	Wake blockage
<i>xy</i>	Euclidian sum of velocity components

# I

Literature survey.



# 1

## Literature survey.

With the ever increasing restrictions laid upon airliners to limit their emissions and noise, more drastic flow control techniques are being investigated with the hope that some of these techniques are able to revolutionise the aerodynamic and aeroacoustic behaviour of future aircraft. Especially the landing and take-off phase of aircraft are currently under scrutiny as the continued growth of cities causes airports to be enclosed by residential areas resulting in more severe constraints of noise and pollution levels. A common idea to reduce both noise and pollution is to increase the amount of continuous descent approaches (CDAs). This approach strategy, of which a schematic representation is shown in figure 1.1, allows the aircraft to remain at cruise altitude for a longer period of time. This limits the noise and local pollution exposure of the residential areas as the aircraft does not have to fly in the vicinity of these areas as well as the fact that a direct approach allows the aircraft to throttle down. According to Heathrow airport 10,000 tonnes of  $CO_2$  and £2,000,000 will be saved when increasing the CDA by 5% in the UK alone. Current limitations to the CDA are the maximum lift coefficient achieved by aircraft as higher lift coefficients allows for lower flight velocities and steeper descent paths, however flying close to the maximum lift angle of attack comes with significant risks. Depending on the aircraft, passing the maximum lift coefficient can cause sudden stall resulting in a quick drop in lift, causing the aircraft to descent much faster than expected and might even lead to the aircraft being uncontrollable. In order to mitigate this risk aircraft do not fly at close to the maximum lift angle of attack, even though it will significantly reduce  $CO_2$  emissions during landing.

Further reductions of emissions and noise would require an enhanced continuous descent approach (*CDA+*), in which aircraft are able to fly at higher lift coefficients. One method of achieving these higher lift coefficients is with the help of flow control devices that help control or delay the separation occurring during stall and allow the aircraft to fly at angles of attack past the original stall angle. This permits aircraft to descent at even steeper flight paths as shown in figure 1.1.

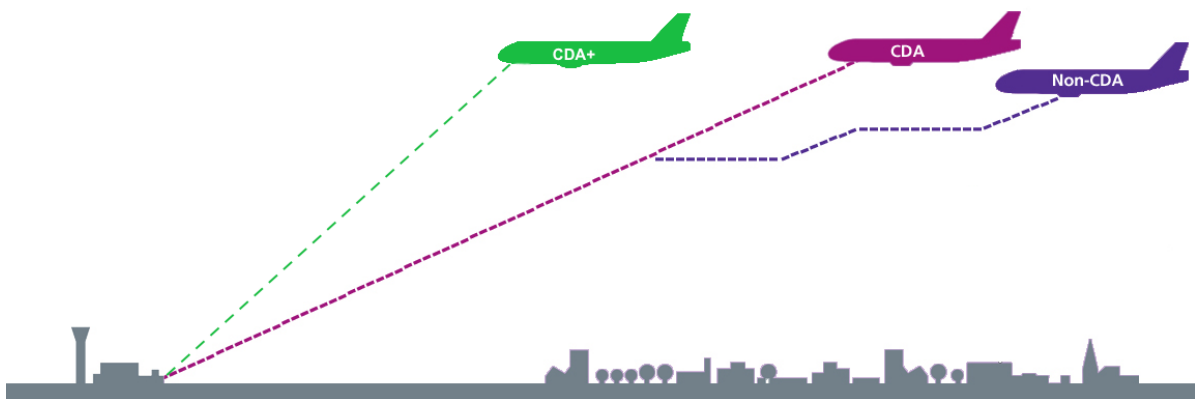


Figure 1.1: Different approach strategies.

For a significant while passive flow control devices, such as turbulators and vortex generators

amongst others have had the attention of researchers, but during the last 25 years, this attention has shifted towards active flow control devices due to their success in controlling severe adverse aerodynamic conditions, whilst having negligible penalties when turned off. Furthermore, various AFC methods have proven to be beneficial for a wide variety of applications, ranging from internal to external flows and from civilian to military aircraft. Though active flow control requires energy to operate, whilst passive flow control does not, active flow control devices offer benefits not seen in PFC devices as these devices can be turned on when flow improvements are possible, but only have a negligible drag penalty when not operated [40].

In these 25 years several techniques have emerged that have promising effects in the field of active flow control. It all started by steady blowing or suction to either introduce high momentum flow or remove low momentum flow in order to decrease flow separation. However these techniques required significant amount of pipes and pumps to work, which is where zero-net-mass-flux devices, such as the synthetic jet, came into play. These devices did not require pumps or pipes and with the introduction of piezoelectric elements their sizes could be significantly decreased, which allowed them to be implemented in small wings. Though these synthetic jet actuators offered flow control characteristics unparalleled by steady blowing or suction, the attainable frequencies and velocity ratios remained low and rendered them unsuitable for high speed applications, as, in order to work optimally, the devices should operate at frequencies similar to the instabilities of the flow itself. Fortunately an updated synthetic jet actuator came into play that used electric arcs to propel air rather than piezoelectric elements, which offered much higher jet velocities and frequencies that can match the high frequencies of instabilities. With these characteristics Plasma Synthetic Jet Actuators (PSJA) opened up a new range of applications, such as flow separation and supersonic flow control.

Though this thesis will focus upon plasma synthetic jet actuation a plethora of other techniques offer similar means of flow control, which is why 1.1 will discuss some of these more common passive (section 1.1.1) and active (section 1.1.2) flow control devices used in industrial applications.

## 1.1. Flow control devices.

When it comes to flow control a differentiation between active and passive flow control is often made. As mentioned passive flow control is able to enhance flows around objects without any energy input at the cost of a drag penalty, whereas active flow control methods are able to enhance flows without a drag penalty at the cost of an energy input. In sections 1.1.1 and 1.1.2 various passive and active flow control devices are discussed in detail.

### 1.1.1. Passive flow control.

Passive flow control devices almost always involve geometrical modifications to enhance the flow characteristics around objects omitting the need for an energy input to operate. However, due to the fact that geometrical modifications are required the PFC devices are always operating, even at flow conditions where these devices would not be necessary, possibly disturbing beneficial flow conditions. The geometrical modifications and the disturbance of beneficial flows translate to a drag penalty at some operating conditions. At other conditions the flow improvements outweigh the added drag of the modifications.

According to Joshi and Gujarathi [26] there are three main types of passive flow control devices as shown in figure 1.7. Retrofits are most similar to active flow control devices as they involve minor geometrical modifications whilst being able to beneficially affect large scale flow structures. Control surfaces are devices that involve micro structures that are unable to affect the macro scales of the flow, however the flow close to the wall is affected resulting in viscous drag reductions of 8% and a slightly improved lift when applied to airfoils and aircraft as reported by Bechert and Hage [2]. Similarly to retrofits, modifications are also able to enhance the macro structures of the flow, however this often implies drastic changes in design, which is not suitable for most aircraft applications.

As the scope of this thesis will be flow separation control, which involves affecting the macro structures of the flow, some commonly used retrofits are described in detail in the paragraphs below.

#### Gurney flaps.

Gurney flaps or lift enhancement tabs are small plates often located on the pressure side and trailing edge of lift generating devices as seen from figure 1.3. These plates, which are mostly between 1%-2% of the chord length, are placed perpendicular to the direction of the fluid flow. This results in two

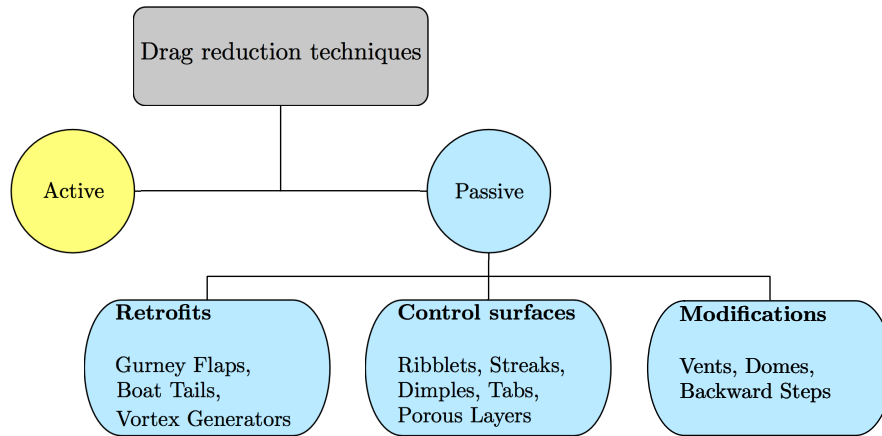


Figure 1.2: Classification of passive flow control techniques according to Joshi and Gujarathi [26].

counter rotating vortices which are alternatively shed in a von Karman vortex sheet, effectively altering the Kutta condition. This causes the pressure on the pressure side to increase and the pressure on the suction side to decrease increasing the lift, drag and pitching moment of airfoil. In the case of thick airfoils also drag reductions have been reported. At large angles of attack a chordwise vortex in front of the tab (figure 1.3) becomes more apparent. This vortex increases the effective camber of the airfoil contributing to a significant part of the lift enhancement. Joshi and Gujarathi [26] reported that perforated Gurney flaps are able to reduce drag, wake width and unsteadiness better than their solid counterpart.

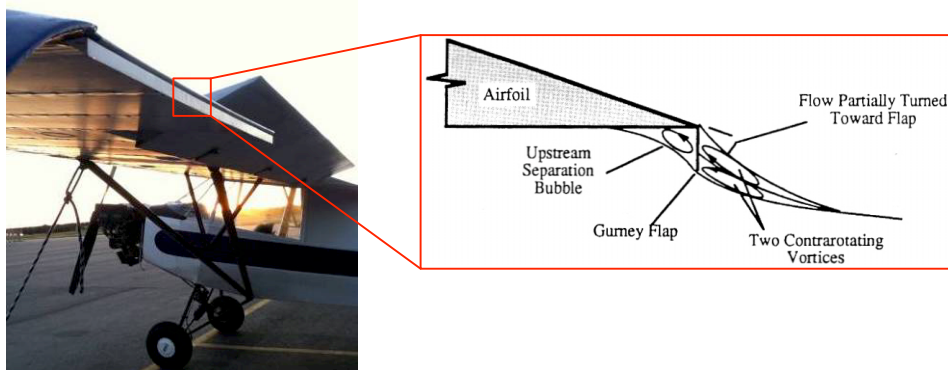


Figure 1.3: Example of a Gurney flap.

### Vortex generators.

In the case of aeronautical applications the most used passive flow control device is the vortex generator. Vortex generators consist of vanes usually attached to the suction surface that are positioned with an angle with respect to the local free stream flow. As flow passes these VGs experience high and low pressure fields at the upstream and downstream surface of the VG respectively. Similarly to wing tip vortices rotation is created as air moves from the high to low pressure field, whilst simultaneously being convected by the free stream flow. Due to these vortices the low momentum flow close to the airfoil wall is mixed with the high momentum flow of the free stream. This mixing reenergises the boundary layer and will therefore stay attached to the airfoil at higher adverse pressure gradients resulting in a flow separation delay. Figure 1.4 shows the basic working principle of VGs.

Vortex generators are able to significantly enhance flows at adverse conditions, but their benefits are severely dependent on their sizing and placement. When designed too large the VGs stick out of the boundary layer resulting in an increase of drag and when placed too far from each other not enough mixing takes place to combat adverse conditions. According to a paper by Lin [31], in which the effect of counter rotating micro VGs on an airfoil flap was investigated, the separation alleviation on the flap

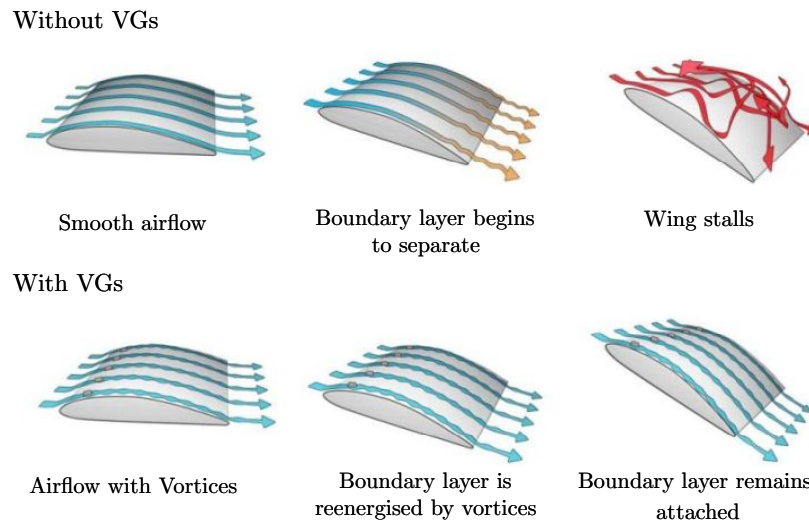


Figure 1.4: Basic principle of vortex generators according to Joshi and Gujarathi [26].

could significantly increase the lift by approximately 10%, reduce the drag by about 50%, and increase the  $L/D$  around 100% at approach angle of attack.

### 1.1.2. Active flow control.

Contrary to passive flow control its active counterpart does, in most cases, not involve geometrical modifications to aerodynamic bodies. Rather than passively influencing flows with the help of VGs and lift tabs, concentrated energised air is used to affect the macro structures of the flow. Active flow control is often seen as PFC's more sophisticated brother as it lacks almost any aerodynamic penalties when turned off, but can achieve significant flow enhancements when turned on. According to Cattafesta and Sheplak [7] AFC can be categorised into fluidic actuation, moving objects and plasma actuation as seen in figure 1.5. Though categorised into two fields some of the fluidic and plasma actuators operate in a similar fashion as both add or subtract momentum from fluids by working on a fluid, such as (plasma) synthetic jets or DBD actuation. Other techniques, such as ns-DBD and localised arc filament plasma actuators work on the premise of generating strong compression waves to achieve a controlled flow. Moving objects on the other hand are moving geometrical modifications like flaps and slats, though more sophisticated methods, such as morphing surfaces, remain an important development field.

According to Cattafesta and Sheplak [7] the most important fields of active flow control can be categorised as seen in figure 1.5. Note that for this thesis the synthetic jet and plasma synthetic jet actuators are categorised as one since their influence on the external flow is similar and the body of work on plasma synthetic jet actuators is too small to differentiate the two technologies when it comes to flow separation control.

In the following sections the most important fluidic and plasma actuators will be discussed.

#### Steady blowing and suction.

One of the older techniques revolving fluidic actuation are steady blowing and suction. These techniques either add momentum to the boundary layer or remove it. Contrary to (plasma) synthetic jets or DBD actuation these devices are not zero-net mass flux and therefore require a complex system of pumps and valves, resulting in heavy and large configurations. When it comes to steady blowing, the main working mechanism is to allow a better mixing between the high and low momentum areas of the boundary layer, resulting in better flow conditions at small adverse pressure gradients.

When suction is applied to flows it sucks low momentum air away from the surface. Research done by Kay [28], showed that uniform suction at velocities of  $U_s > 0.001U_\infty$  was able to maintain laminar flow under the prevailing conditions of free stream turbulence and surface finish. Free flight conditions might allow for lower suction velocities. Though the research done by Kay [28] shows how steady suction is able to control the transition from laminar to turbulent flow it was unable to delay separation. Still, when it comes to controlling turbulent flows with boundary layer suction it has been

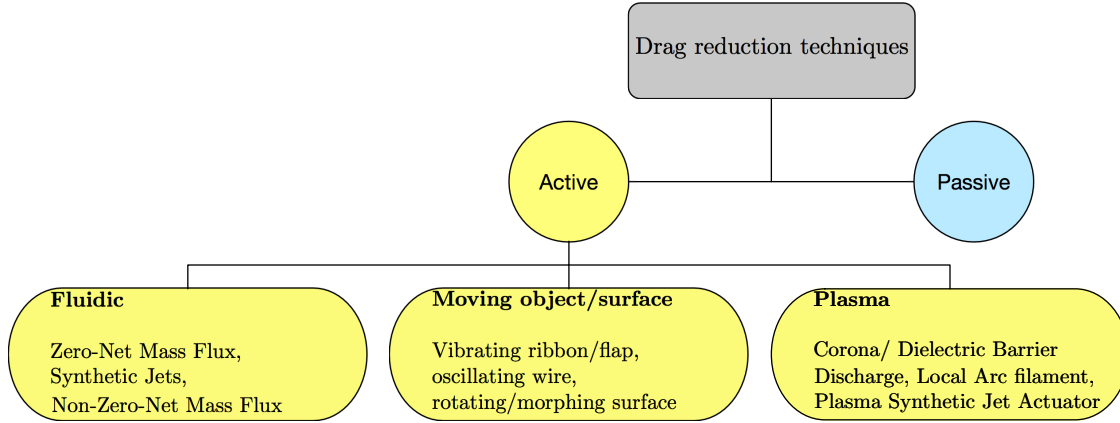


Figure 1.5: Classification of active flow control techniques according to Cattafesta and Sheplak [7].

proven that suction allows for thinner boundary layers, resulting in better virtual airfoil shapes and aerodynamic characteristics. Table 1.1 shows a summary of relevant parameters of some suction or blowing experiments.

Though both steady suction and blowing are able to enhance flow characteristics their main drawback is their inability to tap into the unsteady nature of flows, rendering them less effective than newer techniques such as (P)SJ actuation and DBD actuation. With the added disadvantage of requiring a significant amount of pumps and pipes most research has moved to newer means of active flow control.

$Re$	$C_\mu$	$U_{s/b}$	Ref
$1 \cdot 10^7$	–	$0.001U_\infty$	[28]
$16 \cdot 10^6$	0.02 – 0.04	–	[44]

Table 1.1: Basic Suction/Blowing parameters from references,  $Re$ =Reynolds,  $C_\mu$ = momentum coefficient,  $U_{s/b}$ =blowing or suction velocity

### Dielectric barrier discharge actuators.

Contrary to any other active flow control technique discussed in this chapter, dielectric barrier discharge actuators do not involve the expulsion of jets. DBD actuators operate by creating a low-temperature plasma between a pair of asymmetric electrodes by application of a high-voltage AC signal across the electrodes. As the strong electric field causes the local air to ionise it becomes susceptible to the electric fields between the electrodes causing an acceleration of the ionised particles [22, 23]. The localised velocity increase is referred to as an electric wind, rather than a jet.

The current interest of these devices is due to the fact that they are light and can be implemented such that additional drag is negligible whilst having rapid response times. Though several kinds of DBD actuators are being researched most of the work is focused on the single dielectric barrier discharge actuator (SDBDA). As the effect of these SDBD plasma actuators have been mainly proven for low Reynolds numbers, some researchers still question the applicability of these actuators since most aeronautical applications require operation at Reynolds numbers of  $Re > \mathcal{O}(10^6)$ . Their main limitation to high-speed and high-Reynolds number applications is the low velocity produced by the actuators, which is in the order of several meters per second [22]. Though most work on SDBD actuation is performed on low Reynolds numbers several papers, including ones by Moreau et al [35], Xin et al [52] and Little et al. [32], have moved to moderate Reynolds number of  $\mathcal{O}(10^6)$ .

The research performed by Little et al. [32] involved nanosecond DBD actuation, around a NASA Energy Efficient Transport airfoil operating at  $Re = 0.75 \cdot 10^6$ . As the aim of the research was flow separation control at high angles of attack the DBD actuator was placed close to the leading edge,  $x/c \approx 0$ , as to allow actuation to take place before the separation point. From the force balance measurements it was found that having ns-DBD actuation could increase the maximum lift by approximately  $\Delta C_l \approx 0.35$  or 27%, whilst delaying the stall angle by  $6^\circ$ . The working mechanism at pre-stall conditions was by tripping the flow showing that ns-DBD actuation can act as an active trip. At post stall conditions

ns-DBD actuation was able to manipulate flow instabilities to generate coherent spanwise vortices within non-dimensional frequency ranges of  $0.6 \leq F^* \leq 11.3$ . The vortices caused entrainment of the free stream flow and were transported to the near wall regions allowing the flow to be reenergised. This control mechanism, which is widely recognised for controlling separation in a variety of flow systems, was observed to be most effective at frequencies of  $4 \leq F^* \leq 5$ , higher than the normally encountered in such flow control studies where optimal frequencies are similar to 1 ( $F^* \sim 1$ ). Increasing the Reynolds number to  $Re = 1 \cdot 10^6$  showed no Reynolds number effect in the performance of ns-DBD actuation, however it does follow the  $F^*$  scaling.

Rather than using a single DBD actuator at the leading edge of the airfoil Moreau et al. [35] placed three DBD actuators ( $x = 0.18c$ ,  $0.27c$  and  $0.36c$ ) on a NACA 0015 airfoil operating at an angle of attack of  $\alpha = 11.5^\circ$ , experiencing trailing edge separation, emanating from  $x/c = 0.5$ , is present. With the wind tunnel operating at a free stream velocity of  $U_\infty = 40 \frac{m}{s}$  a Reynolds number of  $1.33 \cdot 10^6$  has been obtained. When operating in single actuator mode it was observed that actuator locations closer towards the leading edge are able to combat separation better as actuation at  $0.18c$  was able to delay the mean separation point by  $0.14c$ , whereas the other actuation locations are only able to delay it by  $0.06c$ . This could be explained by the oscillatory behaviour of the separation point as the instantaneous location of the flow detachment fluctuates between  $x = 0.25c$  and  $x = 0.91c$ . The DBD actuator at  $0.18c$  remains well ahead of the separation point, whilst the DBD actuators located at  $0.27c$  and  $0.36c$  are sometimes exposed to the separation region. This corresponds to the findings by Jolibois et al. [25] and Bouremel et al. [4] in which the effect of varying actuator location on airfoils operating at  $Re = 0.4 \cdot 10^6$  and  $Re = 0.35 \cdot 10^6$  is researched. Though separation is delayed best by actuators located as close to the leading edge as possible, there are angles of attack at which other actuation locations offer better lift and drag enhancements, but as soon as the separation point lies upstream of the DBD location most benefits are diminished.

Apart from using a single actuator at varying chordwise location, Moreau et al. [35] also investigated their effect when being turned on simultaneously. Turning on all three actuators at once resulted in a continuous actuation area between 18% and 38% increasing the electric wind velocity from  $4.3 \text{ m/s}$  to  $7.3 \text{ m/s}$ . It was also found that this configuration was able to push the separation point to  $x = 0.76c$ , an improvement of  $0.12c$  when compared with a single DBD actuator at  $x = 0.18c$ . However, with the significant performance enhancement three DBD actuators over a single DBD actuator comes the cost of a power consumption that is tripled with respect to a single DBD actuator.

Apart from testing the optimal actuator location also the effect of actuation frequency has been studied using two methods. During the first experiment the actuation frequency has been varied between  $0.31 \leq F_{ac}^* = \frac{L_s f_{ac}}{U_\infty} \leq 6.13$ , where  $L_s$  is the separation length. It was found that in this case the larger effects have been found at  $F_{ac} = 0.31$  and  $3.1$ , of which the latter performed better. The other method involved keeping the actuation frequency constant, but having a sine signal that was burst-modulated at a lower frequency with a duty cycle of 50%. It was found that  $F_{burst}^* = 0.31$  was the best performing frequency. The reason for the  $F^* = 0.31$  to operate this well is that this value corresponds to the vortex shedding frequency determined from the shear layer vorticity thickness.

Rather than testing traditional DBD actuators, Xin et al. [52] tested symmetric DBD actuators on a high Reynolds number,  $2.0 \cdot 10^6$ , airfoil. This symmetric DBD actuator covered nearly the entire span of the wing and was placed at 1% of the chord, such that it would be in front of the separation point at all times. This symmetric DBD actuator has two induced airflow directions on each edge of the exposed electrode, creating an upstream and downstream moving electric wind. Apart from creating electric winds also large scale spanwise vortices were detected, promoting the mixing of the high and low momentum regions within the flow. Due to this mixing stall could be delayed by  $2^\circ$  and maximum lift could be enhanced by 8.98%. When operating at post stall conditions differences in lift between the actuated case and the baseline were reported to be 42%. Therefore, symmetrical DBD plasma actuators show potential for replacing leading edge slats and controlling separation flow at high angles of attack.

Apart from using DBD actuation to delay separation also their use as virtual Gurney flaps are reported by Feng et al. [16]. In this case a DBD plasma actuator is placed at the trailing edge of the pressure side of a NACA 0012 airfoil operating at  $Re = 2 \cdot 10^4$ . Similarly to Xin et al. [52] the DBD actuator created a wall jet moving against the free stream flow in order to form a quasi-steady recirculation region resulting in a reduction of the pressure side velocity. This circulation region also draws the air over the suction surface toward the leading edge aiding flow reattachment. These flow

modifications create an increased pressure difference between the pressure and suction surface of the airfoil enhancing its lift characteristics. It has been reported that the working mechanism behind the virtual Gurney flap is very similar to a mechanical Gurney flap, in which a momentum coefficient of  $C_\mu = 0.001$  corresponds to a mechanical Gurney flap of  $0.001c$  in terms their equal lift enhancement.

In table 1.2 the typical Reynolds number, momentum coefficient and electric wind velocity for several DBD actuation experiments on airfoils are shown.

$Re$	$C_\mu$	$U_{ew}$	Ref
$2.3 \cdot 10^4$	0.009 – 0.011	–	[24]
$4.6 \cdot 10^4$	0.006	–	
$3.3 \cdot 10^4$	–	$0.6U_\infty$	[50]
$1.33 \cdot 10^6$	–	$0.18U_\infty$	[35]
$2 \cdot 10^6$	0.002 – 0.045	$0.08 – 0.39U_\infty$	[52]

Table 1.2: Basic DBD data from references,  $Re$ =Reynolds,  $C_\mu$ = momentum coefficient,  $U_{ew}$ =electric wind velocity

### Plasma & synthetic jet actuators.

Though DBD actuation is able to enhance flow conditions at low-moderate flow speeds their main disadvantage is their low electric wind velocities rendering them less useful for high velocity applications. When applications are exposed to high-subsonic, transonic or even supersonic flow conditions devices with higher velocity potentials are required, such as synthetic and plasma synthetic jet actuators. Where the electric wind velocities of DBD rarely exceed the  $10 \text{ m/s}$ , jet peak velocities reached by synthetic and plasma synthetic jets are reported to exceed  $100 \text{ m/s}$  and  $300 \text{ m/s}$  respectively.

Both actuators operate on the premise that the cavity pressure is increased by energy addition resulting in an expulsion of gas after which a weak vacuum is created that allows air to be sucked back into the actuator. In the case of PSJ actuation this is achieved by an arc quickly heating the cavity air, whilst for synthetic jets piezoelectric elements rapidly shrink the cavity size. As the amount of energy that can be added by heating of the cavity air is significantly higher than by rapidly decreasing the volume with the help of piezoelectric elements the jets created by PSJ actuation achieve much higher exit velocities. However, due to the novelty of PSJAs not many flow control experiments have been performed using this technology, which is why the majority of this section is based on the flow control experiments using SJ actuation instead.

One of the first to apply SJAs to a NACA 0015 airfoil were Gilarranz, Traub and Rediniotis [18, 19], who placed an SJA array at  $x = 0.12c$  to test how such an array affects the performance of the airfoil between angles of attack varying from  $-2^\circ$  to  $29^\circ$ . Similarly to the research performed by Chatlynne et al. [8] actuation at small angles of attack ( $< 10^\circ$ ) only shows marginal improvements when SJ actuation is applied. However, actuation frequency, or enlarging the momentum coefficient, does weakly affect the lift curve slope. Furthermore, at this range of  $\alpha$  static pressure measurements concluded that only the first 25% of the chord was affected by actuation. This changed when the angle of attack was increased, where SJ actuation was able to delay stall from  $12^\circ$  to  $18^\circ$  and enhancing the maximum achieved lift by 40% and at  $\alpha = 18^\circ$  by 80% with respect to the baseline case. Even at angles beyond  $\alpha = 18^\circ$ , at which massive stall occurs for all cases, the lift characteristics remained improved when compared to the unforced case. However, increasing the angle of attack past  $\alpha > 25^\circ$  showed that actuation was only able to locally affect the first 25% of the chord and in order to see any beneficial effects the frequency needed to be adjusted.

As the research done by Gilarranz et al. [19] comprised of force balance and pressure measurements only several papers used computational fluid dynamics to find the underlying mechanisms that allow SJ actuation to enhance the flow around an airfoil. Both You and Moin [53] and De Giorgi et al. [10] researched a numerical representation of the experiment by Gilarranz et al. [19] and confirmed the effect that SJ actuation is able to affect the stall characteristics of airfoils and thereby enhancing both lift and drag. In table 1.3 the results of each paper is shown

You and Moin [53] found that by using an unstructured-grid LES solver detailed flow structures within the synthetic-jet actuator and the synthetic-jet/cross-flow interaction could be predicted that gave more insight into the findings by Gilarranz et al. They found that adding or removing momentum to or from the boundary layer was able to stabilise the boundary layer and promoted the mixing between

experiment	uncontrolled		controlled	
	$C_{L_{max}}$	$C_D$	$C_{L_{max}}$	$C_D$
Gilarranz et al. [19]	0.82	0.26	1.41	0.22
You and Moin [53]	0.81	0.28	1.40	0.22
De Giorgi et al. [10]	0.84	0.27	1.45	0.23

Table 1.3: Lift and drag characteristics of a NACA 0015 airfoil at  $Re = 8.96 \cdot 10^5$  with and without SJ actuation.

the inner and outer part of the BL as well. During the suction phase low momentum air is removed preventing separation to occur downstream of the array, whilst during blowing the jets caused mixing between the high and low momentum regions of the BL to occur preventing flow separation as well. This behaviour was confirmed by De Giorgi et al. [10], where this behaviour is compared with an array of continuous jet actuators. It was found that the main drawback of using CJA is that it cannot be used to decrease the unsteady behaviour of the flow. Due to the fact that unsteady phenomena play a significant role in flow separation CJ actuation will be less effective in enhancing aerodynamic properties of objects suspended in separated flow. In fact, it was found that with similar momentum coefficients, synthetic jet actuation is preferred over continuous jet actuation as SJAs not only exploit the unsteady flow behaviour but mostly because the relative reduction of the total pressure losses for the SJA is approximately twice as large as that for the CJA. This simply means that SJAs require less energy to operate than their continuous counterpart.

The working mechanism that allow SJ actuation to be more efficient than CJ actuation is the increased production of discrete vortices. When convected downstream these vortices merge and create a wake virtually shaping the airfoil. These vortices are created by the collision of the free stream flow with the jet. During the blowing phase the vorticity of the leeward side of the jet is increased mainly due to the curving of the jet flow by the free stream flow, whereas the vorticity on the windward side remains weaker. As the blowing phase advances the leeward side vortical structures are stretched and increase in size and are slowly convected downstream.

Similarly to the numerical research by De Giorgi et al. an experimental research by Seifert and Pack [43] also compared the effectiveness of oscillatory blowing/suction with CJ actuation on a NACA 0015 airfoil, albeit at large Reynolds numbers that correspond to a jetliner at take-off conditions. Similarly to the paper by De Giorgi et al. [10] it was found that oscillatory blowing/suction is able to tap into the unsteadiness of the flow thereby requiring a lower momentum coefficient to achieve similar lift and drag enhancements than required for continuous jets. It reported that the best frequencies to operate for oscillatory blowing/suction lies within the region of  $0.5 \leq F^* \leq 1.5$ , where an optimum is reached around  $F^* \approx 1$  regardless of the Reynolds number. Seifert and Pack [43] suggested that by applying a pressure tab at the trailing edge a closed loop system, in which the momentum coefficient is adjusted to its optimum, could improve the system even more and allow them to be used to enhance geometries encountering steeper adverse pressure gradients.

The only PSJA experiment on a NACA 0015 was performed by Caruana et al. [6] in which a NACA 0015 at a Reynolds number of  $1.2 \cdot 10^6$  was placed in a free stream velocity of  $U_\infty = 40 \frac{m}{s}$ , see table 1.4 for a summary of the parameters. Contrary to the other experiments the actuator is placed further downstream at  $x = 0.32c$  rather than  $x = 0.12c$  in the cases of Gilarranz et al. [19], You and Moin [53] and De Giorgi et al. [10]. Similarly to the SJ actuation experiments PSJ actuation is able to push the separation point towards the leading edge allowing for better flow conditions over the airfoil. Pressure measurements have shown that using PSJ actuation allowed for a recompression of the former separated area. Furthermore, it was found that by applying PSJ actuation result in fuller velocity profiles. Increasing the actuation frequency enhance the fullness of the profile but this benefit caps off at higher frequencies. Due to the fact that PSJ actuation was able to delay the separation point resulting in smaller wake regions a drag reduction of 19% was found. Unfortunately this decrease in drag was only reported for angles  $\alpha \leq 11.5^\circ$ , contrary to the SJ actuation findings, however this is due to the fact that at  $\alpha > 12^\circ$  the separation point moves upstream of the PSJ array rendering them unable to affect the flow.

Apart from studies performed on a NACA 0015 airfoil, similar studies on the effect of SJ actuation on other airfoils have also been performed. One of those studies, performed by Kim and Kim [29],

$Re$	$C_\mu$	$U_j$	$F^*$	Ref
$1.2 \cdot 10^6$	–	$2.25U_\infty$	0.85-6.35	[6]

Table 1.4: Basic Plasma Synthetic Jet parameters from references,  $Re$ =Reynolds,  $C_\mu$ = momentum coefficient,  $U_j$ =jet velocity

was a numerical simulation of a NACA 23012 airfoil operating at  $Re = 1.2 \cdot 10^6$ . Kim and Kim found that leading edge separation control, apart from its frequency, is also dependent on the peak velocity of the jet. When the jet velocity is in the same order of the free stream velocity SJ actuation is unable to enhance the flow characteristics of the airfoil, whilst at peak velocities that are two or three times higher than the free stream lift is enhanced. The reason for this behaviour is that at low velocities the disturbances created by the jets are unable to reach the separation point as the momentum of the fluid expelled is too low. The low momentum jets are only able to locally affect the flow, which at  $\alpha = 18^\circ$ , resulted in a decrease in lift and increase in drag. With an increase in angle of attack the separation point moves closer to the SJ array, which does allow all cases, also the case in which the peak exit velocity matches the free stream velocity, to positively affect the flow. The optimum actuation frequency is also found to be  $F^* = 1$  as is reported in many other papers. The reason why low frequency modulation obtained better results is due fact that the small vortices shedded by the actuator move along the suction surface and are able to penetrate the large leading edge separation vortex. This results in a substantial decrease of the leading edge separation vortex. However, when actuation frequency is increased the small vortices shed by the SJAs are not able to grow due to their close proximity as the actuators shed them to fast. This causes the flow the synthetic jet slot to be firmly attached, resulting in a more stable flow structure on the suction surface. Furthermore, the highest lift and drag

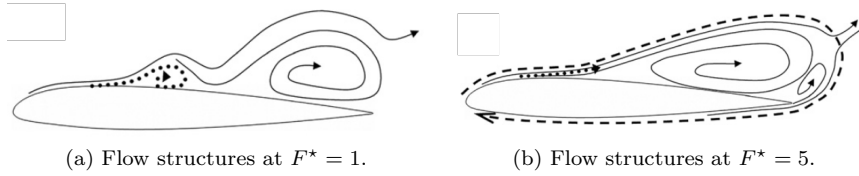


Figure 1.6: Varying large scale structures at various actuation frequencies and  $U_j > U_\infty$  [29]. The dotted line is the modulated flow by the jet.

enhancements occur when the actuator location matches the separation point, which is in accordance with a paper by Greenblatt and Wignanski [20] in which the criteria for optimum actuation were found to be:

- $F^* \approx 1$
- $U_j > U_\infty$
- $\left(\frac{x}{c}\right)_{SJA} = \left(\frac{x}{c}\right)_s$

Apart from a single SJA location, the effects of having two SJA arrays, located at  $x = 0.12c$  and  $x = 0.3c$  respectively, was also investigated. By adding an appropriate phase delay between the two arrays steady flow conditions were found, which were not achieved using a single array. Furthermore, the dependence of actuation frequency remains the main driver of aerodynamic benefits.

In the above mentioned experiments all jets were configured ‘shooting’ into the boundary layer, also known as the Cross Boundary Layer (CBL) configuration. However, a numerical study by Esmaili Monir et al. [15] investigated the effect of Tangential Boundary Layer (TBL) jets. The main difference between these configurations is that a CBL configuration creates a jet moving away from the surface, typically inclined by an angle of  $\alpha_j = 23^\circ$  between the synthetic jet axis and the local surface of the airfoil as advised by Kim and Kim [29], whereas using a TBL configuration creates jets moving along the surface of the airfoil. It was found that the implementation of a TBL jet array gained a significant improvement over the traditional CBL jet arrays when comparing their improved lift and drag characteristics. According to Esmaili Monir et al.[15] ‘A lot of the infused momentum in the CBL synthetic

jet is spent on crossing the boundary layer and creating “slowly moving” vortex structures with larger dimensions in the normal direction to the wall.’. Thus implementing TBL jet arrays would be more effective in flow separation as the smaller vortices infuse the jet momentum only in the boundary layer where it counts and not the outside regions of the flow. However, the manufacturing process of the caps will be more difficult than just drilling a hole as done for CBL synthetic jet configurations.

Table 1.5 shows a summary of the most important parameters of various SJ actuation experiments. Comparing this data to the DBD parameters, table 1.2 one can see the improved jet velocities with respect to the low electric wind velocities, however the momentum coefficients are reduced with respect to DBD actuation. This shows that in order to achieve similar amount of flow control, less momentum addition is required suggesting that, if efficiencies of both devices are similar, SJ actuation requires less energy to operate.

$Re$	$C_\mu$	$U_j$	$F^*$	Ref
1150	–	$0.2 - 0.5U_\infty$	0.1-0.7	[54]
$2.3 \cdot 10^4$	0.009 – 0.011	–		[24]
$4.6 \cdot 10^4$	0.006	–		
$1.2 \cdot 10^5$	$1.2 - 4.2 \cdot 10^{-5}$	$0.12 - 0.22U_\infty^*$	3.6-10.8	[47]
$2.5 \cdot 10^5$	0.0019	–	$\mathcal{O}(1)$	[8]
$2.73 \cdot 10^5$	0.0014	$1.32U_\infty$	2.5-5.5	[30]
$3.81 \cdot 10^5$	0.0012	–	0.65-1.4	[1]
$8.96 \cdot 10^5$	0.0123	$2.14U_\infty$	0.65-1.4	[53]
$8.96 \cdot 10^5$	0.0051 – 0.0254	$1.03 - 2.31U_\infty$	0.57-1.23	[19]
$6.7 \cdot 10^5 - 1.0 \cdot 10^6$	0.003 – 0.016	–	–	[11]
$2.19 \cdot 10^6$	0.0002 – 0.0008	$1 - 3U_\infty$	0.5 – 5	[29]
$16 \cdot 10^6$	0.0002 – 0.0006	–	0.5-1.1	[43]

Table 1.5: Basic Synthetic Jet parameters from references,  $Re$ =Reynolds,  $C_\mu$ = momentum coefficient,  $U_j$ =jet velocity

Apart from studies (P)SJ actuation studies performed on airfoils also their effect on ramps have been tested as this allowed for a more detailed view on the mechanism behind flow separation control. One experiment performed by Zhang et al. [54] was to see how the reduced frequency,  $F^* = \frac{fh}{U_\infty}$ , as well as the velocity ratio,  $VR = \frac{\bar{U}_j}{U_\infty}$ , influence the separation region. Both low and high actuation frequencies were able to combat flow separation, however increasing the velocity ratio seemed of little effect on the decrease of the separation region at low reduced frequencies,  $F^* = 0.2$ . At higher frequencies,  $F^* = 0.6$ , an increase in velocity ratio did show a steady decrease to the separation region. Furthermore the results suggest that higher frequencies result in larger affected regions. This would mean that fewer actuators would be required to achieve similar effects, especially when high velocity ratios are used. Lastly, using higher frequencies does not only result in larger affected regions, the effects also last the entire cycle of the actuator. This is not the case at low frequencies where the height of the separation bubble oscillates throughout the jet cycle.

One of the more important improvements of PSJAs over SJAs is their enhanced jet velocities. Where SJAs reach peak jet velocities around 100  $m/s$  PSJAs can reach velocities over 300  $m/s$  allowing them to affect supersonic flows. Though no supersonic airfoil models have been tested some research on the topic of the effect of PSJ actuation on Shock Wave Boundary Layer Interaction (SWBLI) has been performed. A study by Narayanaswamy et al. [37] showed the effect of PSJ actuation on a  $24^\circ$  compression ramp at a Mach number of  $M = 3$ . Similarly to the subsonic separation flow control studies it was found that when the actuation location is upstream of the separated show PSJ actuation was able to significantly modify the separated flow dynamics. However, when placed downstream of the separated shock PSJ actuation no noticeable change in the dynamics took place. By comparing the flow fields it was found that the difference in shear layer perturbation might be the cause of the difference in effectiveness of PSJ actuation. This is due to the fact that when applying upstream actuation the perturbations within the shear layer grow when convected downstream, which is not seen for downstream actuation. Similar growth of the shear layer perturbations are also reported in various subsonic separation control

experiments, which illustrates the importance of the shear layer above the separation bubble in determining the SWBLI and ordinary separation control dynamics. This was confirmed by Greene et al. [21] at which a similar experiment using a PSJ actuation to affect the SWBLI of a  $20^\circ$  compression ramp at  $M = 3$ . The placement of the PSJA arrays proved very sensitive as any effect of PSJ actuation died out when placed more than  $3\delta$  upstream of the compression ramp corner. Suggesting the boundary layer mixing induced by the jets dies out relatively quickly. The optimal placement was found to be  $1.5\delta$  upstream of the compression ramp corner. Apart from placement also the Strouhal number appeared to affect the actuator performance. Furthermore, PIV measurements showed that PSJ actuation are able to decrease the skin friction and overall thickness of the boundary layer downstream of the shock interaction at the unfortunate cost of making the boundary layer more susceptible to separation. This indicates that if the main goal is to minimise flow distortion downstream of the SWBLI a reduction of the separated region might be counterproductive.

## 1.2. Plasma Synthetic Jet Actuators

As mentioned in section 1.1.2 Plasma Synthetic Jet Actuators belong to the zero-net mass flux fluidic actuators as no mass is extracted or added to the free stream. It

### 1.2.1. Basic discharge

Similarly to Synthetic Jet actuation the cycle of PSJ actuation can be separated into three different phases. These phases, being the energy disposition, expulsion and suction phase are individually described below.

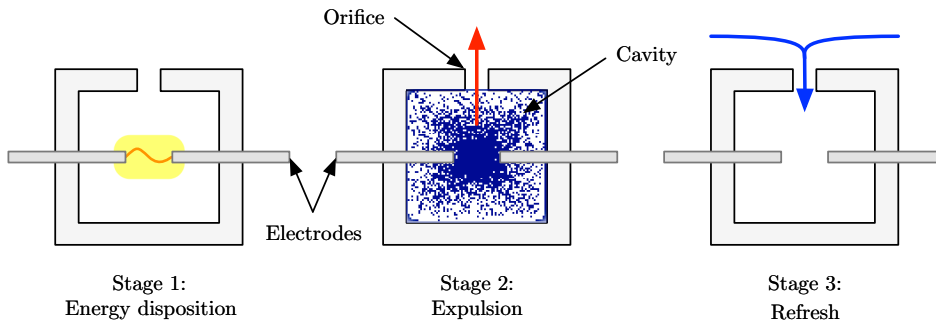


Figure 1.7: Three different phases in a PSJA cycle.

#### Energy disposition phase.

During the energy disposition phase energy is supplied to the air within the cavity. Contrary to SJ actuation, where energy is supplied by rapidly decreasing the cavity volume with the help of piezoelectric elements, PSJ actuation receives its energy from an electrical arc between two electrodes. This arc, created by supplying a voltage source high enough such that the air gap between the electrodes can be crossed, is sustained by energy stored into a capacitor which rapidly deposits its energy within the cavity. The high temperature arc then heats up the air within the cavity causing the pressure to rise. Unfortunately, most of the energy stored in the capacitor does not end up heating the cavity air as most is lost in the processes of creating streamers, molecular ionisation, localised heating of the electrodes and molecular excitation that does not convert to translational energy (heat), which is schematically represented in figure 1.8. CFD modelling found that the energy put into heating of a specific PSJ actuator, was about 35% of the total capacitive energy supplied [40]. However, it was found that this value is greatly influenced by both the capacitance and the discharge voltage, where trends towards higher capacitances and lower voltages achieve higher efficiencies as this results in wider arcs and longer discharge times [40, 64]. According to Caruana et al. [6], the plasma acts as a small resistance of several Ohms, which explains why lower voltages result in higher efficiencies as the heat dissipated by a resistance is not dependent on the voltage, but on the current squared as  $P_h = I_d^2 R_p$ . Therefore typical heating efficiencies lie in the order of  $\eta_h \sim \mathcal{O}(10\%)$ .

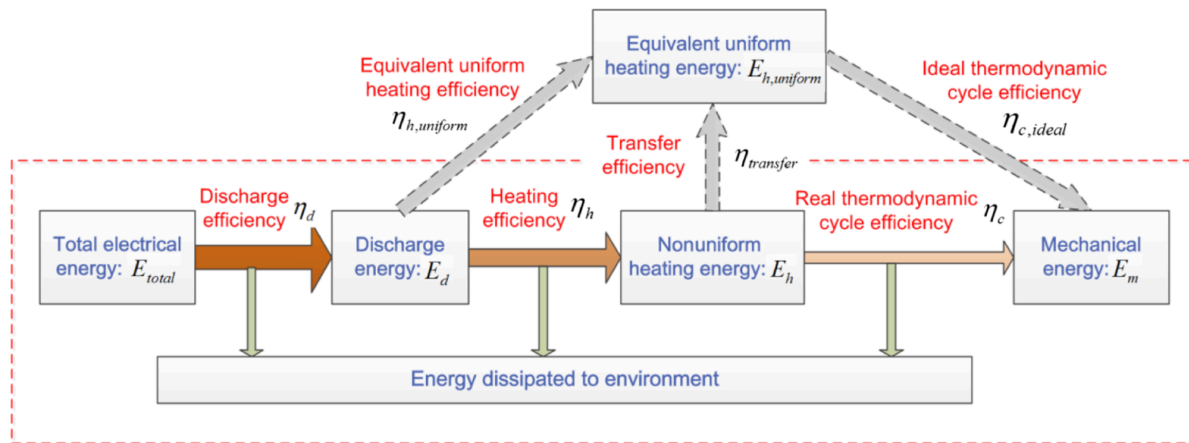


Figure 1.8: Losses experienced during PSJ actuation according to Zong et al. [64].

According to Zong et al. [64] the main reason for the low working efficiency of PSJ actuation is the low thermodynamic cycle efficiency, which is typically less than 30%. This thermodynamic efficiency is mainly dependent on two parameters being the non-dimensional energy deposition and the heating/discharge time. Increasing the former shows a linear trend with the thermodynamic cycle efficiency whilst the discharge time negatively influences the efficiency.

#### Discharge phase.

After energy has been supplied to the actuator the pressure within the cavity has increased to such an extent it forces air out of its orifice, creating a strong jet. Initially this flow is choked, resulting in an exit pressure that exceeds the atmospheric pressure, however this passes and at the end of this phase the cavity is left with low density heated air at a pressure slightly below the atmospheric conditions.

#### Refresh phase.

The third phase is represented by a reintroduction of relatively cool, high-density ambient air into the cavity due to the fact that a pressure gradient across the orifice sucks air into the cavity. This process is maintained by the convective and conductive cooling across the internal cavity surfaces allowing the air inside the cavity to drop together with the continued cooling of the ceramic walls and electrodes. This maintains a slight pressure gradient up to the point where the walls reach the ambient air temperature, at which point the cavity pressure equals the ambient air pressure [40].

### 1.2.2. PSJA geometries.

When it comes to the synthetic jet a significant amount of geometrical parameters have been tested, most of them related to the orifice geometry. However, specific design parameters are purely valid for plasma synthetic jet actuators, which is why this section will discuss the effect of orifice geometry apart from the PSJA specific geometrical parameters.

#### PSJA

When it comes to PSJA specific geometrical parameters the electrode distance and configuration are the main variables to be considered. When it comes to the latter parameter two configurations are often used. In the early development of PSJ actuators a three-electrode configuration is most often used, however this has changed to a two electrode geometry in more recent studies. The three electrode-configuration, also known as the external trigger configuration as shown in figure 1.9a, uses an extra electrode to create an arc between the anode and cathode whereas the pseudo-trigger configuration (figure 1.9b) uses the anode as the trigger electrode. The electrical circuits of both configurations are shown in figure 1.10. In the research by Zong et al. [63] the influence of electrode distance on the performance of a PSJA jet is tested, from which it was found that increasing the electrode distance resulted in a larger discharge energy deposited into the cavity. However, increasing the electrode distance past the optimum resulted in a sharp declination due to the fact that the discharge time is shortened.

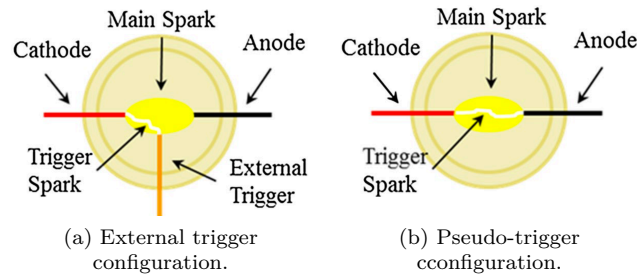
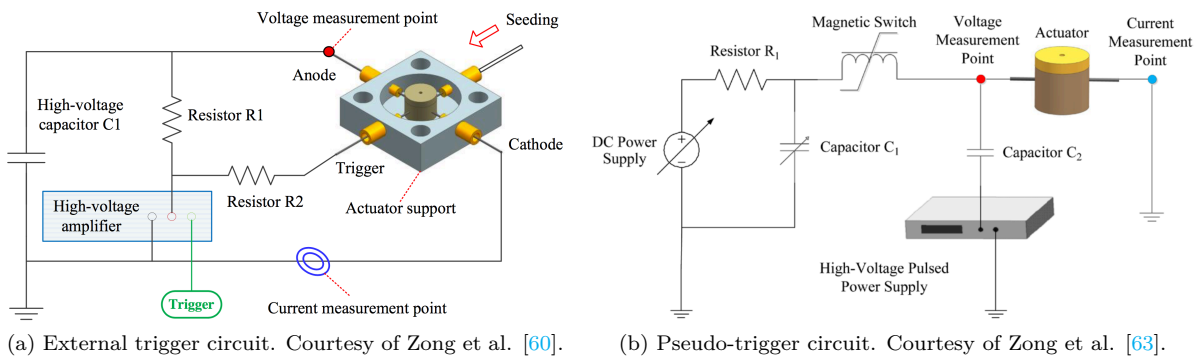


Figure 1.9: Different discharge circuits for a single PSJ actuator according to Emerick et al. [14]

Though it was found that discharge energy is an important parameter when optimising the geometry, the heating volume remains dominant, as is also found by Popkin et al. [40] and Caruana et al [6].

A significant benefit of the pseudo-trigger configuration is its ability to have higher electrode distances without reducing the discharge energy improving its ability to create larger heating volumes and effectively enhancing the heating efficiency of PSJAs. According to Popkin et al. [39] the switch from external trigger geometry to pseudo-trigger geometry has resulted in a theoretical operating efficiency increase from 30 to 75%, at the cost of a more complex electrical circuit as seen from figure 1.10.



(a) External trigger circuit. Courtesy of Zong et al. [60]. (b) Pseudo-trigger circuit. Courtesy of Zong et al. [63].

Figure 1.10: Different discharge circuits for a single PSJ actuator.

Apart from a traditional single arc discharge, research done by Zhang et al. [55–57] has shown that having multiple electrode pairs within a cavity can significantly enhance the performance of PSJAs. The newly used circuit allows for the increase of the total distance of the spark channel without using a larger input voltage. This is achieved by implementing virtual voltage relays that ramp up the voltage in-between electrode pairs. It was found that having this multi-electrode circuit is able to increase the plasma resistance as well as doubling the discharge efficiency, though the growth flattens as more electrode pairs are used. Furthermore a significant increase in the jet duration and velocity are reported.

### Orifice geometry

A significant amount of effort has been put in to understand how the orifice geometry affects the jet produced by (P)SJ actuation. Zong et al. [63] did extended research on the influence on several geometrical throat parameters, such as orifice diameter and throat length. The performance of each parameter was based the estimated pulsed thrust, the discharge characteristics, and the Schlieren images taken during discharge. During their measurements a pressure probe was moved throughout the jet concluding that the total pressure is highest in the centre or axis of the jet and decreases with increasing distance from this axis. By enlarging the orifice diameter it was found that the total pressure of the jet is inversely associated with the orifice diameter. An increase in orifice diameter also resulted in higher peak jet front velocity, but a decrease in both jet duration and jet delay time. Lastly the pulsed thrust is negatively affected as larger diameters resulted in a decrease of pulsed thrust.

The effect on the throat length is less prominent than the orifice diameter, but still plays an important role when optimising PSJ geometry. It was found that increasing the throat length increases the

jet front velocity and the jet delay time whilst decreasing the jet duration time. Especially the latter raised concern as the jet intensity dropped by 30% when the throat length was increased from 2 *mm* to 6 *mm*. The reason for this effect is that increasing the throat length causes both the inertia of the throat gas, as well as the viscous drag to increase. Since the driving forces of the jet are always related to the pressure difference across the throat an increase in throat length directly results in a reduction of the jet and suction velocity as the pressure difference remains the same whilst the viscous and inertial forces have increased. This reduction in jet and suction velocities resulted in a larger refill time, which can be problematic at high actuation frequencies as a lack of time results in a decrease in cavity density as it did not have the change to completely refill itself. This translates to a decrease in jet duration time as actuation cannot achieve the high pressures to expel the same amount of gas. This indicates that the throat length should be minimised on the premise that structural integrity is maintained [63]. A numerical research by Caruana et al. [6] showed that introducing a cone angle does enhance the refill properties of an actuator. A MSc. thesis performed by Nani [36] showed similar results when using a rounded inner lip of the orifice. Though the size of this orifice is significantly larger, 12.7 *mm* rather than the 1 *mm* used by Caruana et al. [6], it is expected that the trends seen in this thesis translate to some degree to the smaller actuators used in other research. It was found that a rounding ratio of  $r/D = 0.5$ , where  $r$  is the rounding radius and  $D$  the orifice diameter, achieved the highest efficiency. This was mainly due to the lack of a throat in the case of  $r/D > 0.5$ , resulting in a lack of flow reattachment as the flow passes over a sharp outside edge. In the other cases, where a small throat is present it was sufficiently long for the flow to reattach to the channel walls and follow the radius creating a wider velocity profile reducing the losses of the actuator. Furthermore, the acoustic power of the SJA, similar to the discharge energy of a PSJA, was found to be a strong function of the orifice geometry. Increasing the ratio  $r/D$  from 0-0.5 the power significantly decreased. A lack of throat, as seen for  $r/D = 1$  caused the acoustic power to rise above the baseline case.

Apart from round orifices some research on slotted orifices have been performed, both rectangular orifices as researched by Watson et al. [51] and Van Buren et al. [49] as well as rounded slots as done by Zong and Kotsonis [60]. The research done by Watson et al. [51] showed that having a rectangular slot resulted in much less coherence of the jet and even showed signs of turbulence where a circular jet would not. This phenomenon was experienced in aspect ratios of 5 and 1.25 indicating that this is a property of rectangular orifice geometries in general. Apart from an early transition to turbulence it was found that, in contrary to circular geometries, a slight difference between the shape of the jet and the orifice was present, orifice it must initially be in the shape of that orifice. This suggests that the fluid exiting the orifice immediately begins to arrange itself so as to eliminate any regions that have high rates of strain, ostensibly the fluid exiting from the orifice corners and create an axisymmetric ring. As the amount of fluid leaving the rectangular orifice is similar to the circular geometry the vortex rings of both geometries are very similar. However, due to the fact that the rectangular geometry produces a more turbulent jet it is expected to achieve higher entrainment levels than the laminar ring produced by the circular geometry. This suggests that higher levels of vorticity are present, though the amount of dissipation is also higher due to the turbulent nature of the jet, meaning that for rectangular jets the coherent vortex structures will persist in the flow for a smaller amount of time. It is therefor assumed that rectangular orifice geometries are better suited for applications in which the injection of coherent vorticity into a flow is of lesser importance than the increased mixing these geometries achieve. Van Buren et al. [49] went into more depth when investigating the effect of aspect ratio. It was found that increasing the aspect ratio of a rectangular jet result in a more two-dimensional behaviour of the jets as the effect of the edge vortices decreases. However, maximising the aspect ratio is not always the best idea as the highest jet velocity was achieved at  $AR = 12$ , whilst the largest momentum addition occurred for the  $AR = 18$  case.

Also in the case of the rounded slot used in the experiments by Zong and Kotsonis [60], a similar behaviour to the rectangular orifices is found, as it reported an entrainment rate significantly higher than its circular counterpart, sharing the same orifice area. This higher entrainment rate resulted in a slower moving jet front, though the jet exit velocities remain similar for both geometries. Furthermore, quasi-2D flow fields were reported for the slotted orifice as also noted by Van Buren et a. [49].

### 1.3. Knowledge gaps.

When it comes to active flow control several techniques are able to significantly enhance flows around airfoils and ramps. However, with most aeronautical applications operating at transonic flow regimes and at high Reynolds numbers some serious hurdles need to be overcome for these techniques to become applicable in these settings. Section 1.1.2 went into detail what techniques are currently available and DBD actuators have shown great promise when it comes to separation control at low-moderate Reynolds numbers, but some researchers doubt their applicability at other flow regimes due to their lack of generating high velocity electric winds. Though research performed by Xin et al. [52] and Moreau et al. [35] show that DBD actuation might be a viable option at moderate Reynolds numbers ( $\mathcal{O}(10^6)$ ) no breakthroughs have been reported at Reynolds numbers similar to passenger aircraft ( $\mathcal{O}(10^7)$ ).

With the introduction of synthetic jet actuation implementation in aeronautical applications seemed a step closer as the high jet velocities reached by synthetic jets have proven to combat moderate adverse pressure gradients at Reynolds numbers of  $\mathcal{O}(10^7)$ , hinting at their performance for even more demanding flight scenarios. However, research performed by Kim and Kim [29] reported that the effectiveness of SJ actuation is limited to velocities lower than the peak jet velocities rendering them unfit for transonic flow conditions, but with the recent introduction of plasma synthetic jets this hurdle might have been passed as typical jet velocities exceed 300 m/s as proven by various jet characterisation experiments. With these high jet velocities PSJ actuation promises good flow control abilities at high Reynolds number and transonic flow conditions. This has been backed up by research in which PSJ actuation is able to reduce separation regions in supersonic flows of  $M = 3$ .

With PSJ actuation hinting at high speed and high Reynolds number flow control, but lacking sufficient research to back these claims up, a good opportunity for further research has been found. Due to the recent introduction of PSJ actuation several knowledge gaps are present that need to be filled before research moves on to more industrial applications. These gaps can be classified in two major fields being the improvement of the PSJ actuator itself and the implementation of PSJ actuation in aerodynamic models to find its working mechanisms of separation control. This thesis will try to fill in two of these gaps both of which are discussed in more detail below.

#### 1.3.1. PSJA characterisation.

When it comes to the implementation of PSJ actuation in industrial applications the optimal working of PSJAs is required. A major driver in PSJA improvement is enhancing their efficiency, which can be done in numerous ways. A significant amount of research has already been performed on the effect of some geometrical parameters such as electrode distance and orifice area, a knowledge gap is present when it comes to orifice shapes, especially the introduction of cone angles. Though Caruana et al. [6] already showed that cone angles can enhance the refill stage of PSJ actuation and Nani [36] found similar results, their research lacks characterisation experiments on the effect of angle on small orifices. Furthermore, their research has only focused on converging geometries, leaving the effect of diverging nozzles on PSJA enhancement. This poses the question: *‘How does cone angle affect the performance of plasma synthetic jet actuators?’*

In order to answer this question part II of this thesis will extensively discuss a jet characterisation experiment in which the cone angle is varied. In this experiment several converging cone angles being,  $90^\circ$  (baseline case),  $60^\circ$ ,  $45^\circ$  and  $30^\circ$  will be analysed on their effect on the performance parameters as well as the vorticity generated. Apart from the converging geometries, two special cases having a diverging section within the geometry are tested as well. One of these geometries incorporates a purely divergent nozzle,  $-30^\circ$ , and another one has a converging and diverging section,  $\pm 30^\circ$ .

#### 1.3.2. Flow separation control experiment.

Apart from the improvement of the actuators themselves a better understanding of the working mechanism behind PSJ actuation is required before research can move on to more applicable flow conditions for passenger/military aircraft. Several papers have already discussed how PSJAs are able to decrease flow separation of compression ramps in supersonic flow as well as diverging ramps in subsonic flow, but the topic of active flow control on airfoils is mostly overlooked. Though the implementation of PSJ actuation on a NACA 0015 airfoil has been performed by Caruana et al. [6], their placement of the PSJA array, at  $x = 0.32c$ , rendered the entire setup only able to combat localised trailing edge separation. However, in order to see how PSJ actuators compare to synthetic jet actuators a similar

experiment as performed by Gilarranz et al. [19] is required in which the array has been moved further to the leading edge. With the help of PIV measurements such an experiment can answer the question: *How can plasma synthetic jet actuation effectively control large scale leading edge separation of a NACA 0015 airfoil?*

This thesis will try to answer this question in part III in which wind tunnel experiments on a NACA 0015 airfoil with and without actuation are performed.

#### 1.4. Thesis lay-out.

As mentioned in section 1.3 this thesis will try to improve knowledge about PSJ actuation in two different fields, being the improvement of actuator geometry knowledge as well as getting a better insight in the flow mechanics of separation control by PSJ actuation.

Part II will research the effect of orifice geometry on the performance of PSJAs. Chapter 2 will discuss the test setup how this experiment is performed and chapter 3 will discuss its results. In chapter 4 the general findings on how orifice geometry affects PSJA performance will be shared.

The flow separation experiment, in which a PSJA array is used to control the flow around a NACA 0015, will be discussed in part III of this thesis, where in chapter 5 the methodology of this experiment is laid out. The general results of how PSJ actuation is able to enhance the aerodynamic performance of the NACA 0015 model are shown in chapter 6. The concluding remarks about this experiment are discussed in chapter 7.

# II

PSJA characterisation.



# 2

## Methodology.

Knowing how the orifice geometry affects the performance of PSJ actuation is of crucial importance when optimising these kind of actuators. During this experiment several geometries are tested in order to see if certain orifice geometries are able to enhance the performance of PSJ actuation.

### 2.1. Measurement techniques.

During the jet characterisation experiment two types of data have been recorded. PIV is used to characterise the flow fields created by the jets and the electrical measurements are performed to detect the discharge waveforms of the PSJ actuator. Both of these measurement techniques are discussed in sections 2.1.1-2.1.2.

#### 2.1.1. PIV measurements.

In order to see how the jet develops after actuation takes place Particle Image Velocimetry (PIV) is used to detect the instantaneous flow fields. These flow fields are detected with the use of olive oil particles fed by an atomiser that injected its particles both directly into the bottom of the PSJ actuator as well as the quiescent room the experiment took place in. This allowed for an even distribution of the particles inside the jet and its direct surroundings allowing for accurate flow fields. The laser used to visualise the flow fields is an Evergreen II laser which created a laser sheet with a thickness of  $t_{ls} \approx 0.5 \text{ mm}$ , passing the centre of the orifice such that the core of the jet is visualised. The PSJA, laser and the camera, a LaVision Imager LX (2 Mp) camera with a Nikkor 200mm f/4D IF-ED lens, are timed using a LaVision PTU, such that the phase-locked flow fields are recorded. At each phase 200 images were recorded to ensure statistical convergence.

#### 2.1.2. Electrical measurements.

The discharge waveforms experienced by the PSJ actuator have been measured using a high voltage probe (LeCroy, PPE20kV) and a current monitor (Pearson, Model 325). Both waveforms have been recorded using an oscilloscope (Tektronix, TDS 3054 C) with a sampling frequency of  $f_s = 0.1 \text{ GHz}$ , such that accurate discharge waveforms are ensured.

### 2.2. Experimental setup.

The jet characterisation experiment took place on the plasma table, at the High Speed Lab of the faculty of Aerospace Engineering of the TU Delft. On this table, which is electrically grounded and perfectly horizontal, a perspex box is placed in which the experiment took place. This box, approximately  $0.5 \text{ m} \times 0.5 \text{ m} \times 1 \text{ m}$  in size, allows for testing in quiescent flow conditions such that no external effects, other than PSJ actuation, are encountered during the jet characterisation experiments. The actuator model and the electrical circuit are discussed in more detail in sections 2.2.1-2.2.2.

### 2.2.1. Actuator model.

In figure 2.1 the PSJ actuator used in this experiment is shown. The actuator, machined out of a block of glass ceramic called MACOR, has a cavity diameter of  $D_{ca} = 12 \text{ mm}$  and a cavity depth of  $h_{ca} = 15 \text{ mm}$ , resulting in a cavity volume of  $V_{ca} = 1.69 \cdot 10^{-6} \text{ m}^3$ . At the bottom of the actuator a small hole, connected to the atomiser is used to feed oil particles directly into the actuator such that enough seeding is present within the jet. The electrodes, placed halfway into the actuator, had a thickness of  $t_e = 1 \text{ mm}$  and the air gap between the electrodes was  $d_e \sim 4 \text{ mm}$ . The electrodes itself have been electrically connected as discussed in section 2.2.1.

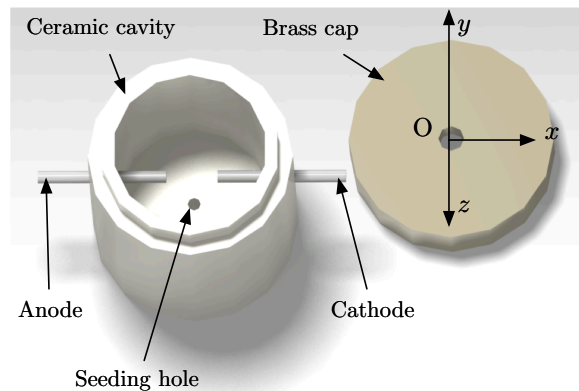


Figure 2.1: Actuator structure: Ceramic cavity (left) and brass cap (right).

The caps, machined out of brass, were varied throughout the experiment as to determine how orifice geometry affects the jet expulsion phase of the actuator. In total six different geometries have been tested to find their varying behaviour. Four of these caps had regular, converging, orifice geometries at various angles being:  $90^\circ$ ,  $60^\circ$ ,  $45^\circ$  and  $30^\circ$ . However two special caps had been designed to see if unconventional orifice shapes had any additional effects during the jet expulsion phase. One cap had a diverging orifice with an angle of  $30^\circ$ , which will be referred to as the  $-30^\circ$  nozzle. The second unconventional cap was equipped with a converging-diverging orifice with angles of  $30^\circ$ , which will be referred to as the  $\pm 30^\circ$  nozzle. The thickness of the caps were  $t_c = 2 \text{ mm}$  and the throat diameter for all caps was  $D_o = 2 \text{ mm}$  as well. Figure 2.2 shows a schematic representation of the various caps used.

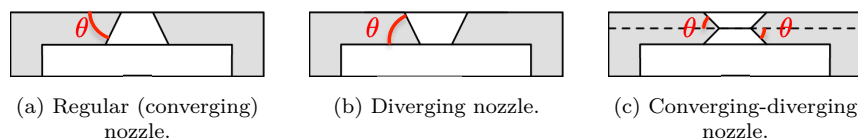


Figure 2.2: Three types of caps used, with  $\theta$  being the cap angle.

Table 2.1 shows a summary of the most relevant input parameters for this experiment.

$V_{ca} [\text{mm}^3]$	$D_o [\text{mm}]$	$t_e [\text{mm}]$	$d_e [\text{mm}]$	$U_0 [\text{kV}]$	$C [\mu\text{F}]$	$E_d [\text{mJ}]$	$\varepsilon [-]$
1696	2	1	4	18	0.1	417.2	0.937

Table 2.1: Input parameters for the PSJA.

### 2.2.2. Electrical circuit.

In order to operate the PSJ actuator a complex electrical circuit is used to ‘fire’ the actuator. This pseudo-trigger circuit, which is shown in figure 2.3, consists of two different power supplies that are separated by diodes. This allows for a sequential discharge of the actuator such that it experiences a trigger-discharge followed by a capacitive discharge, [14, 40, 59]. During the trigger discharge phase, the high voltage (HV) power supply ‘triggers’ an arc between the electrodes of the PSJ actuator as the

voltage of the HV generator is higher than the breakdown voltage of the air gap between the electrodes,  $U_{HV} > U_{bd}$ . However the power supplied by this generator is not sufficient to sustain the arc and create a strong jet, but once an arc has been established gas surrounding it is ionised allowing a larger current to move between the electrodes. As the surrounding gas is ionised more the effective resistance to cross the air gap decreases and allows the low voltage (LV) part of the circuit to deposit its energy in the capacitive discharge phase. Whilst the HV generator established an arc the LV generator has been charging a capacitor bank,  $C1$ . Once the resistance between the electrodes has dropped the capacitor bank deposits all its stored energy into sustaining the arc and heating its surrounding air. It is during the capacitive discharge phase that the pressure inside the cavity rises enough to create a strong jet. The resistors used in the circuit,  $R1$  &  $R2$ , are to prevent any short-circuiting to occur during discharge.

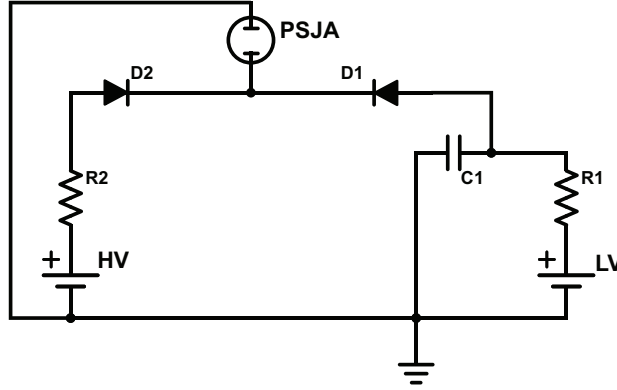


Figure 2.3: Electrical circuit.  
 $R1 = 100\Omega$ ,  $R2 = 100\Omega$  &  $C1 = 1\mu F$

The discharge energy is computed from the capacitor energy times and a discharge efficiency. With the LV generator operating at  $2\text{ kV}$  the energy stored in the capacitor was found to be  $E_c = 1/2 \cdot 1 \cdot 10^{-6} \cdot (2 \cdot 10^3)^2 = 2\text{ J}$ . With typical discharge efficiencies according to Zong et al. [59] being around 30% this would result in  $E_d \approx 600\text{ mJ}$ . However, due to the large electrode distance chosen this efficiency is estimated to be lower as larger electrode distances, according to Zong et al. [63], result in lower discharge times and therefore smaller discharge energies. Therefore a discharge efficiency of 20% is chosen resulting in a discharge energy of  $E_d \approx 400\text{ mJ}$ .

In order to relate the energy put into the actuator with the internal energy of the gas the energy disposition ratio is required, which is computed as ([59]):

$$\varepsilon = \frac{E_d}{E_g} = \frac{\int_0^{T_d} U_d I_d dt}{C_v \rho_0 V_{ca} T_0} \quad (2.1)$$

Since the testing was performed under ambient conditions the internal energy of cavity gas is  $E_g = 427\text{ mJ}$ . This resulted in a non-dimensional energy disposition of  $\varepsilon = 0.937$ , showing that the energy inside the cavity is nearly doubled after actuation has taken place.

### 2.3. Post processing.

After all measurements have been performed the PIV data have been processed using Davis 8.3.1 software. The images were processed using conventional cross-correlation. In order to ensure a good resolution multiple passovers with decreasing window size have been performed. The minimum window size used was  $16 \times 16$  with a 75% overlay resulted in a resolution of 13.5 vectors per  $mm$ .



# 3

## Results.

This chapter discusses the results obtained from the jet characterisation experiment with varying orifice geometry. It is divided into two parts being the phase averaged flow fields of the jet (section 3.1) and its performance parameters derived from these flow fields are dealt with in section 3.2.

### 3.1. Phase averaged velocity fields.

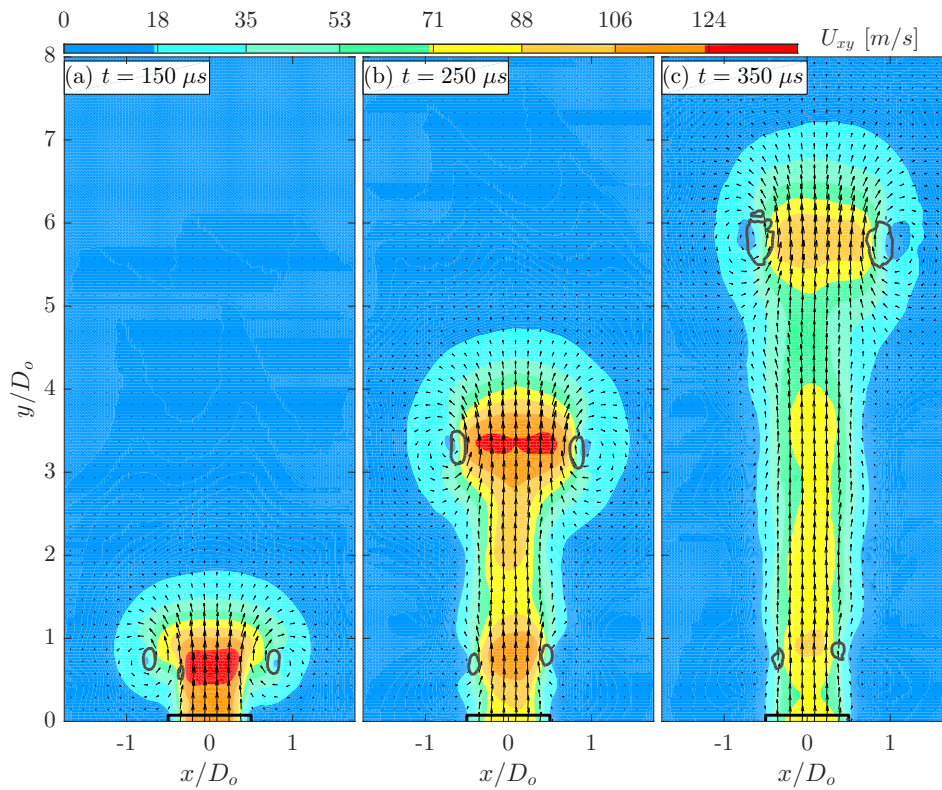


Figure 3.1: Phased average velocity fields at various times after discharge of the baseline case of  $\theta = 90^\circ$ .  $U_{xy}$  is the Euclidean sum of the two velocity components such that  $U_{xy} = \sqrt{u^2 + v^2}$ , the black box denotes the orifice location and the dark grey contours are the Q-criterion of  $Q/Q_{pk} = 0.25$ . The red dashed line shows the division between the up- and downward moving air and the red dot represents the location of the stagnation point.

In order to have a reference the phase averaged velocity fields of the baseline geometry,  $\theta = 90^\circ$ , is shown in figure 3.1, where the  $t$  denotes the time after discharge. As can be seen at  $t = 150 \mu s$  a jet exits the orifice lead by a distinctive vortex ring. This vortex ring, which, which is due to the roll-up of

the boundary layer vorticity, is significantly wider than the jet and its core experiences higher velocities than the current exit velocity.

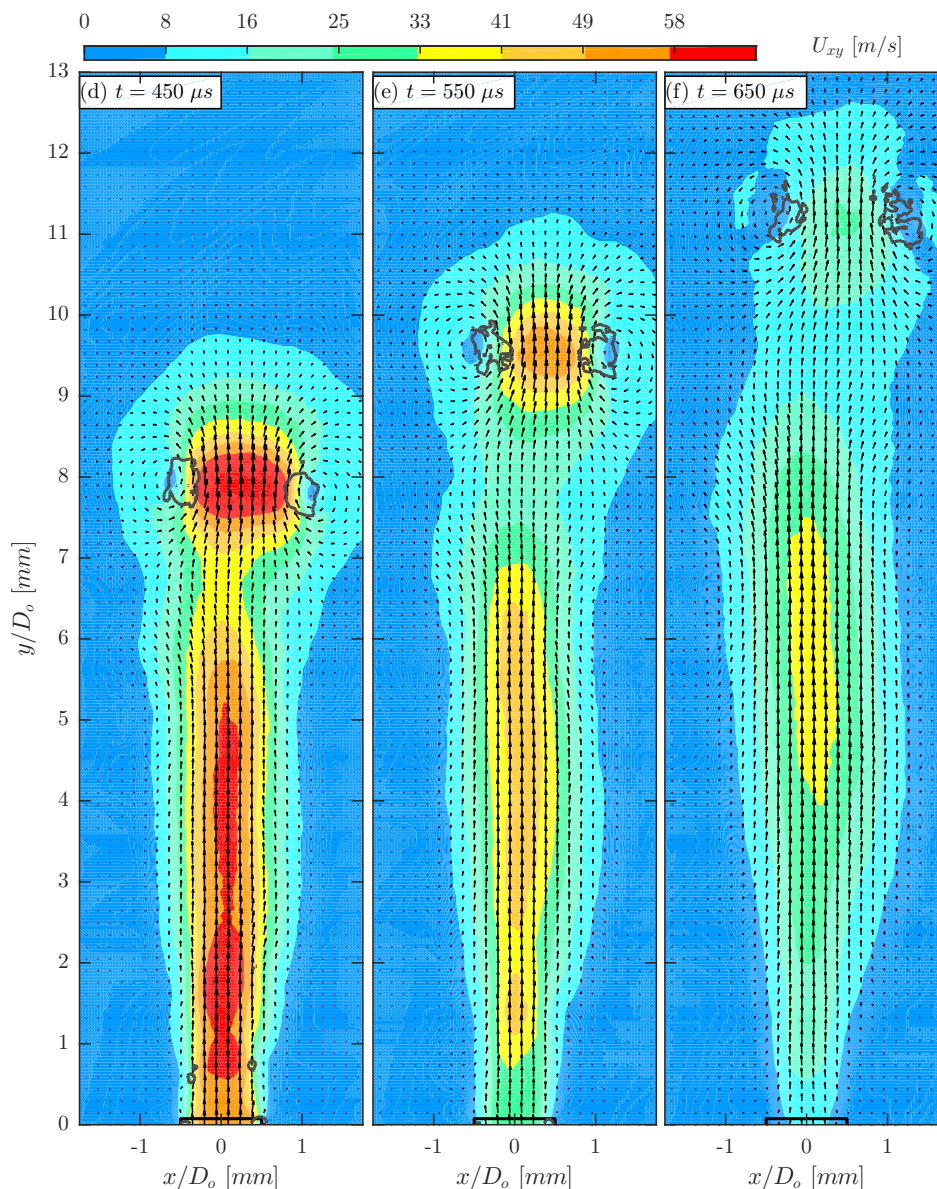


Figure 3.1: Phased average velocity fields at various times after discharge of the baseline case of  $\theta = 90^\circ$ .  $U_{xy}$  is the Euclidean sum of the two velocity components such that  $U_{xy} = \sqrt{u^2 + v^2}$ , the black box denotes the orifice location and the dark grey contours are the Q-criterion of  $Q/Q_{pk} = 0.25$ . The red dashed line shows the division between the up- and downward moving air and the red dot represents the location of the stagnation point.

Furthermore, the effect of viscosity can be seen as the velocities in the core of the jet are significantly higher than the velocities close to the orifice wall, indicating that a boundary layer is present within the orifice. This boundary layer is the result of the wall shear stress that causes a velocity gradient close to the wall effectively reducing the orifice size as the majority of the flow now has to pass through a smaller effective orifice area [5].

At  $t = 250 \mu s$  the vortex ring has moved away from the orifice and has grown in size whilst its core velocity is slightly reduced. Furthermore, another Kelvin-Helmholtz instability is seen around  $y/D_o \approx 0.75$ . This process is continued up to  $t = 650 \mu s$ , where the vortex ring has significantly increased in size, but its core velocity has reduced to roughly 25% of its initial velocity. Furthermore, the secondary vortex rings created by the KH instabilities at earlier time intervals have now fused with one and other. Where at  $t = 350 \mu s$  individual KH instabilities can be seen at  $y/D_o \sim 0.8$  and

$y/D_o \sim 4$ , at  $t > 350 \mu s$  these seem to have fused into one and other resulting in a fully turbulent jet [38]. This effect results in the transfer of momentum of the high momentum jet to its low momentum surroundings, causing the jet to diffuse as can be seen at  $t > 550 \mu s$ , where the jet width increases to three times of exit orifice diameter when it propagates to  $y/D_o \sim 8$ .

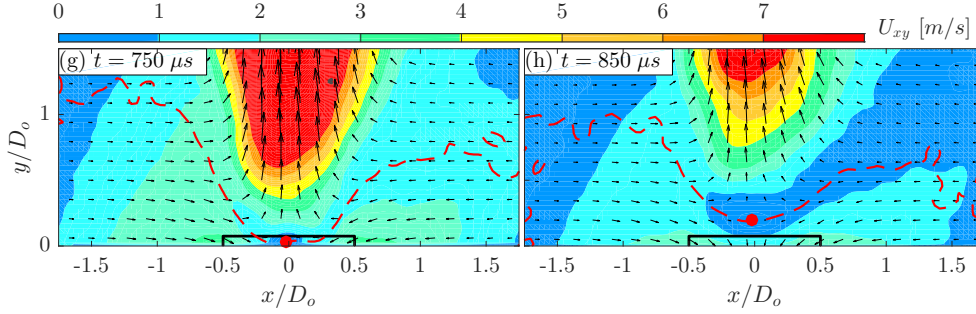


Figure 3.1: Phased average velocity fields at various times after discharge of the baseline case of  $\theta = 90^\circ$ .  $U_{xy}$  is the Euclidean sum of the two velocity components such that  $U_{xy} = \sqrt{u^2 + v^2}$ , the black box denotes the orifice location and the dark grey contours are the Q-criterion of  $Q/Q_{pk} = 0.25$ . The red dashed line shows the division between the up- and downward moving air and the red dot represents the location of the stagnation point.

As the jet exit velocity decreases with increasing time, which is due to the fact that the driving force of the jet, the cavity pressure,  $p_{ca}$ , is dropping as more mass is expelled. After approximately  $700 \mu s$  the cavity pressure has dropped enough to start the suction phase of the PSJ actuator. This effect is seen at  $t = 750 \mu s$ , where air close to the PSJ actuator is sucked back into the cavity, though the remnants of the former jet are still visible by the air moving upward at  $y/D_o > 0.2$ . A bit deeper within the suction phase,  $t = 850 \mu s$ , the tail of the jet has moved further upwards and a clear stagnation point, marked by the red dot, shows the division of the upward moving air and the air being sucked into the cavity.

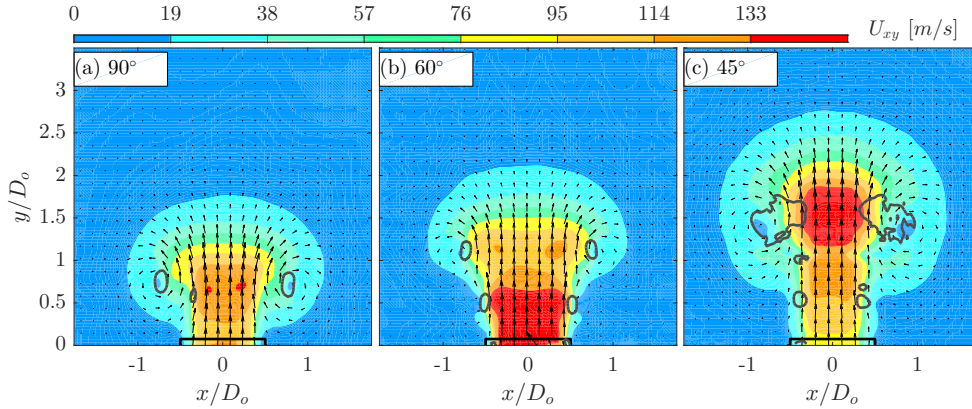


Figure 3.2: Phase averaged velocity fields of all orifice geometries at  $t = 150 \mu s$ . The plotting methods are copied from figure 3.1.

Figure 3.2 shows the phase averaged velocity fields at  $t = 150 \mu s$  after discharge for each orifice geometry. Comparing the converging orifice geometries (figures 3.2 (b)-(d)) with the baseline geometry (figure 3.2 (a)), one can see that all conventional geometries behave similarly by having a strong jet led by a vortex ring. However, the jets of the converging nozzles have developed further than the baseline case. Looking at figures 3.2.a-d a decrease in cone angle,  $\theta$ , leads to more developed jets as the vortex front, taken as the top of the vortex where  $U_{xy} = 19 \text{ m/s}$ , increases from  $y_{vf}/D_o = 1.7$  to  $y_{vf}/D_o = 3$  from  $\theta = 90^\circ$  to  $\theta = 30^\circ$  respectively. As these jets are more developed also more secondary vortex rings evolved from the KH instabilities are noticed for  $\theta = 60^\circ$ ,  $\theta = 45^\circ$  and  $\theta = 30^\circ$ . Especially in the case of the latter the jet seems less stable than the other conventional geometries resulting in stronger secondary vortex rings as seen from the larger Q-criterion contour at  $y/D_o \approx 0.75$  has developed into

a secondary vortex ring. Because of their proximity and the fact that their direction of rotation is the same the inward moving flow at the bottom of the front vortex ring is combated by the outward moving flow at the top of the secondary vortex ring effectively restricting the growth of both vortices. This results in the fusion of the front vortex ring with the jet preventing it from having the clear ‘mushroom’ shape the other nozzle geometries have.

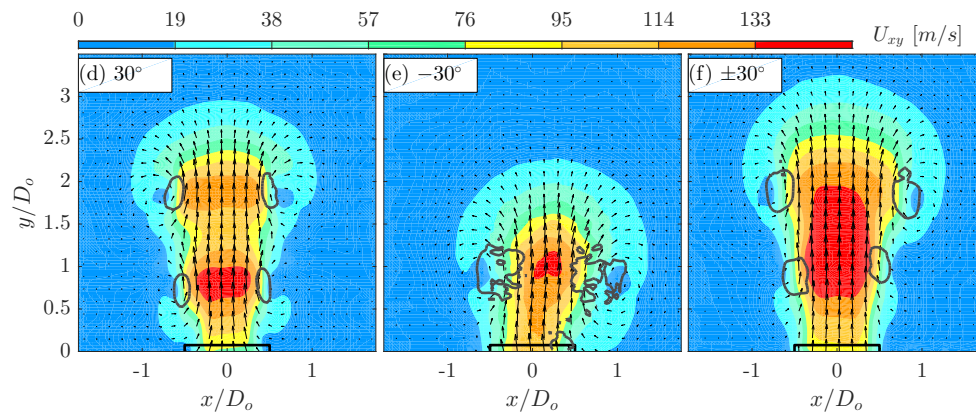


Figure 3.2: Phase averaged velocity fields of all orifice geometries at  $t = 150 \mu\text{s}$ . The plotting methods are copied from figure 3.1.

Looking at the diverging nozzle (figure 3.2 (e)), one can see that the traditional mushroom shape of the baseline case has vanished. Though a vortex ring can still be seen a distinction between the jet and the vortex ring can not be made. Though the general shape of the jet is different to the conventional geometries, the velocities within the core of the jet are similar to that of the baseline case. Furthermore, the core of the jet-vortex combination is slightly angled towards the right, which does not occur for any other geometry. The converging-diverging geometry (figure 3.2 (f)) conforms more to the mushroom shape experienced by the converging nozzles albeit less prevalent than for  $\theta \geq 45^\circ$ . Similarly to  $\theta = 30^\circ$  this is due to the fact that KH instabilities grow into secondary and tertiary vortex rings restricting each other in their growth.

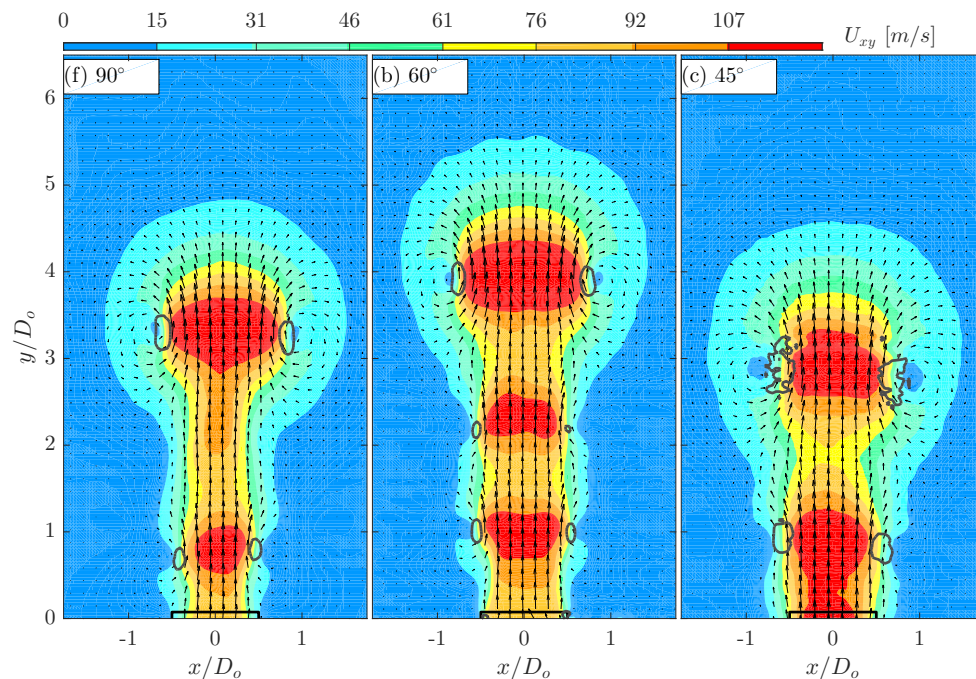


Figure 3.3: Phase averaged velocity fields at  $t = 250 \mu\text{s}$ . The plotting methods are copied from figure 3.1.

Moving on to the averaged velocity fields at  $t = 250\mu s$  in figure 3.3 one can see that the jet has developed further. Though all converging nozzles show a distinct vortex ring leading a jet, all jets have become unstable and show KH instabilities forming into secondary and tertiary vortices as shown in figure 3.4 in which a tertiary vortex ring is depicted for  $\theta = 60^\circ$ . These additional vortices show local velocity maxima in the jet as clearly seen in all conventional geometries. Furthermore, the trend of the vortex front being more developed for smaller cone angles seen in figure 3.2 has disappeared as both  $\theta = 90^\circ$  and  $60^\circ$  have caught up with  $\theta = 45^\circ$ , though the  $\theta = 30^\circ$  nozzle is still ahead of the other geometries.

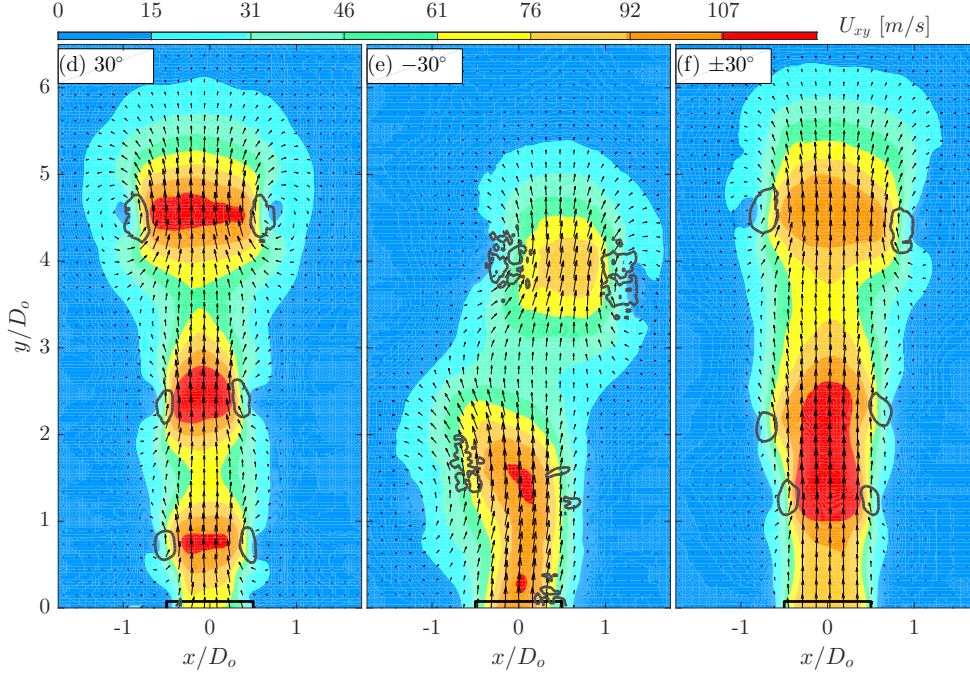


Figure 3.3: Phase averaged velocity fields at  $t = 250\mu s$ . The plotting methods are copied from figure 3.1.

Looking at the jet of the diverging nozzle (figure 3.3 (e)), it hardly resembles the jets seen for the conventional geometries. Though a vortex still leads the jet it experiences much smaller velocities and is skewed towards the right. The jet itself also seems disconnected between the vortex, which, when comparing the instantaneous velocity fields, is often the case. Contrary to the other geometries it was found that the diverging nozzle often ‘shoots’ out a plume of air spreading in every direction rather than a focused jet. This makes sense as it essentially acts as a funnel spreading the outward flow rather than focusing it. The converging-diverging nozzle (figure 3.3 (f)), does not seem to experience this problem as much as it still shows similarities with the conventional geometries. However, its front vortex ring is less prevalent and weaker as its core velocity is lower. This is likely influenced by the diverging part of the nozzle. A possibility why the converging-diverging nozzle does not experience this ‘funnel’ effect as much as the diverging geometry is because the size of its diverging section of the nozzle is comparatively small with respect to the diverging nozzle still allowing for a relatively focused flow.

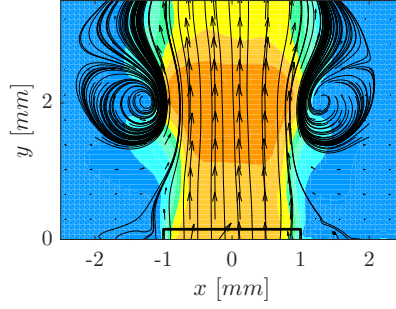


Figure 3.4: Streamlines showing a tertiary vortex ring for the  $60^\circ$  geometry.

At a phase of  $t = 800\mu s$  most geometries experience suction as shown in figure 3.5. For the conventional geometries air is sucked back into the cavity and a clear division between up and downward moving air can be seen. Most of the air is sucked in from the side as the ‘tail’ of the jet has enough momentum to escape the low pressure field close to the orifice. The strongest suction occurs for  $\theta = 60^\circ$ . This is due to the fact that due to its higher jet velocities more air has been expelled creating a stronger vacuum as the air inside the cavity cools down. Research by Caruana and Sheplak [6] confirms the enhanced suction velocities when cone angles are implemented as their research concluded that having cone angles enhanced the suction phase of the PSJ actuator. The only nozzle of which its suction phase has not started is the diverging nozzle that is still blowing out air indicating a much longer jet duration time than the conventional orifice geometries.

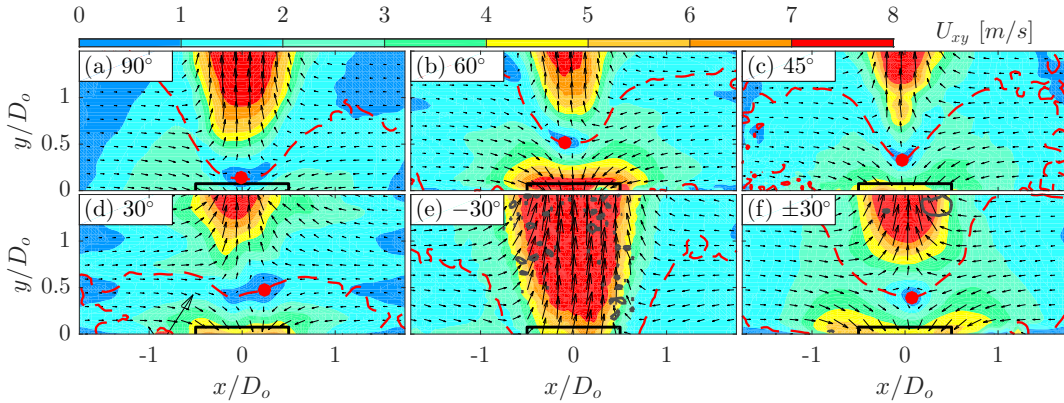


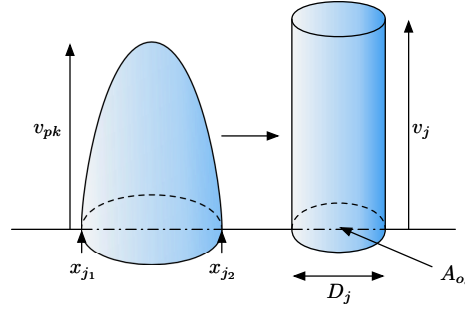
Figure 3.5: Phase averaged velocity fields at  $t = 800\mu s$ . The plotting methods are copied from figure 3.1.

### 3.2. Jet parameters.

Knowing the phase averaged and instantaneous velocity fields of the various orifice geometries it is possible to derive more detailed information from these fields to find the important jet characteristics such that the various geometries can be objectively compared. The jet velocity,  $v_j$ , is one of the most important variables as many other variables depend on this velocity. This jet velocity is the integrated velocity profile normalised by an effective orifice area as schematically represented in figure 3.6. In order to compute this jet velocity the effective orifice area,  $A_{o_e}$ , is required, which is related to the characteristic jet diameter,  $D_j$  as can be seen in equation below.

$$D_j = \int_{x_{j1}}^{x_{j2}} \frac{v}{v_{pk}} dx \quad (3.1a)$$

$$A_{o_e} = \frac{\pi}{4} D_j^2 \quad (3.1b)$$

Figure 3.6: Schematic representation of how  $v_j$  is derived.

Where  $v$  represents the local  $y$ -velocity,  $v_{pk}$  the peak  $y$ -velocity within the velocity profile and  $x_{j1}$  &  $x_{j2}$  are the  $x$ -locations where the physical velocity profile conforms to  $\frac{v}{v_{pk}} > 0.1$ . Having the effective orifice area as well as the velocity profile close to the orifice it is possible to apply a polar integration as shown in equation 3.2 such that the total integrated velocity over the original orifice area is represented by a constant jet velocity over an effective orifice area,  $A_{o_e}$ , as seen in figure 3.6.

$$v_j = \int_{-r_j}^{r_j} \frac{v \cdot \pi \cdot r}{A_{o_e}} dr \quad (3.2)$$

Table 3.1 shows the basic jet parameters derived from the phase averaged flow fields, where  $v_{j_{max}}$  is the maximum achieved jet velocity and  $\bar{v}_j$  is the averaged jet velocity between  $100 - 350 \mu s$ . This time interval was chosen as most of the air is expelled during this time interval, thus the averaged jet velocity is likely to give a better indication of which geometry performs best.  $T_j$  is the jet duration time (the time it takes for the jet exit velocity to reach  $0 \text{ m/s}$ ) and  $\bar{v}_{vr}$  is the velocity of the moving vortex ring leading the jet. In addition figure 3.7 shows the jet velocity curves for each geometry. Starting with the

	$A_{o_e} [mm^2]$	$v_{j_{max}} [\frac{m}{s}]$	$\bar{v}_j [\frac{m}{s}]$	$T_j [\mu s]$	$\bar{v}_{vr} [\frac{m}{s}]$
$90^\circ$	2.00	110.5	79.1	720	49.5
$60^\circ$	2.36	132.7	84.0	630	50.0
$45^\circ$	2.10	126.5	86.1	680	52.5
$30^\circ$	1.99	106.5	67.6	670	54.1
$-30^\circ$	2.72	131.9	84.2	1780	47.5
$\pm 30^\circ$	2.75	122.4	89.6	660	50.5

Table 3.1: Jet parameters for various orifice geometries.

conventional geometries one can see a clear trend as decreasing the cone angle initially results in higher jet velocities but it reaches an maximum as increasing it past a certain cone angle results in decreased jet velocities as was also discussed in section 3.1. This optimum is expected to lie somewhere between cone angles of  $\theta = 60^\circ - 45^\circ$  as the absolute maximum jet velocity is obtained by the  $\theta = 60^\circ$  nozzle, but the highest averaged velocity is reached by the  $\theta = 45^\circ$  nozzle. Either way the jet velocities reached for these two orifice geometries lie very close suggesting that both of them are close to the true optimal orifice geometry. Reducing the cone angle past  $\theta > 45^\circ$  drastically lowers the jet velocity to a point below the baseline case.

Moving towards the unconventional geometries it is surprising to see that they do not underperform the conventional orifice geometries as both obtain high jet velocities, of which the  $\pm 30^\circ$  nozzle even achieves the highest average jet velocity of all cases. However, these high jet velocities are reached with much larger effective orifice areas suggesting that the unconventional nozzles achieve higher outwards volume flows. Furthermore, the jet duration time of the diverging nozzle is significantly longer than all other cases. All geometries have jet duration times of  $T_j \sim 700 \mu s$ , but for the  $-30^\circ$  nozzle this time has increased by 150%. The  $60^\circ$  slightly underperforms with a decrease in jet duration time of  $\sim 10\%$ .

The velocities of the front vortex rings remain similar for all cases with no more than a  $\pm 6.7\%$  deviation from the mean.

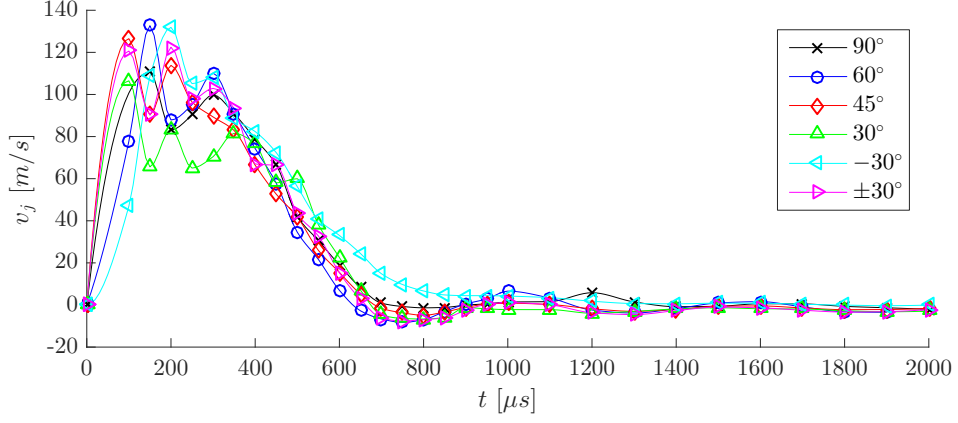


Figure 3.7: Jet velocity curve for all orifice geometries.

Since the intended use of PSJ actuation is the mixing of high and low momentum flows such that phenomena such as flow separation can be combated, their vorticity production is assumed to play an important role. Traditionally the strength of the leading vortex ring is taken as an indicator of the mixing properties of PSJAs, but since some geometries generate relatively strong secondary and tertiary vortices also their total vorticity production is taken into account as seen in figure 3.8. From this figure it can be seen that total produced vorticity is about three times as large as the vorticity of the leading vortex ring. In all cases the vorticity of the vortex ring,  $\omega_{z_{vr}}$ , increases rapidly up to  $t \approx 200 \mu s$ , after which its strength slowly diminishes. This is a similar process as seen from figure 3.1 where the velocities within the vortex decrease as time passes. It was found that converging geometries, especially  $\theta = 60^\circ$  and  $45^\circ$  obtain the strongest leading vortices. The converging-diverging nozzle achieves a similar vortex strength as the baseline case. The weakest leading vortex is obtained by the diverging orifice geometry.

When it comes to the total vorticity produced, all geometries, except for  $\theta = -30^\circ$ , experienced improved vortex production with respect to the  $\theta = 90^\circ$  geometry. Again, the  $\theta = 60^\circ$  and  $45^\circ$  nozzles achieve the highest vorticity production but the  $\theta = 30^\circ$  and  $\pm 30^\circ$  still show a significant improvement with respect to  $\theta = 90^\circ$ . It is likely that the diverging nozzle underperforms with respect to the other cases due to the funnel effect discussed in section 3.1. Contrary to the focused jets ‘cutting’ through the quiescent air and having a clear interface between this static and moving flow, the diverging part expands the air creating a plume. This plume then pushes the air away rather than cutting through and therefore does not have the clean interface the other jets experience for KH instabilities to grow into secondary vortices.

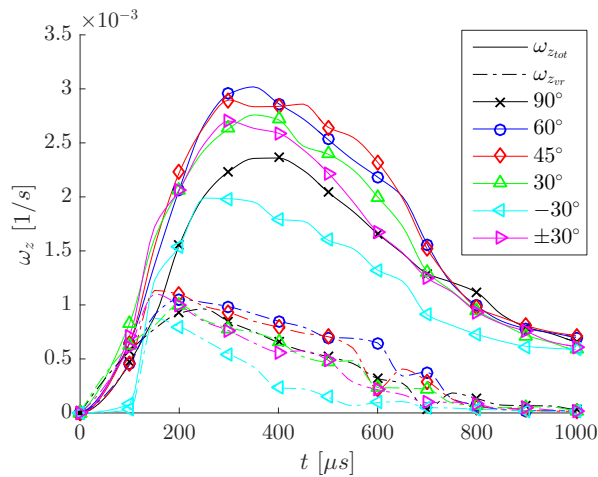


Figure 3.8: The total absolute vorticity (solid lines) and absolute vorticity of the front vortex ring (dash-dotted lines).

Apart from vorticity production and jet velocity several other factors, such as the expelled mass,  $m_e$ ,

jet impulse,  $I_j$ , and the jet mechanical energy,  $E_m$ , are used to quantify the performance of PSJAs. As can be seen from equations 3.3a - 3.3c all these factors are dependent on the jet exit velocity, however also the jet exit density,  $\rho_e$ , plays a significant role, which by itself is dependent on the exit velocity as the density inside the cavity decreases as more mass is expelled.

$$\begin{cases} m_e = \int_0^{T_j} \rho_e(t) v_j(t) A_o dt & (3.3a) \\ I_j = \int_0^{T_j} v_j(t) \cdot \rho_e(t) v_j(t) A_o dt & (3.3b) \\ E_m = \int_0^{T_j} \frac{1}{2} v_j^2(t) \rho_e(t) v_j(t) A_o dt & (3.3c) \end{cases}$$

Though a direct solution for this exit density cannot be found due to a lack of known variables, a simplified model proposed by Zong and Kotsonis [59] is used to find an upper and lower limit of this exit density. These upper and lower bounds to the exit density are shown in equation 3.4.

$$\begin{cases} \rho_e(t) \geq \frac{\rho_0}{f_{UL}(t) \cdot \exp\left(\frac{A_o}{V_{ca}} \cdot \int_0^t v_j(t) dt\right)} & (3.4a) \\ \rho_e(t) \leq \frac{\rho_0}{\exp\left(\frac{A_o}{V_{ca}} \cdot \int_0^t v_j(t) dt\right)} & (3.4b) \end{cases}$$

Looking at the above-mentioned equation one can see that larger orifice areas and jet velocities cause the exit density to drop faster. This makes physical sense since these factors increase the mass flow, which causes the density within the cavity, and the exit density, to reduce faster. The effect of an increased jet velocity can be clearly seen when comparing the exit density of the 90° and 30° geometries, where both cases have similar orifice areas, but an increase in jet velocity results in a larger reduction of the exit pressure. The effect of orifice area is seen when comparing the 60° and -30° geometries where jet velocities are similar, but the larger orifice area of the converging-diverging nozzle results in a steeper decline of the exit density. In all cases the peak ratio of the upper and lower limit of the exit density

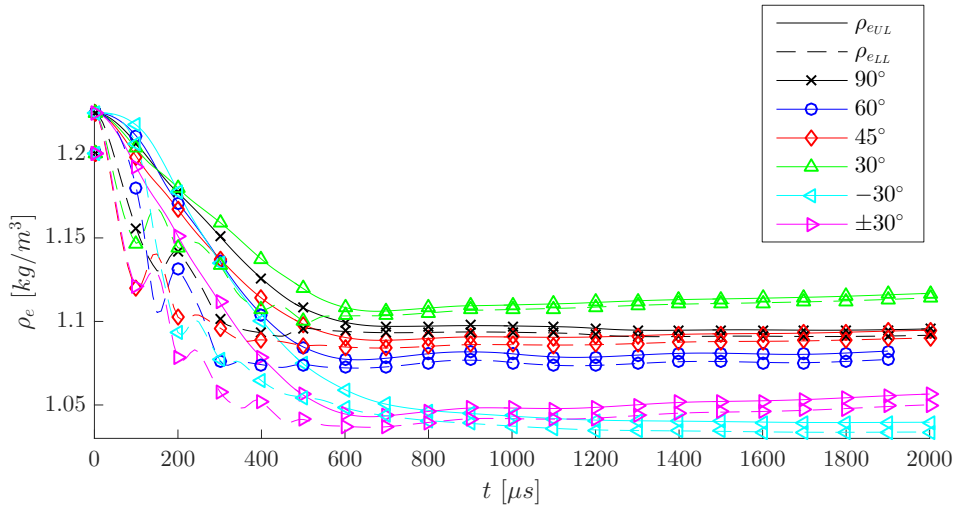


Figure 3.9: Exit density for various nozzle shapes.  $\rho_{eUL}$  (solid lines) and  $\rho_{eLL}$  (dashed lines) are the upper and lower limit of the exit density respectively.

is less than 1.08, leading the maximum relative error to be less than 4% when taking the mean of this density for the computation of the parameters from equation 3.3. Substituting the exit densities within equation 3.3 the above mentioned parameters can be found, however, for comparative reasons their

normalised forms show more insight and are computed as:

$$\left\{ \begin{array}{l} m_e^* = \frac{m_e}{\rho_0 V_{ca}} \end{array} \right. \quad (3.5a)$$

$$\left\{ \begin{array}{l} I_j^* = \frac{I_j}{\sqrt{2E_d \cdot (\rho_0 V_{ca})}} \end{array} \right. \quad (3.5b)$$

$$\left\{ \begin{array}{l} \eta_m = \frac{E_m}{E_d} \end{array} \right. \quad (3.5c)$$

As can be seen, the expelled mass is normalised with the mass inside the cavity,  $\rho_0 V_{ca}$ , but normalising the jet impulse requires more imagination. The quantity  $\sqrt{2E_d \cdot (\rho_0 V_{ca})}$  is found when assuming that the entire discharge energy is converted into kinetic energy from which the velocity can be computed as  $E_d = \frac{1}{2}mv^2 \rightarrow v = \sqrt{\frac{2E_d}{\rho_0 V_{ca}}}$ . Since impulse is  $m \cdot v$  the reference quantity  $\sqrt{2E_d \cdot (\rho_0 V_{ca})}$  is found.  $\eta_m$  is known as the absolute electro-mechanical efficiency, which is the mechanical energy of the jet normalised with the discharge energy. These normalised jet parameters are shown in table 3.2. Due

	$m_e^*$	$I_j$ [ $\mu N \cdot s$ ]	$E_m$ [mJ]	$I_j^*$	$\eta_m$
90°	4.83%-4.99%	8.27-8.58	0.369-0.384	0.628%-0.652%	0.089%-0.092%
60°	5.58%-5.79%	10.10-10.56	0.488-0.512	0.767%-0.801%	0.117%-0.123%
45°	5.14%-5.34%	9.39-9.81	0.453-0.475	0.713%-0.745%	0.109%-0.114%
30°	4.49%-4.60%	6.77-6.96	0.262-0.270	0.514%-0.528%	0.063%-0.065%
-30°	6.99%-7.26%	12.01-12.59	0.591-0.622	0.912%-0.956%	0.142%-0.149%
±30°	6.86%-7.14%	12.94-13.54	0.636-0.667	0.983%-1.029%	0.152%-0.160%

Table 3.2: Key performance parameters of PSJA.

to the fact that the unconventional orifice geometries achieve high jet velocities whilst having a larger effective orifice area, results in them achieving higher performance parameters than their conventional counterparts, with their efficiency nearly  $\sim 70\%$  higher than obtained by the baseline geometry. In absolute terms, the  $\pm 30^\circ$  nozzle achieves the highest performance parameters. When it comes to the conventional geometries the  $60^\circ$  geometry achieves the highest efficiency, though closely followed by the  $45^\circ$  nozzle, indicating that both geometries lie close to the true optimum. The geometry achieving the lowest efficiency is for  $\theta = 30^\circ$ , which is to be expected as it achieved the lowest jet velocity.

Though these performance parameters give a good quantitative indication of how each geometry performs, it does not include the produced vorticity, which is often a critical factor when opting for the best PSJ actuator. In order to account for the vorticity produced another variable is suggested,  $\tau$  [W], which is the product of the total vorticity and the mechanical energy converted by the actuator,  $\tau = \omega_z \cdot E_m$ . Since this variable has the same unit as power, it is normalised by the discharge power of the system,  $P_d = E_d \cdot f_d$ . The results are shown in table 3.3, from which it is seen that the converging-diverging geometry still performs best, but the solely diverging nozzle does not seem the second best alternative any longer. Using,  $\tau$ , as a characterisation parameter shows that the  $\pm 30^\circ$  geometry is closely followed by the  $60^\circ$  geometry as it produces significantly more vorticity, but is not able to efficiently convert electrical energy into mechanical energy.

	90°	60°	45°	30°	-30°	±30°
$\tau$ [ $\mu W$ ]	1.776	3.016	2.690	1.469	2.412	3.520
$\tau/P_d$ [-]	$0.426 \cdot 10^{-5}$	$0.723 \cdot 10^{-5}$	$0.645 \cdot 10^{-5}$	$0.352 \cdot 10^{-5}$	$0.578 \cdot 10^{-5}$	$0.844 \cdot 10^{-5}$

Table 3.3: Suggested PSJ characterisation parameter.

# 4

## Conclusion

As seen from chapter 3 orifice geometry does affect the performance of PSJ actuators. Several kinds of geometries have been tested varying from the conventional converging geometries to the unconventional diverging and converging-diverging nozzles. Comparing the converging geometries with the baseline case of  $\theta = 90^\circ$  a clear performance trend in jet velocity and vorticity production, likely peaking between  $45^\circ \leq \theta \leq 60^\circ$ , is found. At these geometries the maximum achieved jet velocities and vorticity production lie about  $\sim 20\%$  higher than the baseline case. Furthermore it was found that decreasing the cone angle results in a slightly larger effective orifice area, which, together with the higher jet velocities reached, resulted in larger mass expulsions. The specific impulse and electro-mechanical efficiency are also improved by  $14\% - 22\%$  and  $23\% - 33\%$  respectively. The improved efficiency together with the larger amount of vorticity produced show that these cone angles can significantly improve PSJ performance for industrial applications.

Decreasing the converging angle past  $\theta > 45^\circ$  results in a performance drop. In the case of  $\theta = 30^\circ$  the jet velocity drops even below the baseline case resulting in a  $7.4\%$  lower mass expulsion. This lower jet velocity also negatively influences the electro-mechanical efficiency, showing a  $\sim 30\%$  reduction when compared to  $\theta = 90^\circ$ . Though efficiency wise an angle of  $\theta = 30^\circ$  underperforms the baseline case of  $\theta = 90^\circ$  it does introduce significantly more vorticity.

Comparing the unconventional orifice geometries with the conventional ones it was found that adding a diverging part to the orifice can result in effective orifice areas of as much as  $\sim 36\%$  higher allowing for a larger mass expulsions. Though both unconventional nozzles enhance the expelled mass the  $\theta = \pm 30^\circ$  case is of special interest as it has a similar vorticity production whilst having high jet velocities and a larger effective orifice area. Though producing less vorticity than converging geometries of  $45^\circ \leq \theta \leq 60^\circ$ , its enhanced electro-mechanical efficiency makes the product between the mechanical energy and the vorticity produced the highest of all geometries, indicating that adding a small diverging section might be beneficial for PSJA improvement.

The diverging nozzle,  $\theta = -30^\circ$ , does enhance the mass flow and efficiency by similar amount, but the vorticity generated is significantly lower than the other cases rendering it less useful for industrial application where thorough mixing is required. This inefficient production of vorticity is likely due to the diverging section causing the flow to expand in all directions rather than creating a focused jet that slices through the air allowing KH instabilities to form vortices. Furthermore, its jet duration time is also significantly larger limiting the frequency range where this nozzle can be used.

Though each application will favour a specific set of requirements that determines the best actuator for that set of requirements, it was found that, in terms of absolute vorticity production, converging angles between  $45^\circ \leq \theta \leq 60^\circ$  are likely to achieve the best results. However, adding a small diverging section to the orifice does drastically enhance its efficiency whilst still producing a significant amount of vorticity. As only a single diverging angle is tested more research is needed to find optima within the diverging and converging-diverging geometries to see if even better results can be achieved.



# III

PSJA separation control.



# 5

## Methodology.

With the knowledge the plasma synthetic jet characterisation provided a second experiment was proposed to see if an actuator array is able to affect the flow around an airfoil. These series of experiments involved actuator arrays placed within NACA 0015 airfoils and were placed in a wind tunnel to find the aerodynamic performance these arrays can achieve. The experiments are divided into two parts as two different NACA 0015 models have been used, both a different setup of the actuator arrays.

### 5.1. Measurement techniques.

During the wind tunnel experiments multiple types of data have been recorded of which the PIV data as well as the force balance data are most important. In order to link the force balance data to the PIV data electrical data, including the trigger signal, have been recorded. A more detailed description of every measurement technique involved is presented in the sections 5.1.1-5.1.3.

#### 5.1.1. Force balance measurements.

In order to see the macro effects of PSJ actuation on the airfoil performance the aerodynamic forces have been measured using a six-component balance, which was developed by NLR (National Aerospace Laboratory, the Netherlands) in conjunction with the Delft University of Technology. The model was connected to the balance through holding rods that were indirectly connected to a mounting plate. It is assumed that the holding rods are perfectly clamped and that the connection to the balance is rigid resulting in a perfect load transfer between the model to the balance. The balance was able to measure forces and moments with a precision of  $\mathcal{O}(10^{-6}) N$  and  $\mathcal{O}(10^{-6}) N \cdot m$  respectively. This translates to estimated relative errors below 0.1% of the peak lift and drag. Drop tests in which small objects were dropped on the mounting plate of the balance (with the airfoil model was still attached) were performed to check if its response time is adequate for fast dynamic processes, that might be experienced during the experiment. Using a fast Fourier transformation with a balance sampling frequency of  $f_s = 2 kHz$  one can detect frequencies below  $1 kHz$ . From the drop tests most frequencies measured were up to  $100 Hz$ , with some small effects measured around  $840 Hz$  which might be noise or some vibrations in the room itself. Since the maximum actuation frequency used for the experiment is  $f_{ac} = 80 Hz$  the first order harmonics can be detected in all cases and it remains very likely that several higher-order harmonics are captured too.

#### 5.1.2. PIV measurements.

Though the balance data is of great importance to see the macro effects of how PSJ actuation affects the flow and to see at what angles interesting phenomena occur, Particle Image Velocimetry, PIV, is used to visualise these flow fields such in order to get a deeper insight of the working mechanisms behind PSJ actuation.

In contrast to the PSJA characterisation experiment the seeding is directly fed into the wind tunnel, rather than through the actuators themselves. This allowed for an even particle distribution throughout the test section. The fog, created with a SAFEX fog generator placed in the wind tunnel, consisted of a glycol-water mixture as the working fluid creating particles with a diameter of  $D_p \sim 1 \mu m$ .

A chordwise laser sheet, approximately 1 mm thick and located midspan between two actuators, was created using a Quantronix Darwin Duo 527-80-M laser. This laser, capable of very high pulse frequencies, was used in combination with Photron Fastcam SA-1 cameras to capture the flow fields around the NACA 0015 model. The synchronisation of the laser, cameras and actuation system was regulated with a LaVision high-speed PTU and all signals have been saved in order to construct time dependent flow fields. During this experiment two camera setups have been used. One setup to get an overview of the entire airfoil and detect the larger flow structures that might be generated by the PSJ actuation, which will be dubbed as the Large Field Of View (LFOV) setup. This setup is used for the time and phase averaged measurements as well as for the Time Resolved PIV (TRPIV) measurements. The second setup consisted of two cameras that record only a small portion of the flow close to the actuators, this setup will be dubbed the Small Field Of View (SFOV) setup.

The LFOV setup consisted of a single camera on which a Nikkor 105mm f/2.8G IF-ED lens was mounted. The images were recorded with dual frame mode with a recording frequency of 800 Hz with a total of 2728 images. The recording frequency was doubled to 1600 Hz for the SFOV setup. The cameras involved during this setup had Nikkor 200mm f/4D IF-ED lens mounted on them, which allowed for a higher resolution of the flow fields to be recorded. Due to this smaller field of view only a region between  $0 \leq x/c \leq 0.4$  was recorded, but having a higher resolution smaller effects caused by actuation can now be visualised. In both setups the particle size was kept to approximately 2 pixels.

During the TRPIV measurements the same lens as the LFOV was used, however the images recorded were in single frame mode and at a frequency of 4000 Hz for a total of 5456 images.

### 5.1.3. Electrical measurements.

The electrical data recorded included both the current and voltage waveforms of the high voltage amplifier, Trek model 20-20HS, as well as the trigger signal of the cameras. From these signals, which are not directly linked to the flow fields, the phase averaged flow fields can be constructed during post processing. Furthermore, the signals obtained from the amplifier can be used to compute the energy supplied to the actuator array.

Apart from the measurements of the amplifier and camera setup the electric waveforms of the capacitors used in powering the actuator array are measured to compute the discharge energy. This was done with a separate setup involving a high voltage probe (LeCroy, PPE20kV) and current monitor (Pearson, Model 325). The measurements have been recorded by an oscilloscope (Tektronix, TDS 3054 C). In order to ensure an accurate discharge waveforms a sampling frequency of  $f_s = 1GHz$  was used.

## 5.2. Experimental setup.

The active flow control experiments took place in two different tunnels. Both tunnels used were of the open jet type and had a test section of  $0.4m \times 0.4m$  designed to fit neatly onto the wind tunnel exit. The first experiment took place in the M-tunnel, located at the Low Speed Lab at the TU Delft, which had a maximum tunnel velocity of  $U_{\infty_{max}} = 30 m/s$ , however most testing was performed at lower velocities as both the noise and turbulence level increase significantly with higher wind tunnel velocities. The second experiment involved the W-tunnel, located at the High Speed Lab, at the TU Delft. This tunnel was capable of operating at tunnel velocities of  $U_{\infty_{max}} \approx 35 \frac{m}{s}$  and due to the larger contraction ratio the turbulence level is in the order of  $\mathcal{O}(0.5\%)$ . Most of the data presented in this thesis are from this experiment as the flow as well as the model were of better quality resulting in more applicable results.

### 5.2.1. Electrical circuit.

When applying PSJ actuation for large scale aerodynamic surfaces a multitude of PSJAs are required. In order to decrease the complexity of wiring and powering a multitude of single PSJAs would cause a PSJA array is used instead, which only requires a single power source. However, different from dielectric barrier discharge, the resistance characteristic of the arc discharge channel is negative resulting in difficulties generating large area arc discharges as an increase in voltage results in a decreased current. Powering a series of PSJAs without a devices to raise the voltage level above the breakdown voltage in between actuators would require an extremely powerful source of power. Due to the fact that these power sources are not readily available the strong power source would have to be substituted by several smaller sources of power. Though Tie et al. proposed a six channel spark discharge method [48] the

very high trigger voltage of  $40kV$  and very short rise time of  $25ns$  causes this idea to be far from being applied as current technological capabilities are insufficient to operate such a system at a larger scale.

This is why a different setup, proposed by Zhang et al. [56] and Zong and Kostonis [62], is used to power the array of which the electrical scheme is shown in figure 5.1. The major difference between actuators in series, or the setup proposed by Tie et al. [48], is the fact that a ‘virtual relay’, consisting of a large resistor,  $R_p$ , and a small capacitor,  $C_p$ , are placed after every second actuator. This virtual relay, which indirectly connects actuator with the ground allows for a sequential breakdown of the gaps as mentioned by Zong and Kostonis [62] and is designed to match the dynamic impedance of pulsed arcs. The working mechanism of this ‘multi-channel’ discharge scheme, assuming all gaps have been ignited, can be split up in two phases, namely the pre-trigger discharge phase and the capacitive discharge phase.

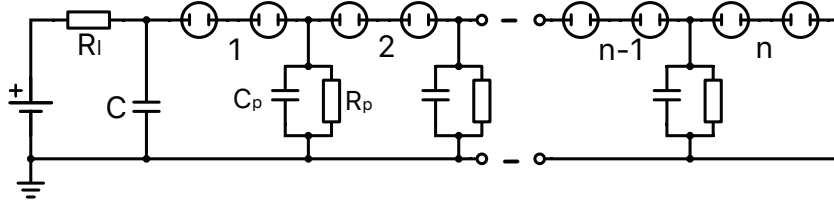


Figure 5.1: Power supply system proposed by Zhang et al. [56].

Each set of 2 actuators are noted by a number and the actuators themselves are modelled as circles with two electrodes inside, also known as a neon lamp symbol.

During the pre-trigger discharge phase high voltage pulses (voltage:  $20kV$  and pulse width:  $3ms$ ) provided by the amplifier, Trek model 20-20HS, are delivered to the energy storing capacitor,  $C$ . Since no arc has been established each of the capacitors in the virtual relays are vacant, meaning that the virtual relays can be treated as short circuits. Thus the voltage over the energy storing capacitor,  $C$ , is only dependent on the first and second gap. In the case of two gaps of  $2mm$  the breakdown voltage,  $U_{bd}$ , is approximately  $U_{bd} \approx 9kV$  [62]. After an arc has been established between the first two gaps the capacitor in first virtual relay,  $C_p$ , is charged by the energy storing capacitor,  $C$ , in less than  $1\mu s$ . The high voltage of the capacitor of the virtual relay is then transferred to the next two gaps, establishing a connection with the next virtual relay. This scenario repeats itself up to the point where an arc has been established for all actuators. Note that after the last set of actuators no virtual relay is placed as there is no need to ramping up the voltage for a next set of actuators. At this point in time the arcs established in the gaps are quite weak in intensity as the energy level is dependent on the capacitive energy within the virtual relay (energy level:  $C_p U_{bd}^2/2$ ) and is mostly sustained by the leakage current through the resistors of the virtual relays,  $R_p$ . When an arc is present in each gap, a closed circuit is formed causing all the energy in all capacitors to be released simultaneously creating an intense capacitive discharge, of which the energy level is dependent on the energy storing capacitor (energy level:  $C U_{bd}^2/2$ ). This capacitive discharge is responsible for most of the heating and pressurising the gas within the actuators. The actuation frequency used for the experiment can be adjusted by varying the discharge frequency accordingly.

As energy is dissipated during the pre-trigger discharge phase the gaps of the first two actuators have been increased to  $3mm$ . This resulted in a higher breakdown voltage of  $U_{bd} = 14kV$  for the first two gaps, but overshoots the breakdown voltage required for the subsequent gaps that have a  $2mm$  spacing. This allows the energy dissipated in the pre-trigger discharge phase to be compensated [62].

The parts used for this multi-channel discharge circuit are given in table 5.1.

part	configuration	part number
$R_l$	$100\Omega$	
$C$	$4nF$	
$C_p$	$110pF$	Murata Electronics ( <i>part no. DHR4E4C221K2BB</i> )
$R_p$	$2M\Omega$	Ohmite ( <i>part no. SM10302-1004-F-E</i> )

Table 5.1: Key parameters electric circuit.

During the second experiment the representative discharge voltage,  $U_d$ , and current,  $I_d$ , waveforms which are shown in figure 5.2. In this figure the above mentioned discharge phases can be detected. Starting at  $t = 0 \mu s$  a pre-trigger discharge is detected as the discharge voltage waveform experiences a staggered declination and the discharge current remains relatively low,  $I_d = \mathcal{O}(10^1)A$ , showing that the arcs are sustained by the leakage current of the virtual relays.

During the capacitive discharge phase, starting at  $t \approx 0.8 \mu s$ , the discharge voltage and current waveforms oscillate periodically and experience damping with a damping coefficient roughly between  $0.23 \leq \zeta \leq 0.36$ . During the capacitive discharge phase a peak current  $I_{d,p} \approx 240 A$  is achieved and the discharge lasts approximately  $2 \mu s$  resulting in a discharge energy of  $E_d = 0.42 J$ , most of which is deposited into the capacitive discharge phase.

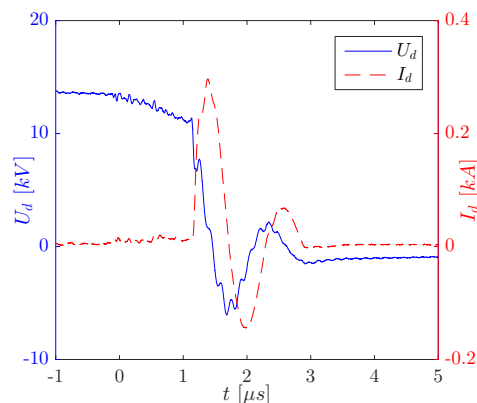


Figure 5.2: Voltage and current waveforms of the PSJA array containing 26 actuators.

### 5.2.2. Model.

Both models used in the wind tunnel experiments involved a NACA 0015 airfoil with a chord of  $0.25m$  and a span of  $0.396m$ , allowing it to fit within the test section mentioned earlier. However the remaining design parameters of both models are quite different which is why both models are discussed separately.

#### X-1.

The NACA 0015 airfoil model has been designed to incorporate three actuation locations at  $x/c = 0.12$ ,  $0.24$  and  $0.36$  respectively. The model was produced via a 3D printing technique using the laser sintering (*a laser-based 3D printing technology that uses solid powder materials whereby a computer-controlled laser beam selectively binds together particles in the powder bed*) of polyamide, which is a strong yet lightweight material capable of withstanding the forces experienced in the tunnel. The holding rods that connect the model with the balance were located at the chordline at  $x/c = 0.3$  as a lack of space prohibited mounting at the aerodynamic centre at  $x/c = 0.25$ .

In this experiment standalone actuators, made of a glass-ceramic composite called MACOR, were machined out of blocks  $15mm \times 15mm \times 100mm$  and had a final dimension of  $15mm \times 15mm \times 10mm$ , see figure 5.3. These were later connected via the multichannel discharge circuit proposed by Zhang et al. [56] discussed in section 5.2.1.

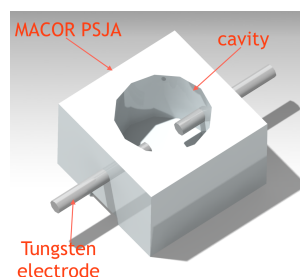


Figure 5.3: Standalone PSJA used for the first experiment.

The dimensions of a single cavity were a cavity diameter of  $D_{ca} = 12\text{mm}$  and a cavity depth of  $h_{ca} = 7\text{mm}$ . This results in a single cavity volume of  $7.92 \cdot 10^{-7}\text{m}^3$ , but as the array consisted of 10 actuators the total cavity volume was  $7.92 \cdot 10^{-6}\text{m}^3$ . The caps for the actuators were produced out of ABS using a 3D print technique called fused deposition modelling (*a filament-based technology where a temperature-controlled head extrudes a thermoplastic material layer by layer onto a build platform*). The orifice diameter was  $D_o = 1\text{mm}$  and the cone angle was  $60^\circ$ . The electrodes had a thickness of  $t_e = 1.5\text{mm}$  and the air gap was  $d_e = 3\text{mm}$ . The NACA 0015 model used is shown in figure 5.4. Though the original plan was to use all tree actuator slots problems with the space as well as the electrical components limited the testing to only the first slot at  $x/c = 0.12$ .

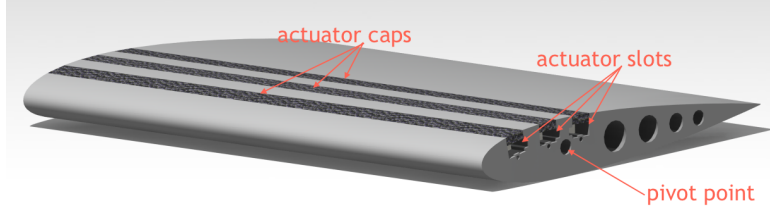


Figure 5.4: X-1 setup.

In order to determine the angle of attack during testing an angle dial with an accuracy of  $\mathcal{O}(1^\circ)$  was mounted to the testing rig.

### X-2.

The second wind tunnel experiment involved an entire redesigned NACA 0015 airfoil, with updated electrical components that lasted longer and with more space accounted for the electrical components. The model, still 3D-printed using laser sintering of polyamide, now only had a single row of actuators and included a sparing in which the electrical components would fit. Rather than cutting individual actuators, entire MACOR rods of  $10\text{mm} \times 10\text{mm} \times 100\text{mm}$  were used to make actuator arrays containing six or seven cavities each, with a spacing of  $14.28\text{mm}$  between the cavity centres, increasing the number of actuators from 10 to 26. For the caps the fused deposition modelling of ABS was replaced by handmade MACOR caps. These caps were made of MACOR sheets of  $3\text{mm} \times 100\text{mm} \times 100\text{mm}$ . In order to span the entire model four array blocks were placed next to each other in the actuator slot on which the caps were placed, creating an almost flush airfoil profile. One of these blocks is shown in figure 5.5.

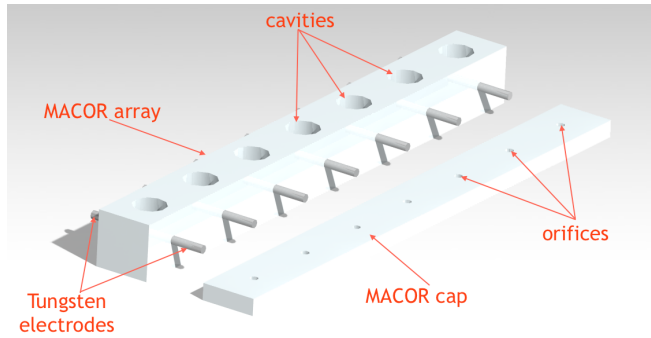


Figure 5.5: PSJA array and cap.

With an increased actuator density their proximity as well as their dimensions had to be reduced with respect to the previous experiment. This led to a cavity diameter of  $D_{ca} = 6\text{mm}$  and a cavity depth of  $h_{ca} = 6\text{mm}$  resulting in a single cavity volume of  $1.69 \cdot 10^{-7}\text{m}^3$  and a total cavity volume of  $4.41 \cdot 10^{-6}\text{m}^3$ , a reduction of 44% with respect to the previous experiment. The orifice diameter one the other hand has been increased to  $D_o = 1.5\text{mm}$  as to affect a larger part of the flow and its cone angle was  $90^\circ$  for simplicity. The electrode thickness was  $t_e = 1.5\text{mm}$  with an air gap of  $d_e = 2\text{mm}$  apart. Since the dimensions of the array has been decreased in size it was possible to move the array

closer to the leading edge of the model to  $x = 0.08c$ . This allows the actuation location to remain in front of the separation point for a higher angle of attack likely enhancing the performance of the array. Furthermore, the holding rods have been moved to the quarter chord location, which corresponds to the location of the aerodynamic centre and an inclinometer, with an accuracy of  $\mathcal{O}(0.1^\circ)$ , is attached to one of these holding rods to measure the angle of attack. This allows for a better accuracy determining the angle of attack when compared to the first wind tunnel experiment.

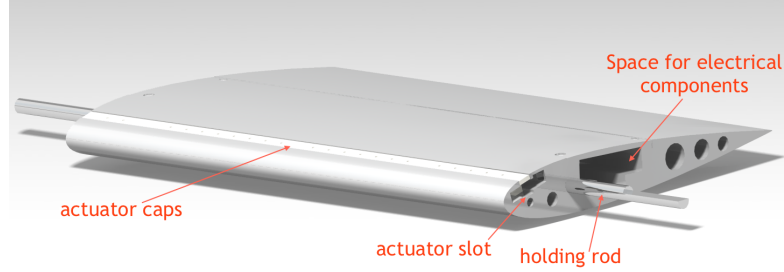


Figure 5.6: X-2 setup.

Also during this second experiment the multichannel discharge circuit was used to supply the 26 actuators of energy and the electrical components were kept the same, with the exception of the discharge capacitor, whose capacitance was increased to  $C = 4nF$ .

#### Jet characterisation.

In a similar fashion as was discussed in part I of this thesis a jet characterisation experiment has been performed on the jets of the array. Contrary to the former jet characterisation experiment only the jet velocity has been computed to get an insight of the most basic jet parameters. Furthermore, due to the missing connection between the PTU and high voltage generator no proper timing of the actuators took place. However, it was assumed that by taking a normal distribution of the jet velocities at each ‘phase’ a good representation of the actual jet velocity is found. Due to the fact that the instantaneous fields showed many fluctuations it was unable to find a realistic effective orifice area or diameter which led to the actual orifice area of  $1.767 \cdot 10^{-6} \text{ m}^2$  to be taken as the reference area.

According to[47] the jet/free stream velocity ratio is defined as:

$$VR = \frac{T_j f_{ac} \bar{v}_j}{U_\infty} = \frac{U_j}{U_\infty} \quad (5.1)$$

where  $U_j = T_j f_{ac} \bar{v}_j$  is the averaged outward jet velocity over an entire actuation cycle. With this definition of averaged outward jet velocity the momentum coefficient is denoted by:

$$C_\mu = \frac{n_a A_o U_j^2}{bc U_\infty^2} \quad (5.2)$$

Where  $n_a$  is the amount of actuators within the model. Operating the model at actuation frequencies between  $4 \text{ Hz} \leq f_{ac} \leq 80 \text{ Hz}$  then results in VRs of  $5.1 \cdot 10^{-2} - 1.02$  and  $C_\mu$ ’s of  $1.269 \cdot 10^{-8} - 5.077 \cdot 10^{-6}$ , much lower than in most SJ actuation experiments, [1, 8, 11]. A summary of the most important jet parameters is shown in table 5.2.

Noteworthy is the low mechanical efficiency of the jets, which is due to the low jet velocity as the mechanical energy is dependent on  $v_j^3$ . This low jet velocity is likely due to the large orifice area chosen in order to affect a larger portion of the flow during the wind tunnel experiments. On the other hand, the large orifice area results in a large expelled mass and a similar specific impulse as the  $90^\circ$  case discussed in part II.

$v_{j_{max}}$ [m/s]	$T_j$ [ $\mu\text{s}$ ]	$m_e^*$	$I_j$ [ $\mu\text{N} \cdot \text{s}$ ]	$E_m$ [mJ]	$I_j^*$	$\eta_m$
30.7	730	11.63%	14.6	0.1897	0.67%	0.0434%

Table 5.2: Key performance parameters of PSJA array (26 PSJAs).

### 5.3. Post processing.

Before being able to use the raw data recorded from the experiments the data needs to be analysed and corrected to increase the likelihood that the measured phenomena correspond to the actual phenomena occurring during testing. In the case for the force balance results wind tunnel corrections and electric noise reduction techniques have been implied which are discussed in section 5.3.1. For the PIV data the raw images have been processed using Davis before further data manipulations have been applied (section 5.3.2).

#### 5.3.1. Force balance corrections.

Since testing of the model took place in a closed test section, the behaviour of the flow around the model is inherently different than free flight where no physical restrictions to the flow are present. This affects the true dynamics of the flow around a model, sketching a different image than reality. However, much research has been performed to correct for these differences and implementing these corrections reduces the differences between free flight and wind tunnel testing as much as possible. The force balance data obtained from the second wind tunnel experiment have been corrected for by solid and wake blockage using the techniques discussed by Maskell [33]. However, the data is only corrected for the blockage effect as other corrections result in a change in angle of attack which removes the relation between the PIV data and the force balance data.

Adding a model to a test section results in a partial blockage of its cross-sectional area, causing the flow around the object to accelerate in order to uphold the mass conservation law. As the wind tunnel velocity is not measured at the model location the measured velocity is different than the velocity at the model location, causing erroneous results, which need to be corrected for. For this particular experiment there are two kinds of blockage to account for, namely solid and wake blockage. Solid blockage is the physical blockage of a solid object in a wind tunnel and wake blockage accounts for the effect of the slow moving air within the wake. In order to account for solid blockage the following equation needs to be used, which depends on the body shape factor,  $K_1$ , the wing volume  $V_w$  and the cross-sectional area of the wind tunnel,  $C$ . The body shape factor, depending on the placement of the model, is between 0.74, in case of a horizontal model, and 0.52 in case of a vertically placed model. Under the assumption that the angles of attack remain small the body shape factor of 0.74 is chosen [12].

$$\varepsilon_{sb} = \frac{K_1 V_w}{C^{1.5}} \quad (5.3)$$

In case of the NACA 0015 model with a chord of  $c = 0.25m$ , the solid blockage was found to be  $\varepsilon_{sb} = 0.0296$ .

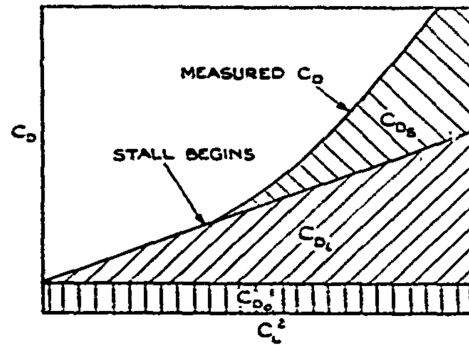


Figure 5.7: Drag analysis of a lifting wing, courtesy of Maskell [33].

Wake blockage requires more complex correction methods as drag consists of different components as seen from figure 5.7. In order to find the components responsible for wake blockage one needs to remove the induced drag, by using a second order polynomial fit through the data points, such that:

$$C_{D_s} = C_D - C_{D_i} - C_{D_0} \quad (5.4)$$

Having the component of the separation drag it has become possible to compute the effect of separation

on the dynamic pressure, which, According to Maskell [33], is given as:

$$\frac{q_c}{q} = 1 + \frac{1}{2} \frac{S}{C} C_{D_0} + \frac{5}{2} \frac{S}{C} C_{D_s} \quad (5.5)$$

However, with the definition used by Dimitriadis [12] being:

$$\frac{q_c}{q} = 1 + 2\varepsilon \quad (5.6)$$

The wake blockage factor is computed as:

$$\varepsilon_{wb} = \frac{1}{4} \frac{S}{C} C_{D_0} + \frac{5}{4} \frac{S}{C} C_{D_s} \quad (5.7)$$

Adding the two blockage contributions together results in the total blockage,  $\varepsilon = \varepsilon_{sb} + \varepsilon_{wb}$ , which when substituted into equation 5.6 results is used to correct the force balance measurements. It was found that post-stall these blockage effects can account for about 20% of the total forces experienced, thus correcting for this results in much more reliable data.

Apart from the blockage corrections the data has been put trough a low pass filter, in order to remove the effect of electric noise on the data. Together with the corrections mentioned above it is assumed that any errors are negligibly small.

### 5.3.2. PIV.

When it comes to the PIV measurements quite some data processes have been performed. First of all the raw recorded images have been processed using Davis 8.3.1 software, using conventional cross-correlation. In order to ensure a relatively high resolution multiple passovers with decreasing window size have been performed of which the minimum window size of  $16 \times 16$  and an overlap of 75% resulted in a resolution of 1.07 vectors per mm.

In order to ensure that the vector images represent reality all outliers have been removed and no interpolation has been used to fill the data points as this would reduce the reliability of the flow fields obtained. In the case of the LFOV and the TRPIV measurements a refraction in the field of view caused erroneous results. This was corrected for by a self-written piece of code that locates this refraction and then interpolates the removed areas such that more realistic velocity fields are obtained. Since this refraction was located close to the trailing edge the SFOV measurements did not suffer from this phenomena and no further manipulation has been performed after exporting it from Davis.

Having the electrical data discussed in section 5.1.3 it has been possible to create both time averaged and phase averaged data. In the case for the time averaged data the velocity fields during the steady stage have been used to create averaged flow fields throughout time, giving a macro overview of the effects of plasma synthetic jet actuation at different frequencies.

The phase averaged flow fields were created with the help of the trigger signal and the electrical signal linking the image to the discharge phase. All images are then distributed to their correct phase and then averaged in similar fashion as the time averaged data. Depending on the actuation frequency about 8 to 170 images correspond to a single phase. Though 8 images might not be enough to ensure statistical convergence it will give an indication of the basic phenomena occurring during such discharge phase.

# 6

## Results.

In this chapter the results of the two wind tunnel experiments using plasma synthetic jet actuation to combat flow separation are discussed. First the macro results such as the lift and drag forces will be discussed in section 6.1, then in section 6.2 the PIV results will be discussed. The latter section is divided into five parts. First the baseline flow fields will be discussed in section 6.2.1. Then the actuated cases will be discussed of which upstream actuation (section 6.2.2) will be discussed first and the flow fields at maximum lift angle of attack ( $\alpha_{C_{Lmax}}$ ) at which downstream actuation is experienced (section 6.2.3) second. Furthermore TRPIV is used to see how the instantaneous flow fields change when starting the actuation or shutting it off (section 6.2.4). Lastly, the time and phase averaged flow fields at a higher free stream velocity will be discussed in section 6.2.5.

### 6.1. Force balance measurements.

This section will discuss the force balance measurements taken during the two wind tunnel experiments, where section 6.1.1 and 6.1.2 will discuss the lift and drag polars of the first and second experiment respectively. Section 6.1.3 will briefly discuss the effect of increasing the amount of actuators and section 6.1.4 will go more into depth on the topic of power consumption by the PSJA arrays and how to possibly decrease power consumption in the future.

#### 6.1.1. First experiment.

Though the calibration of the angle of attack and the zero-run of the first experiment might have some small errors, some good qualitative phenomena can still be observed to see how actuation affects the lift and drag of the NACA 0015 model, as seen in figure 6.1. Looking at the lift curve of the baseline case one can see that lift linearly increases up to an angle of attack around  $\alpha \approx 13.25^\circ$ , after which the lift drops. As it takes about  $2^\circ$  for the lift to reach a minimum it likely experiences trailing edge stall, where separation slowly creeps from the trailing edge upstream to the leading edge of the airfoil,[13]. From  $\alpha \approx 15.25^\circ$  lift starts to increase once more, but when decreasing the angle from a post-stall position a hysteresis effect is visible as it joins the lift curve at  $\alpha \approx 12.25^\circ$ , showing that the hysteresis spans  $\Delta\alpha_{hys} = 1^\circ$ .

Where stall occurs in the baseline case, the actuated cases still experience increase in lift for increasing angles of attack. Depending on the actuation frequency, the maximum lift is obtained between  $\alpha \approx 15^\circ - 16^\circ$  and in the case of  $F^* = 1$  the increase in lift with respect to the baseline case is  $\Delta C_L = 10\%$ , however at higher dimensionless discharge frequencies this benefit becomes less, as for  $F^* = 6$  the difference in lift is reduced to  $\Delta C_L = 2\%$ . Another benefit of PSJ actuation is the omission of the hysteresis.

Looking at the drag polar of the baseline case a quadratically increasing trend up to  $\alpha \approx 13.25^\circ$  can be seen. This quadratic increase is due to the induced drag component which varies quadratically with respect to the lift coefficient. However, from  $\alpha = 12.25^\circ - 14.25^\circ$  drag shoots up as the wing experiences an increasing amount of separated flow. When the flow is fully separated,  $\alpha = 14.25^\circ$  lift gradually increases again albeit with a lesser slope than pre-stall.

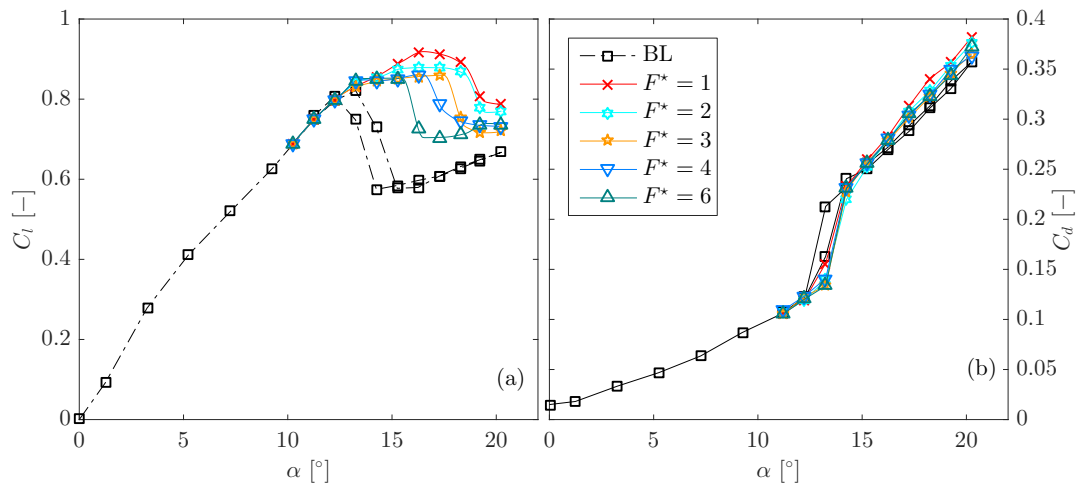


Figure 6.1: Lift and drag polar at  $U_\infty = 10 \text{ m/s}$  and  $Re = 1.65 \cdot 10^5$ . BL is the baseline case without actuation.

A similar trend is seen when actuation is turned on, but the point at which drag shoots up is slightly delayed when the discharge frequency is adequate. At  $F^* = 1$ , this is not the case, but at actuation frequencies of  $F^* \geq 2$  partial separation is delayed by  $\Delta\alpha_s = 1^\circ$ . This can be deduced by the fact that the drag of the baseline and  $F^* = 1$  cases rises during two measurement steps suggesting that at first only partial separation is present, which then transition to leading edge separation. This effect is not seen at higher actuation frequencies where partial separation could be delayed as drag remains low. Though partial separation has been delayed drag shoots up directly after and unites with the baseline and  $F^* = 1$  case, suggesting that leading edge separation could not be combated by actuation.

### 6.1.2. Second experiment.

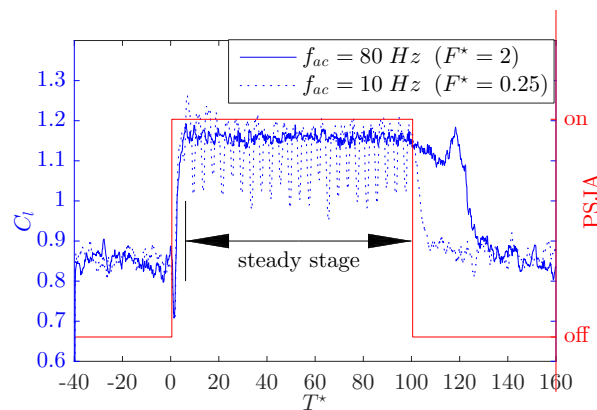


Figure 6.2: Dynamic response of the lift force to non-dimensional discharge frequencies of  $F^* = 0.25$  and  $F^* = 1$ , at  $\alpha = 15.5^\circ$  during a square wave test. The on or off indicate whether actuation is turned on or not.

Before the force balance curves were measured square wave tests were performed in order to see the time scales required for the effect of PSJ actuation to show up. During these tests PSJ actuation is periodically turned on or off for  $2.5 \text{ s}$  and the signal is then ensemble averaged. As can be seen from figure 6.2 it takes about 6 dimensionless time units for the forces to become steady. Comparing the augmented lift with the baseline lift one can see that actuation considerably improves the aerodynamic characteristics of the NACA 0015 model. It was observed that at dimensionless discharge frequencies of  $F^* \geq 0.5$  turning off the actuators did not result in a direct decrease in lift, but experienced the high lift status for approximately 20 time units before returning to the baseline lift. This transient process takes about 30 dimensionless time units. These time scales have also been observed by Benard et al.[3], where the transient process was put to use by creating a real-time feedback control system that operates

DBD actuators in low duty cycle as this can cut down the power consumption of these devices.

During the second experiment force balance data have been obtained for a multitude of free stream velocities. Starting with the lift polar of the baseline case at  $U_\infty = 10 \text{ m/s}$  and  $Re = 1.65 \cdot 10^5$ , see figure 6.3, one can see how the polar crosses the origin showing that the NACA 0015 is indeed symmetric. Increasing the angle of attack shows a steady increase in the lift coefficient up to  $\alpha = 15^\circ$  at which a maximum lift coefficient of  $C_L = 1.081$  is obtained. However two kinks are present in the ‘linear’ part of the polar. These changes in slopes, occurring at  $\alpha = 2^\circ$  and  $6^\circ$  respectively, likely indicate a presence of a laminar separation bubble. Though no further data has been collected to support this claim extensive research has been performed by Deepakkumar Sharma [45] showing that NACA 0015 airfoils do suffer from laminar separation bubbles at a certain range of Reynolds number. Increasing the angle of attack past  $\alpha = 15^\circ$  causes a sudden drop in lift indicating flow separation, however lift quickly starts to increase once more. Decreasing the angle of attack from a post-stall position shows the hysteresis effect experienced by the NACA 0015 as flow reattaches itself only at  $\alpha \leq 14^\circ$ . Comparing the stall and reattachment angle of attack with the previous experiment a discrepancy is seen. This mismatch is likely the result of a calibration error that occurred during the first experiment as the electric noise caused by the actuators caused the measurement system of the balance to ‘freeze’, requiring a reboot of the system. This caused a mismatch between the zero lift angle of attack and is propagated for all measurement angles. In case of the second experiment the measurement system has been moved further away from the actuators and shielded better such that no reboots were required during the force measurements resulting in a more realistic stall angle.

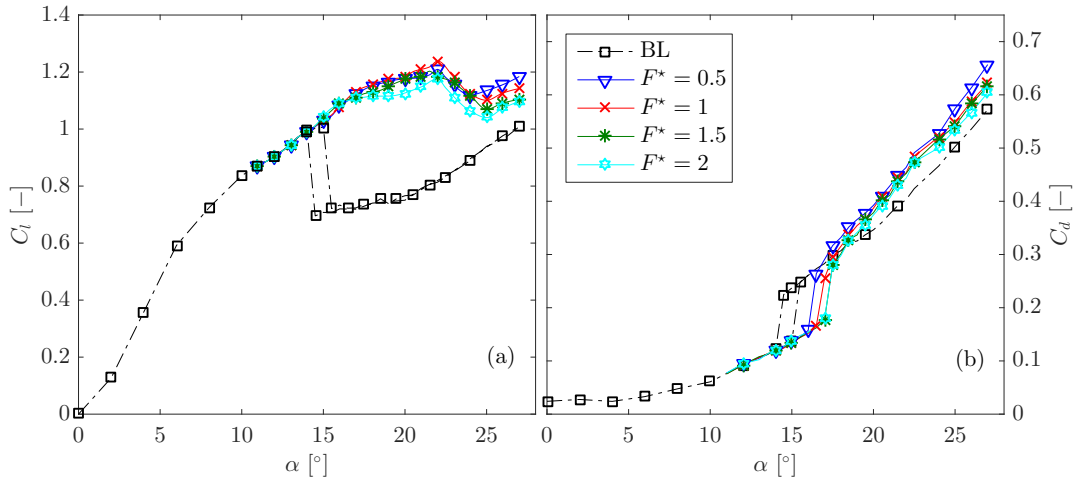


Figure 6.3: Lift and drag polar at  $U_\infty = 10 \text{ m/s}$  and  $Re = 1.65 \cdot 10^5$ .  
BL represents the baseline case without actuation.

Comparing the baseline case with the actuated cases one can see how actuation helps increasing the lift past the separation point experienced by the baseline case. Rather than stalling at  $\alpha = 15.5^\circ$  lift continues to grow monotonically up to  $\alpha \approx 22^\circ$ , where new maximum lift coefficients are obtained. Increasing the angle of attack further causes the lift to drop, but starts increasing again past  $\alpha \geq 25^\circ$ . Furthermore, the actuated cases show no signs of hysteresis as was experienced by the baseline case. It was found that modulating the flow at  $F^* = 1$  obtains the highest increase in lift with  $\Delta C_L \approx 20\%$  with respect to the baseline case. However, all actuation frequencies have a positive effect on the lift characteristics of the airfoil.

Moving on to the drag polar of the baseline case one can see that the drag coefficient is steadily growing up to the point of separation, which occurs at  $\alpha > 15^\circ$ . Separation causes the drag force to jump up before steadily growing again. Decreasing the angle of attack when separation has occurred shows a similar hysteresis effect as with the lift polar as it takes an angle of attack smaller than  $\alpha \leq 14^\circ$  for the drag to drop and reattach the flow.

The effect of actuation can only be spotted past the separation point of the baseline case as this sharp increase in drag is delayed for each of the actuated cases. It shows that increasing the actuation frequency allows for bigger delay in flow separation as the largest  $\Delta\alpha_s \approx 2^\circ$  is obtained at  $F^* = 1.5$  & 2. Contrary to the results of the first experiment even the lower frequencies are able to delay separation.

This difference can be explained by having a better distribution of the actuators as well as the slightly larger orifice as both will allow the actuators to affect a larger portion of the flow.

Increasing the free stream velocity of the wind tunnel to  $U_\infty > 10 \text{ m/s}$  (figures 6.4, 6.5 and 6.6) show similar patterns as at  $U_\infty = 10 \text{ m/s}$ . However, it was noticed that, in case of the baseline curves, the point of reattachment when decreasing the angle of attack from a post-stall condition increases with increasing Reynolds number. At  $U_\infty = 10 \text{ m/s}$  it takes about  $1^\circ$  for the force curves to join again, it takes about  $2.5^\circ$  at  $U_\infty = 15 \text{ m/s}$  and even  $4.5^\circ$  at  $U_\infty = 30 \text{ m/s}$ . Apart from the increasing hysteresis effect the lift coefficient also rises with free stream velocity, except at  $U_\infty = 30 \text{ m/s}$ . This is likely due to the fact that at these velocities moderate vibrations of the balance system have been recorded that could have caused a mismatch between the forces and the steady angle of attack.

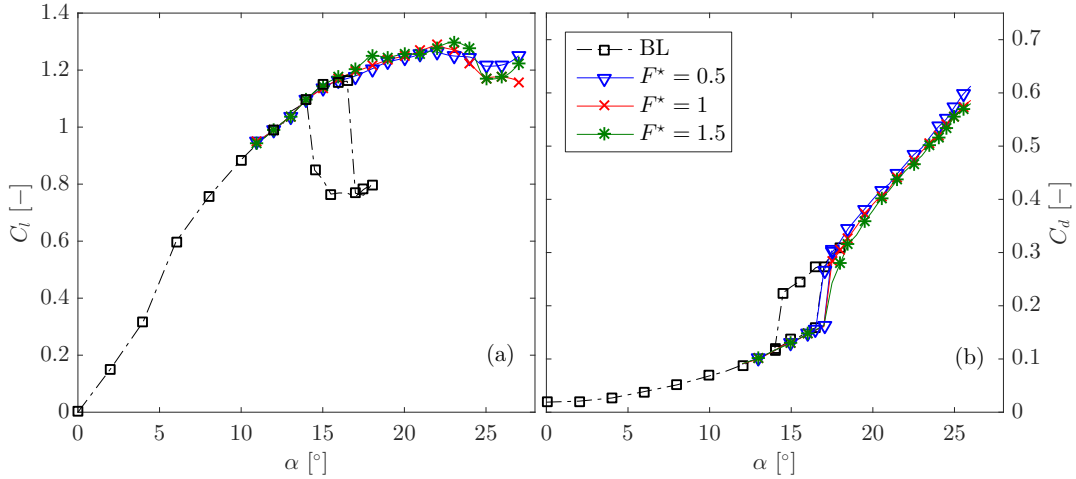


Figure 6.4: Lift and drag polar at  $U_\infty = 15 \text{ m/s}$  and  $Re = 2.48 \cdot 10^5$ .  
The remaining plotting methods are consistent with figure 6.3

Figure 6.4 shows the force balance curves at  $U_\infty = 15 \text{ m/s}$ . Comparing the lift polars with that of the lift polars at  $U_\infty = 10 \text{ m/s}$  a similar behaviour is found as in both cases actuation was able to elongate the monotonic growth of the lift polars up to  $\alpha \approx 22^\circ$ . However, contrary to a lower Reynolds number this time an actuation frequency of  $F^* = 1.5$  achieves the highest lift enhancement. Furthermore, the growth in maximum lift of the actuated cases is rather small when compared to the growth of maximum lift coefficient for the baseline cases at  $U_\infty = 10 \text{ m/s}$  and  $U_\infty = 15 \text{ m/s}$ .

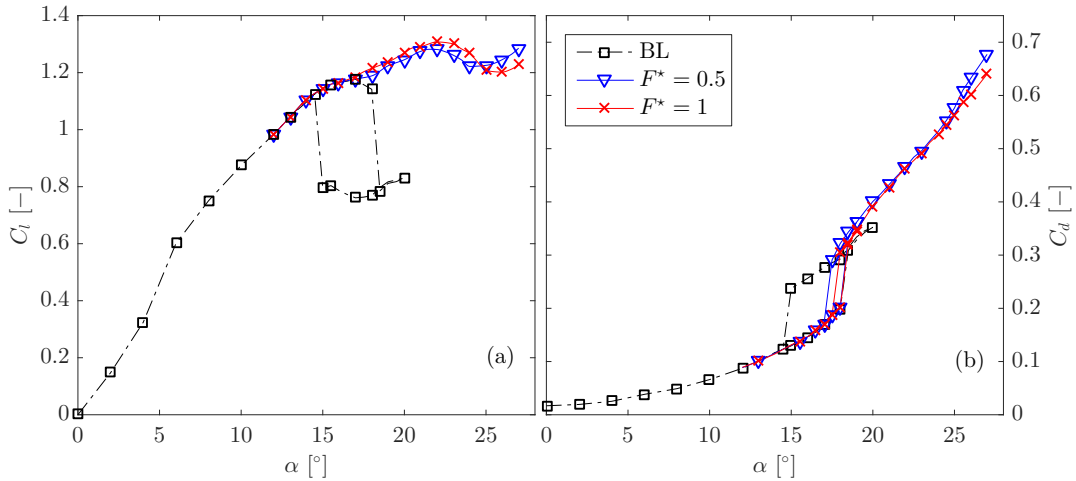


Figure 6.5: Lift and drag polar at  $U_\infty = 20 \text{ m/s}$  and  $Re = 3.31 \cdot 10^5$ .  
The remaining plotting methods are consistent with figure 6.3

Looking at the drag polar the amount by which separation can be delayed has also lessened and is the same for all actuation frequencies, though at  $F^* = 1.5$  a slightly lower drag is measured directly

post separation. Furthermore, a small hysteresis effect at  $F^* = 0.5$  is present as reattachment is delayed by  $0.5^\circ$ . This effect is not seen in the lift polar.

Increasing the free stream velocity to  $U_\infty = 20 \text{ m/s}$  (figure 6.5) does not alter the general shape of the lift polars of the actuated cases, but the drag polars are affected. Whereas actuation was able to delay separation at lower free stream velocities, it now is unable to do so. However, higher actuation frequencies do affect the drag polar by decreasing the hysteresis effect, with higher frequencies being able to decrease this effect more. Comparing the hysteresis effect of the baseline case with that of the actuated cases one can see that the effect can be pushed back from  $3.5^\circ$  to  $1^\circ$  and  $0.5^\circ$  for actuation frequencies of  $F^* = 0.5$  and  $F^* = 1$  respectively. This might be due to the fact that the jet velocities are lower than the local velocities close to the jet, which reduces their separation abilities as reported by Kim and Kim [29].

At  $U_\infty = 30 \text{ m/s}$  (figure 6.6) both lift and drag polars behave differently than the other cases. Whereas at lower Reynolds number actuation was able to extend the lift polar up to  $\alpha \approx 22^\circ$ , it now only limits the hysteresis effect of the lift polar. This is confirmed by looking at the drag polar as the hysteresis of the baseline case is reduced from  $4.5^\circ$  to  $2.5^\circ$  for both actuated cases.

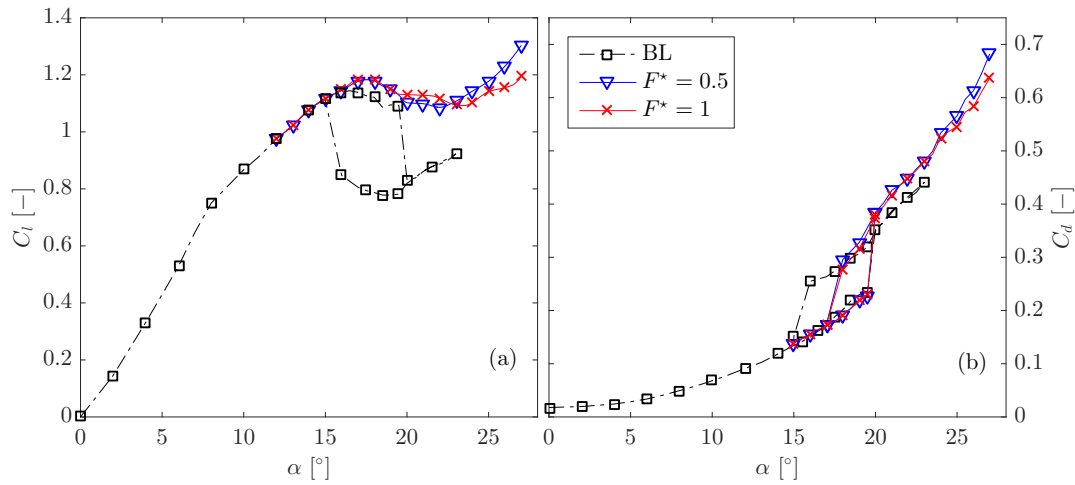


Figure 6.6: Lift and drag polar at  $U_\infty = 30 \text{ m/s}$  and  $Re = 4.96 \cdot 10^5$   
The remaining plotting methods are consistent with figure 6.3

### 6.1.3. The effect of PSJA density and placement.

As seen in the above two sections the lift and drag polars vary quite significantly when the amount of actuators are increased. Though no detailed comparison can be made due to the fact that the energy storing capacitance has been increased from  $C = 3 \text{ nF}$  to  $C = 4 \text{ nF}$  from the first to the second experiment and the fact that the actuator position in the first experiment is placed further downstream, some deductions can still be made. Increasing the actuator density leads to a better spreading allowing the increased number of jets to affect a larger portion of the flow, combining this with the enhanced momentum addition results in a better ability to combat flow separation as was seen from the drag polars. Whereas the first experiment was only able to delay partial separation by a single degree the second experiment was able to delay leading edge separation by  $\Delta\alpha_s = 2^\circ$ . As the separation point lies downstream of the actuator location for both cases this suggests that a better spreading results in a better ability to control the flow.

Another factor that plays a significant role is in the performance of the actuators. Since the actuation position of the second experiment is moved upstream it is able to remain upstream of the separation point for a larger span of angles of attack, resulting the actuated airfoil to experience ‘stall’ at higher angles effectively elongating the ‘linear’ part of the lift polar. Comparing the two experiments one can see that where the first experiment can only elongate the lift polar by  $\Delta\alpha = 4^\circ$  for dimensionless discharge frequencies of  $F^* = 1$ , this is increased to  $\Delta\alpha = 7^\circ$  when the actuators are placed upstream. It is therefore crucial to carefully design models with PSJ actuation as their performance vary drastically with changing actuator lay-out.

#### 6.1.4. Power consumption and the effect of duty cycle.

Knowing that the power to overcome the aerodynamic drag is defined as  $P = DU_\infty = C_D \frac{1}{2} \rho U_\infty^2 S U_\infty$  it is possible to compute the amount of power saved when actuation is turned on as:

$$\Delta P = \Delta C_D \frac{1}{2} \rho S U_\infty^3 \quad (6.1)$$

Knowing the discharge waveforms of a single actuation pulse it is also possible to compute in the input power as  $P_{in} = f_{ac} \int_0^{T_d} U_d(t) I_d(t) \cdot dt$ . A division of the two powers results in the power saving ratio defined as:

$$\eta = \frac{\Delta C_D \frac{1}{2} \rho S U_\infty^3}{f_{ac} \int_0^{T_d} U_d(t) I_d(t) \cdot dt} \quad (6.2)$$

At  $U_\infty = 10 \frac{m}{s}$  a maximum difference in drag of  $\Delta C_D \approx 0.1$  is found for  $F^* = 0.5$  resulting in a power saving ratio of  $\eta = 0.74$ , concluding that even for the case requiring the least amount of energy the savings do not outweigh the energy input, requiring further effort to raise the efficiency of the actuators for industrial applications. One likely reason why the energy input outweighs the energy output is that the jets are placed normal to the airfoil's surface, causing the jet to pierce the boundary layer (figure 6.7) depositing most of the energy in the free stream, rather than in the boundary layer itself. It is therefore likely that changing the geometry to e.g. tangential jets results in much higher power saving ratios as all discharge energy is deposited within the boundary layer as shown by Monir et al.[15].

Comparing the power saving ratio PSJAs with that of DBD actuators a similar ratio is found. According to Jukes and Choi [27] the fluidic power generated by the DBDs is taken as the denominator rather than the input power. This method of defining the power saving ratio results in very high ratios of  $\eta \sim 1500$  for cylinder flow control. Replacing the fluidic power with the energy input of the DBD actuators the energy saving ratio of DBDAs can be found. According to Giepmans and Kotsonis [17] the efficiency of SDBDAs is  $\mathcal{O}(0.1\%)$ , knowing that this efficiency is defined as the ratio of fluidic power outputted by the electric power consumed one can update the power saving definition by Jukes and Choi [27] by implementing the SDBDA efficiency, which results in power saving ratios of  $\eta \sim \mathcal{O}(1)$ . It can therefore be concluded that the power saving ratios for both PSJAs and DBDAs are similar in their ability to reduce separation at moderate Reynolds number flows.

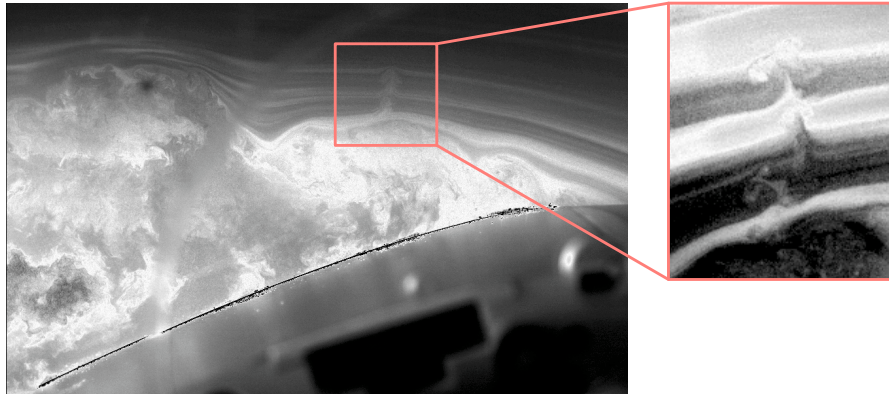


Figure 6.7: Jet piercing through the boundary layer.

However, during the square wave test it was found that, once flow was reattached, it maintained the high lift even as actuation was turned off. This asked the question whether it would be possible to decrease the duty cycle and still have the positive effects of the enhanced lift and delayed separation. The effect of the duty cycle on both lift and drag were performed at  $U_\infty = 10 \text{ m/s}$  and  $\alpha = 15.5^\circ$  and  $22^\circ$ . A constant period of  $T = 0.5\text{s}$  was used and the duty cycle denotes the fraction at which actuation occurs. The effect of duty cycle on a frequency of  $F^* = 1$  is shown in figure 6.8, where the performance,  $p$ , shows how well the array performs, with 0% being equally well as the baseline case and 100% being a fully actuated case. Looking at the effect of duty cycle on the lift performance one can see that at angles of attack at which flow reattachment is feasible,  $\alpha = 15.5^\circ$ , a non-linear trend in performance is noticed whilst at higher angles,  $\alpha = 22^\circ$ , a more linear trend is visible. This is likely

due to the fact that at moderate stall angles ( $\alpha \approx 15.5^\circ$ ) actuation was able to reattach the flow, whilst at  $\alpha = 22^\circ$  large-scale leading edge separation is never eliminated. This enables rapid fight-back of the separation area after actuation is withdrawn. The effect of duty cycle on the drag performance is similar, as indeed a non-linear trend is visible at low angles of attack, whilst at high angles of attack a nearly linear behaviour is seen.

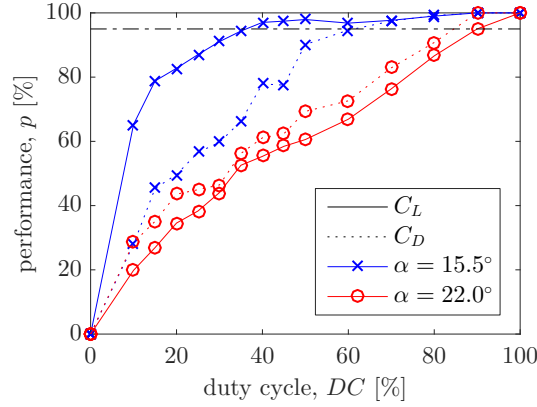


Figure 6.8: Effect of duty cycle on the aerodynamic performance of NACA 0015. Solid line represents the lift curves, whilst the dotted line represents the drag curves.

Seeing how duty cycle affects the performance of the aerodynamic properties of the airfoil it might be possible to reduce the power consumption of the actuation system at certain flight conditions. Though when flying at angles at which no reattachment is feasible it is still best to fly at a duty cycle of 100%. At angles at which reattachment is feasible power savings might be significant. In the case that an overall performance of  $p \geq 95\%$  is required, whilst flying at  $\alpha = 15.5^\circ - 17^\circ$  power savings of about 40% might be possible. If this translates to lower frequencies equally well the power saving ratio at  $F^* = 0.5$  could be  $\eta \sim 1.2$ , in which case the energy output does outweigh the energy input.

## 6.2. PIV results.

### 6.2.1. Time averaged velocity fields for the baseline cases.

Figure 6.9 shows the time averaged flow fields of a NACA 0015 airfoil at various angles of attack without actuation. Starting at  $\alpha = 13^\circ$  only a small part close to the trailing edge experiences separated flow as seen from the dividing streamline. Within this wake region, bounded by the dividing stream line, the flow in the near-wall region is moving upstream due to the experienced adverse pressure gradient. The interface between down and upstream moving flow is denoted by the zero-velocity line at which  $u = 0$ . Increasing the angle of attack results in an upstream movement of the separation point, resulting in a larger wake region as well as separation region. This gradual upstream movement of the separation location lasts until  $\alpha \approx 15.5^\circ$  where the localised separation point ‘shoots’ towards the vicinity of the leading edge. Due to the large separation region occurring at stall the lift drops significantly, whilst drag increases rapidly as seen from the lift and drag polars in figure 6.3. Increasing the angle of attack past this point of stall results in a slightly larger separation region and a small upstream movement of the separation point as seen for  $\alpha = 22^\circ$ . This behaviour of separation creeping upstream from the trailing edge towards the leading edge shows that a NACA 0015 airfoil, for the Reynolds numbers tested, indeed experiences the phenomenon called trailing edge stall[13].

For the PIV measurements two angles of interest are selected, being directly post stall,  $\alpha = 15.5^\circ$  in the case of a free stream velocity of  $U_\infty = 10 \text{ m/s}$ , and the angle of attack at which maximum lift occurs,  $\alpha = 22^\circ$ . The former to see the effect of flow reattachment as was deduced from the force measurements and the latter to see the changing dynamics when maximum lift is achieved. At these angles a wide range of actuation frequencies,  $0.1 \leq F^* \leq 2$  have been recorded in order to see how a varying actuation frequency affects the flow. In the case of the increased tunnel velocity (section 6.2.4) only the optimum frequency of  $F^* = 1$  is tested for the cases directly post stall and at the maximum lift angle of attack, this in order to compare how the free stream velocity affects the behaviour of PSJ actuation for these cases.

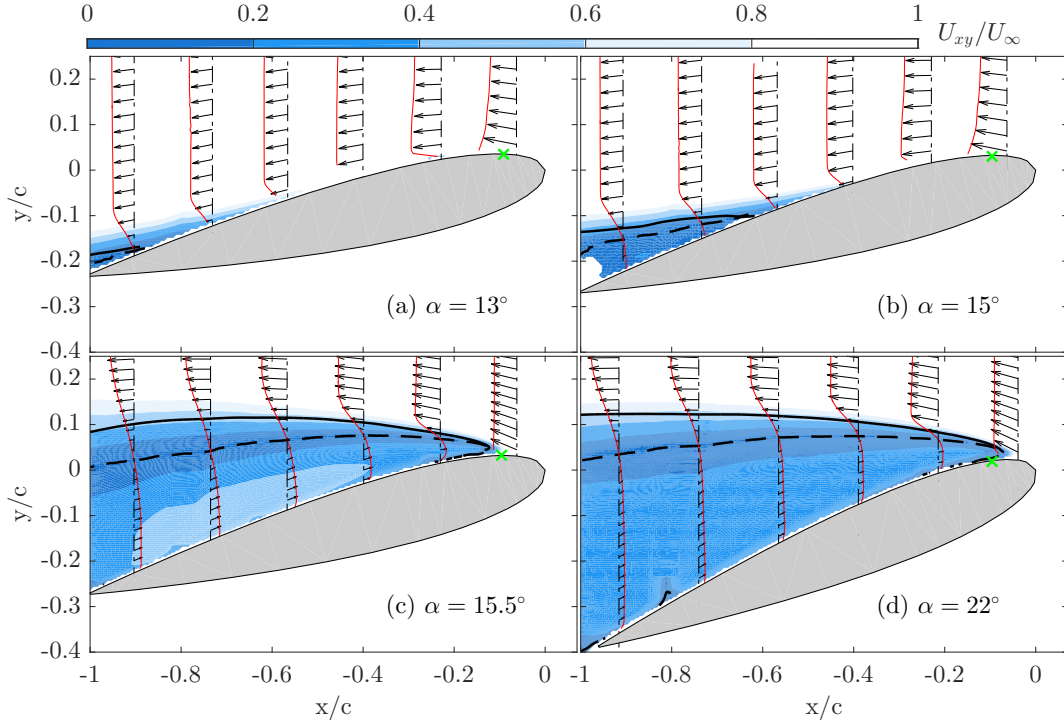


Figure 6.9: Time averaged velocity fields without actuation and for various angles of attack. The Euclidean sum of the velocity components (denoted as  $\sqrt{u^2 + v^2} = U_{xy}$ ) are shown as contours. Furthermore, the velocity profiles at various locations are shown. The solid black line represents the dividing streamline and the dashed black line denotes the location at which the condition  $u = 0$ , henceforth denoted as the zero-velocity line, is reached. The location of the actuators is denoted by the green x.

### 6.2.2. Leading edge separation control at $\alpha = 15.5^\circ$ (upstream actuation).

Looking at figure 6.10 the time averaged velocity profiles at  $\alpha = 15.5^\circ$  for various actuation frequencies within the range of  $0.25 \leq F^* \leq 2$  are shown. Comparing these flow fields with the baseline cases shown in figure 6.9 it is clear that each of the actuation frequencies significantly decrease the separation area,  $A_s$ , which is defined as the area enclosed within the zero-velocity line, the trailing edge and the airfoil surface. One can see that at frequencies of  $F^* \leq 0.25$  (figure 6.10 (a)) the separation point is hardly affected by the actuation, but the zero-velocity line remains closer to the suction side of the airfoil, effectively resulting in a smaller wake region. For larger actuation frequencies,  $F^* \geq 0.5$  (figure 6.10 (b)-(d)), the once separated flow has been reattached resulting in localised trailing edge separation in a similar fashion as seen pre-stall (figures 6.9 (a)-(b)) This reattachment results in fuller velocity profiles, especially close to the leading edge of the airfoil.

In order to compare the separation area and separation length cross-cases, non-dimensional versions of these quantities are used. The dimensionless separation area,  $A_s^*$ , and separation length,  $L_s^*$ , are defined in equation 6.3.

$$\begin{cases} A_s^* = \frac{A_s}{\frac{1}{2}c^2 \cdot \cos(\alpha) \sin(\alpha)} \\ L_s^* = 1 - \frac{x_s}{c \cdot \cos(\alpha)} \end{cases} \quad (6.3)$$

Where  $x_s$  is  $x$ -coordinate of the separation point with respect to the leading edge and  $c \cdot \cos(\alpha)$  is the length of the length of the airfoil at a specific angle of attack. The separation area,  $A_s$ , is non-dimensionalised by the triangular area formed by the chord and its projection within the  $x$  &  $y$ -axis, being  $\frac{1}{2} \cdot c \cos(\alpha) \cdot c \sin(\alpha) \rightarrow \frac{1}{2}c^2 \cdot \cos(\alpha) \sin(\alpha)$ . Figure 6.11 (a) shows the effect of actuation frequency on these parameters as well as the lift coefficient. Starting with the separation length one can see that at low frequencies,  $F^* \leq 0.25$ , actuation only marginally pushes back the point of separation, but after a certain frequency has been reached,  $F^* = 0.5$ , separated flow reattaches itself resulting in localised trailing edge separation, thus effectively delaying the point of separation, which can be seen in the

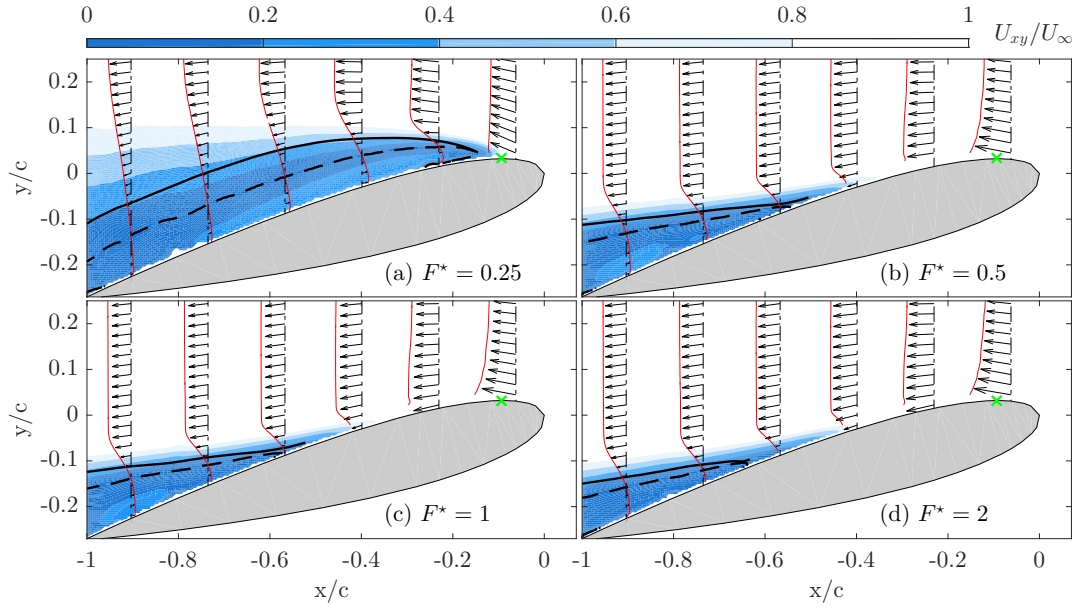


Figure 6.10: Time averaged velocity fields with actuation at  $\alpha = 15.5^\circ$ . The remaining plotting methods are consistent with figure 6.9.

sudden drop in separation length. Once reattachment has been established an increase in actuation frequency only slightly reduces the separation length.

How actuation frequency affects the separation area is different as there is a steep linear decrease in separation area at frequencies below  $F^* \leq 0.5$ . Even low actuation frequencies allow for a reduction in separation area. Increasing the frequency past the point of reattachment  $F^* \geq 0.5$  the separation area keeps decreasing albeit at a much slower rate. The lift coefficient reacts in a similar fashion as an increase in actuation frequency drastically increases the lift of the model, however this growth of lift force with respect to the actuation frequency declines at higher frequencies suggesting that there is a limit at which a further increase in frequency does not enhance the flow any further. This behaviour of the effect of frequency on leading edge stall agrees with the paper from Seifert et al. [42], which mentions that leading edge separation control requires reduced frequencies of  $F^* \geq 0.5$ .

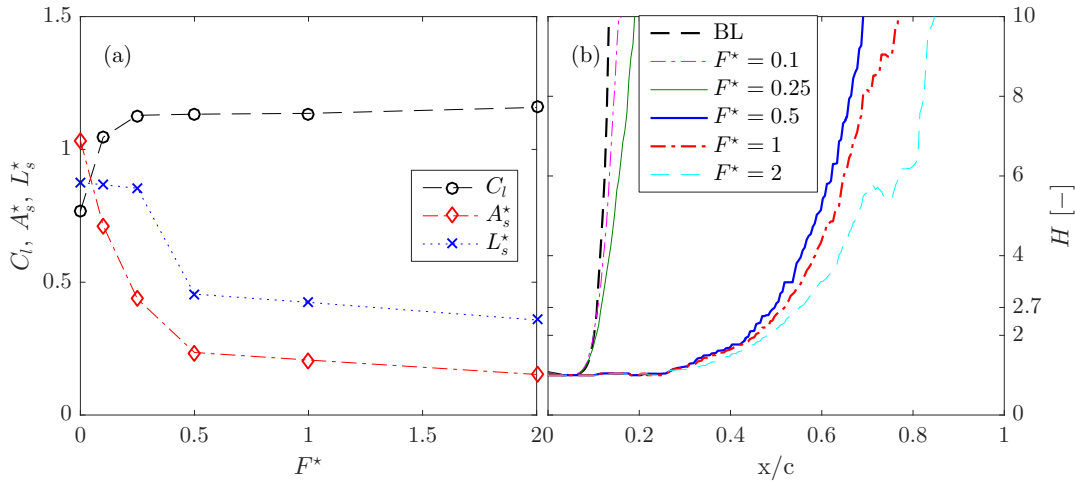


Figure 6.11: (a) Effect of actuation frequency on lift coefficient, separation area and separation length at  $\alpha = 15.5^\circ$ . (b) Varying shape factor throughout the chord for various actuation frequencies at  $\alpha = 15.5^\circ$ .

As flow separation is closely related to the velocity profiles of the boundary layer another method to quantify the effectiveness of PSJ actuation is the computation of the shape factor, which is defined as the ratio of the displacement thickness and the momentum thickness as  $H = \frac{\delta^*}{\theta}$ . These equations

for the displacement and momentum thickness, assuming incompressible flow, are shown below[41].

$$\begin{cases} \delta^* &= \int_{y_0}^{y_{ref}} \left(1 - \frac{u}{U_\infty}\right) dy \\ \theta &= \int_{y_0}^{y_{ref}} \frac{u}{U_\infty} \cdot \left(1 - \frac{u}{U_\infty}\right) dy \end{cases} \quad (6.4)$$

In the above equations the integration starts from the airfoil surface,  $y_0$ , up to a theoretical infinity, which in this case is the  $y$ -location at which the peak of the  $u$ -velocity component is reached,  $y_{ref}$ . The chord wise variations of the shape factor for each frequency is shown in figure 6.11 (b). According to Simpson[46] the shape factor corresponding to the point at which turbulent separation occurs is  $H = 2.70$ . Comparing separation locations found from figure 6.11 (b) with those from figure 6.10 a close resemblance is found. Though the exact transition points of the baseline and the actuated cases at  $F^* \leq 0.25$  are not able to be determined accurately since the resolution of the image is too low, it can be seen that for each case the shape factor grows with increasing chord, and that all actuated cases show a delay in separation with respect to the baseline case.

From both figure 6.10 and figure 6.11 (b) it can be seen that actuation causes the velocity profiles to be fuller. However, the mechanism behind the fuller velocity profiles, which can either be attributed to early transition to turbulent flow caused by the disturbances of the jet or due to the creation of counter rotating chordwise vortices created by the jets[61], cannot be determined. Though both mechanisms allow for more mixing between the free stream and the viscous wall region resulting in fuller profiles, more research needs to be performed in order to determine the true working mechanism, but perhaps it is a mix of both.

Figures 6.12 and 6.13 show the Reynolds normal stresses, or the RMS of the velocity fluctuations, of the  $u$  and  $v$  velocity components respectively. High RMS values of the velocity fluctuations show the unsteadiness of the flow and are often seen in separation regions and shear layers as these locations often experience the highest velocity fluctuations. One can see that in both figures the locus of the maximum Reynolds normal stress of the baseline case seems to be located on the dividing streamlines, which makes sense as the dividing streamline is often located within the shear layer. When actuation is turned on the locus of the maximum RMS do not exactly match as the dividing streamline is located just below the maximum. It is also noticed that at actuation frequencies that are unable to reattach flow,  $F^* \leq 0.25$  the Reynolds normal stresses increase, which is likely due to a fluttering motion of the shear layer caused by actuation. On the other hand, at frequencies at which reattachment is established these stresses are significantly reduced suggesting that an equilibrium in the flow field is reached once reattachment occurs. In this case the only location with significant velocity fluctuations is just downstream of the actuation location. This trend is also seen in figure 6.14 (a), where the maximum velocity fluctuation of the  $v$  velocity component throughout the chord is shown. Notice how for all cases a 'local' maximum around the actuation location is present, even for the baseline case. This peak reduces with actuation frequency, suggesting that higher frequencies are able to create an equilibrium in the flow field once reattachment has been established. At these higher frequencies the location at which the highest velocity fluctuations occur downstream of the actuation location, but more research needs to be performed to find out why this location experiences the highest velocity fluctuations.

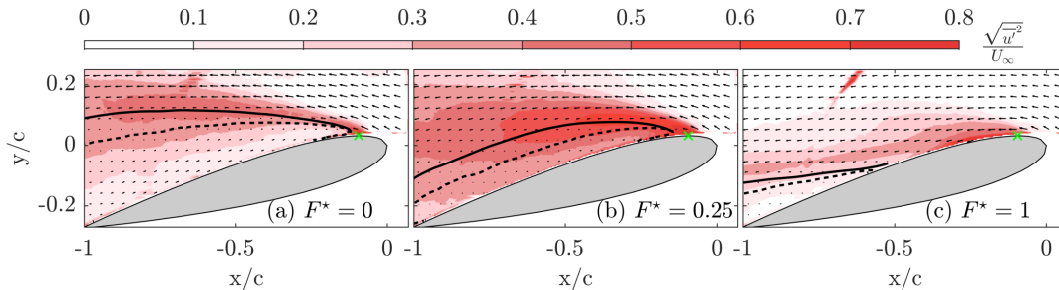


Figure 6.12: Reynolds normal stress of the  $u$  velocity component,  $\frac{\sqrt{u'^2}}{U_\infty}$ , for various actuation frequencies at  $\alpha = 15.5^\circ$ .

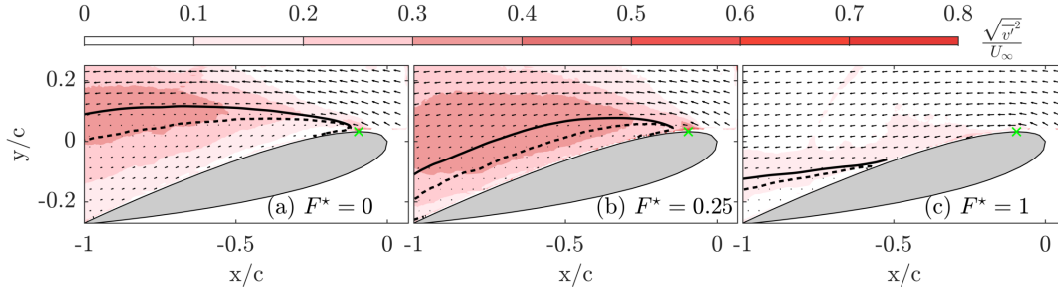


Figure 6.13: Reynolds normal stress of the  $v$  velocity component,  $\frac{\sqrt{v'^2}}{U_\infty}$ , for various actuation frequencies at  $\alpha = 15.5^\circ$ .

Figure 6.14 (b) shows the effect of actuation frequency on the velocity fluctuations in the frequency domain. A virtual probe has been placed on the dividing streamline at  $x/c = 0.7$ , measuring the velocity fluctuations of the  $v$  component to sense the fluttering motion of the shear layer with respect to the actuation frequency. Three different cases have been recorded being the baseline case,  $F^* = 0.25$  (actuation frequencies at which reattachment is not feasible) and  $F^* = 1$  (actuation frequencies at which actuation is feasible). Looking at the frequency domain of the baseline case one can see that there are several prominent peaks between  $0.25 \leq f^* \leq 1$  at which the velocity fluctuations are between 5%-10% of the free stream velocity  $U_\infty$ . When actuation is applied there are three prominent peaks located at  $f^* = 0.125, 0.25$  and  $0.5$ , suggesting that the fluttering motion of the separated shear layer is indeed positively affected by the actuation of the PSJAs. When frequency is increased past the point of reattachment, one can see that all peaks are absent, suggesting that actuation at high frequencies is able to suppress the velocity fluctuations. At frequencies larger than  $f^* \geq 2.5$  no dominant frequencies are noticed.

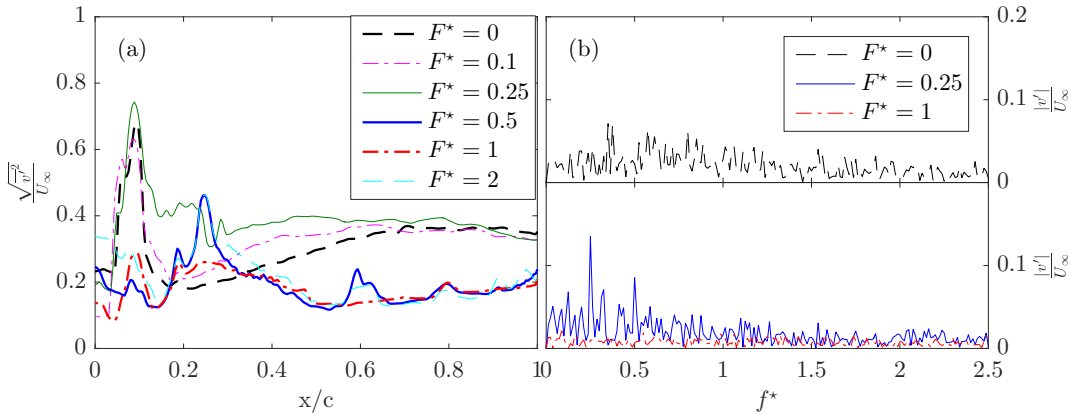


Figure 6.14: (a) Chordwise variation of the peak velocity fluctuation in  $y$ -direction,  $\overline{v'}$ , at  $\alpha = 15.5^\circ$  for varying frequencies. (b) Frequency spectra probed in the dividing streamline at  $x/c = 0.7$ .

Due to the fact that the camera signals together with the discharge signals have been recorded it was possible to find the phase averaged velocity fields, which are used to see how the flow fields vary throughout an actuation cycle. Figure 6.15 (a) shows how the separation area varies over time and in figure 6.15 (b) the dynamic lift response at  $F^* = 0.25$  and  $\alpha = 15.5^\circ$  together with the separation area is shown for a single actuation cycle. For frequencies at which reattachment is feasible,  $F^* \geq 0.5$ , separation area is nearly constant throughout a single phase. At lower frequencies,  $F^* \leq 0.25$ , the separation area is heavily dependent on the phase of the actuation cycle, which is consistent to the frequency and velocity fluctuation plots figures 6.12-6.13. One can see that at these frequencies it takes about  $0.5 \leq T^* \leq 1$  for the separation area to drop after actuation has occurred and in the case of  $F^* = 0.1$  a plateau has been reached for  $T^* \gtrsim 6$ , meaning that it takes about 6 non-dimensional time units for the disturbance to propagate away. This time scale will be referred to as the separation reset time,  $T_r$ , hence forth.

In order to reveal the underlying mechanisms that cause PSJA to affect the flow, several time

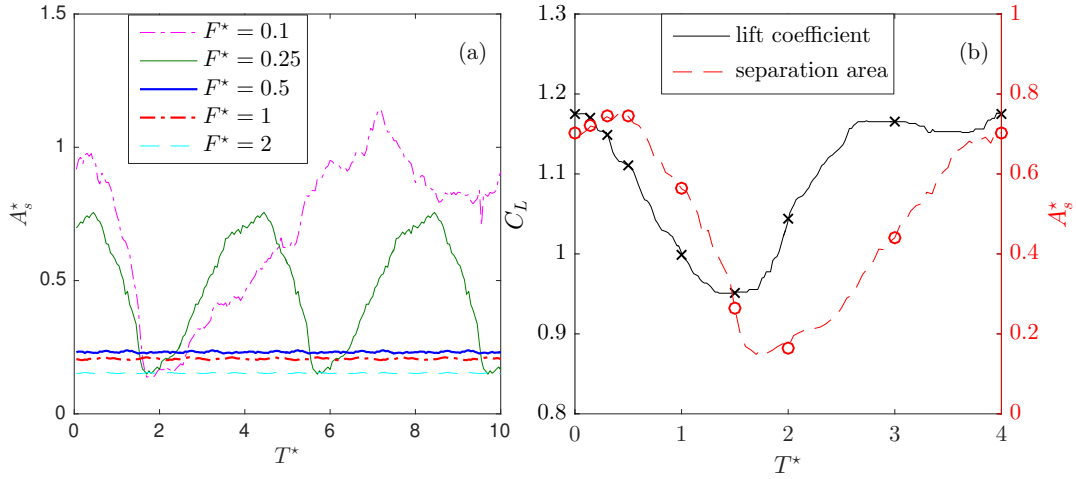


Figure 6.15: (a) Phased averaged separation area at  $\alpha = 15.5^\circ$ . (b) Comparison between the phase averaged separation area and dynamic lift coefficient at  $\alpha = 15.5^\circ$  and  $F^* = 0.25$ . The markings show the instances shown in figure 6.15

instances within a cycle, operating at  $F^* = 0.25$ , have been shown in figure 6.16, where the time instances correspond to the marking from figure 6.15 (b). The vorticity  $\omega_z$  is normalised with the ratio of the airfoil thickness over the free stream velocity,  $t_c/U_\infty$ .

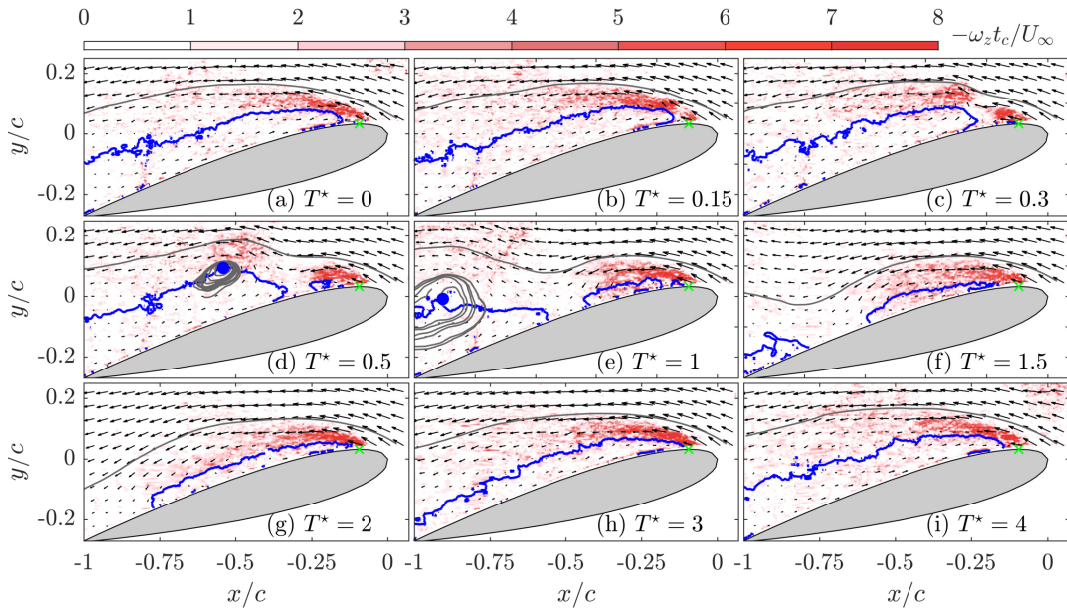


Figure 6.16: Phase averaged velocity fields at  $F^* = 0.25$  and  $\alpha = 15.5^\circ$ . The in plane velocity is represented by black arrows and dimensionless vorticity is shown by the red contours. The borders of the separation area,  $u = 0$ , are shown by the blue lines, whereas the thin grey lines represent streamlines. Vortex locations are marked by blue dots.

Before any disturbances are caused by actuation one can see in figure 6.16 (a) that vorticity is continuously shed from a point close to the leading edge, which is convected downstream along the zero-velocity line. After a single pulse,  $T^* = 0.15$ , the vortex shedding is temporarily halted effectively cutting the vortex sheet in two as the jet pierces through the boundary layer,  $T^* = 0.3$ . The downstream vortex is then rolled up into a concentrated vortex and is slowly convected downstream, whilst pushing point of separation downstream, reducing the separation region ( $T^* = 0.3$  &  $0.5$ ). The upstream vortex on the other hand slowly moves downstream, but remains close to the airfoil surface, creating a small separation bubble that increases in size as the upstream vortex sheet propagates downstream ( $0.5 \leq T^* \leq 2$ ). Once the downstream vortex is out of sight and the separation bubble has reached the trailing edge the separation area increases even more by pushing the vortex sheet away from the

suction surface,  $2 \leq T^* \leq 4$ , up to the point of the undisturbed flow experienced at  $T^* = 0$ .

With the help of the phase averaged flow fields from figure 6.16 an explanation for the rise in lift with increasing separation region, as seen in figure 6.15 (b), can be given. As this is likely due to the fact that the separation bubble creates a virtual hump causing the effective airfoil shape to change. Due to the change in shape the NACA 0015 loses its symmetrical properties and creates a chamber that enhances the lift characteristics of the airfoil as observed by Mittal and Rumpunggnoon[34]. This increasing lift occurs up to the point that the bubble bursts when reaching the trailing edge as the airfoil now experiences fully separated flow once more.

### 6.2.3. Leading edge separation control at $\alpha = 22^\circ$ (downstream actuation).

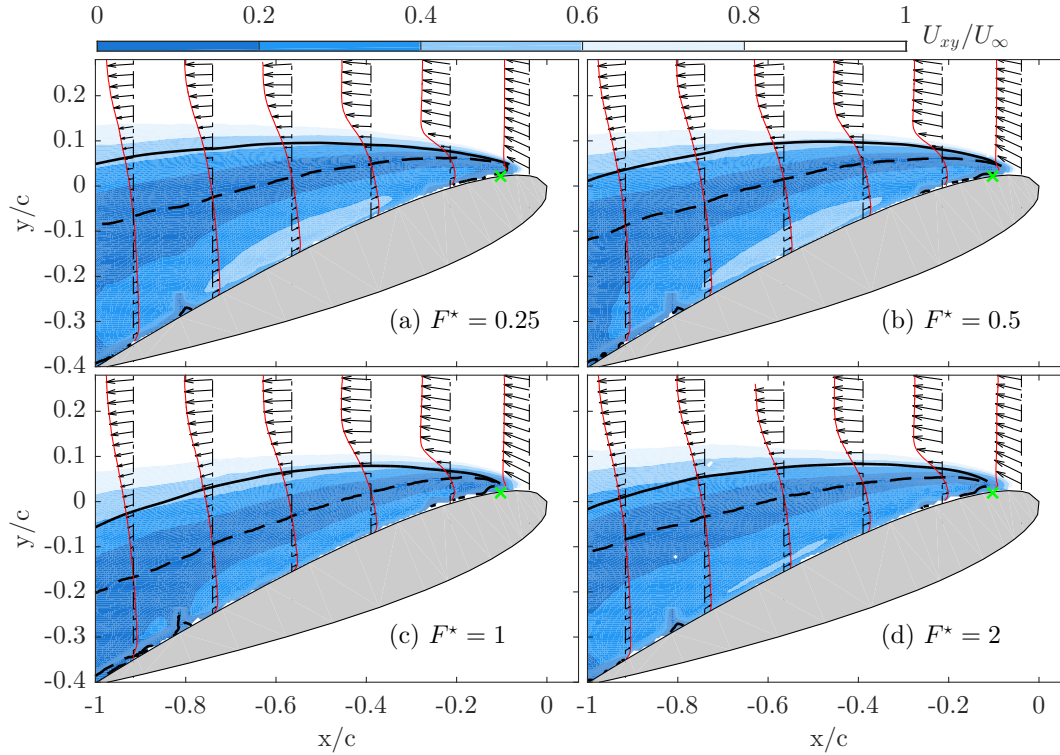


Figure 6.17: Time averaged velocity fields with actuation at  $\alpha = 22^\circ$ . The remaining plotting methods are consistent with figure 6.9.

Figure 6.17 shows the time averaged velocity fields at  $\alpha = 22^\circ$  for increasing frequencies. As can be seen from these fields is that the separation point has been moved upstream from the actuation location. Comparing this to the flow fields at  $\alpha = 15.5^\circ$ , at which the separation point is downstream of the actuators, it can be deduced that downstream actuation is less effective than upstream actuation and is therefore unable to reattach flow. This difference becomes even clearer when comparing figure 6.18 (a) with figure 6.11 (a), where the trends observed for the normalised separation area and separation length are absent in the case of downstream actuation. The separation length hardly decreases with actuation frequency as it decreases from 0.925 to 0.89 from  $F^* = 0$  to  $F^* = 2$  respectively. Separation area is affected by the actuation frequency, but the linear behaviour is reduced to  $F^* = 0.25$  and a minimal separation area is found for  $F^* = 1$ , where at upstream actuation the minimum is found for the highest actuation frequency. This optimum is also found in the lift coefficient as it increases up to  $F^* = 1$ , but decreases again when increasing the frequency past this point. This corresponds to the findings from Seifert et al.[42], which state that the optimum actuation frequencies lie within a reduced frequency range of  $0.5 \leq F^* \leq 1$ .

Figure 6.18 (b) shows how the shape function varies throughout the chord close to the leading edge. Contrary to the shape functions at  $15.5^\circ$  all cases show a quickly growing shape function from  $x/c \geq 0.1$ , indicating that all cases are not able to delay the separation of the boundary layer as momentum within the boundary layer drops and are unable to effectively mix the high momentum free stream flow with

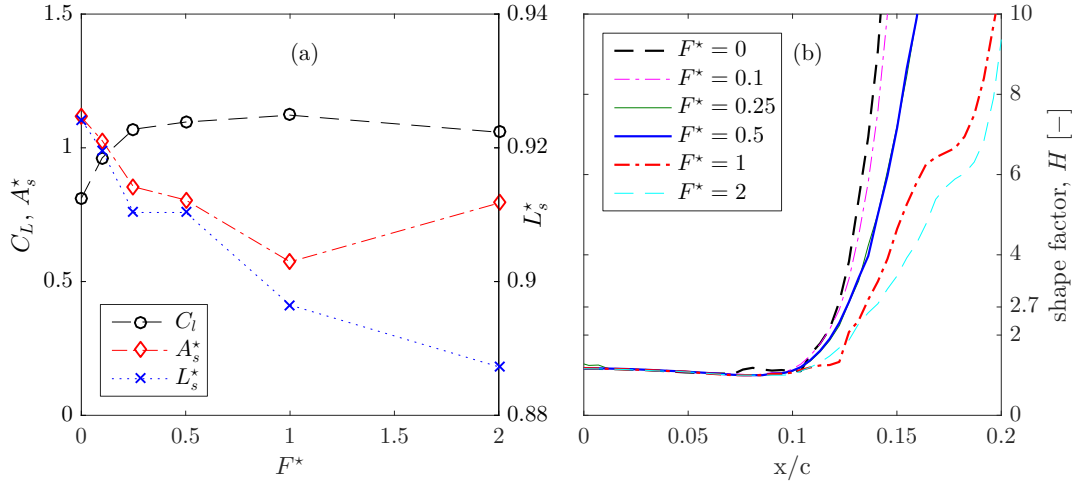


Figure 6.18: (a) Effect of actuation frequency on lift coefficient, separation area and separation length at  $\alpha = 22^\circ$ . (b) Varying shape factor throughout the chord for various actuation frequencies at  $\alpha = 22^\circ$ .

the low momentum boundary layer flow. Though the growth is affected by plasma actuation, frequency only has a marginal effect on the separation point, confirming the results from figure 6.18 (a).

The RMS of the velocity fluctuations  $\overline{u'}$  and  $\overline{v'}$  are shown in figures 6.19 and 6.20 respectively. Similar to the cases seen in figures 6.12 and 6.13 the cases at  $F^* = 0$  and 0.25 the velocity fluctuations slowly grow downstream, however at  $F^* = 1$  a different RMS field is visible. Whereas at  $\alpha = 15.5^\circ$  shows a reduced magnitude and area of the Reynolds normal stresses, at  $\alpha = 22^\circ$  the magnitude and area of the Reynolds normal stresses have grown to be even more than at  $F^* = 0.25$ , suggesting that, when the point of actuation is downstream of the separation point, higher frequencies are able to influence the shear layer and hence the separation layer more than lower frequencies.

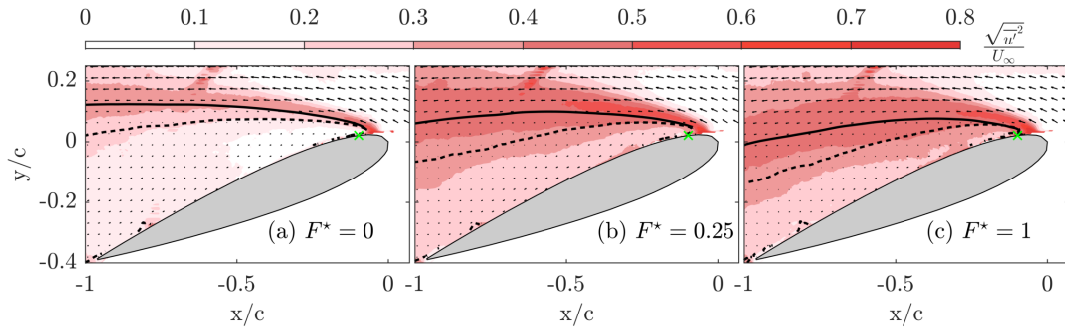


Figure 6.19: Reynolds normal stress of the  $u$  velocity component,  $\frac{\sqrt{u'^2}}{U_\infty}$ , for various actuation frequencies at  $\alpha = 22^\circ$ .

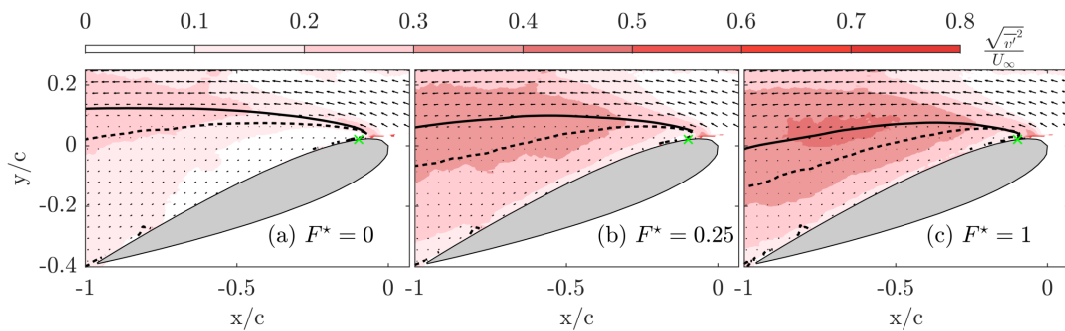


Figure 6.20: Reynolds normal stress of the  $v$  velocity component,  $\frac{\sqrt{v'^2}}{U_\infty}$ , for various actuation frequencies at  $\alpha = 22^\circ$ .

The chordwise evolution of the maximum  $\overline{v'}$  at  $\alpha = 22^\circ$  is shown in figure 6.21 (a). Contrary to the  $\alpha = 15.5^\circ$  (figure 6.11) case the most prominent peak for all frequencies is located in front of the actuation location and very close to the separation point. This peak is unaffected by the actuation frequency, suggesting that separation is mostly influenced by the geometry of the airfoil and its flow conditions. Downstream of the actuators actuation does slightly affect the maximum velocity fluctuations obtained, with higher frequencies resulting in larger fluctuations, however the maximum velocity fluctuations occur at  $F^* = 1$ . This corresponds to the findings of figure 6.18 as a minimum separation area is seen at  $F^* = 1$ . As higher velocity fluctuations indicate a more unstable shear layer caused by the effect of the jets suppressing the separation region.

Contrary to the maximum velocity fluctuations at  $\alpha = 15.5^\circ$ , where, in the case of  $F^* \leq 0.25$ , the maximum fluctuations increase with increasing frequency and then, at  $F^* \geq 0.5$ , are able to reattach the flow resulting in much lower velocity fluctuations indicate that for  $\alpha = 22^\circ$  not enough mixing is possible. This makes sense as the separation point is located upstream of the actuators, causing them to interact with backflow. Since this backflow region is quite thin and moves very slowly, due to the closeness of the airfoil surface, a jet with high exit velocity will pierce right trough this region depositing hardly any energy where it is needed, as most of the energy will end up in the free stream flow. With hardly any energy entering the separation region actuation is unable to effectively affect the upstream boundary layer. Together with a elevated adverse pressure gradient and the inability to affect the boundary layer all cases show leading edge separation.

Figure 6.21 (b) shows the frequency spectra for  $\alpha = 22^\circ$  at  $x/c = 0.7$ . The baseline condition at  $\alpha = 22^\circ$  shows reduced fluctuations compared to  $\alpha = 15.5^\circ$ . Where the maximum amplitudes at  $\alpha = 15.5^\circ$  nearly reached  $\overline{v'}/U_\infty = 0.1$ , the highest peaks at  $\alpha = 22^\circ$  are around  $\overline{v'}/U_\infty = 0.05$ . However the range at which the peaks occur is much wider,  $0.5 \leq F^* \leq 1.7$ , showing that at  $\alpha = 22^\circ$  there are more natural disturbances, which can be treated as receptive frequencies of the shear layer. Modulation within this receptive range,  $F^* = 1$ , shows only a single prominent peak at  $F^* = 1$ , whereas actuation outside of this receptive range,  $F^* = 0.25$  shows several higher order harmonics within the range of the natural disturbances.

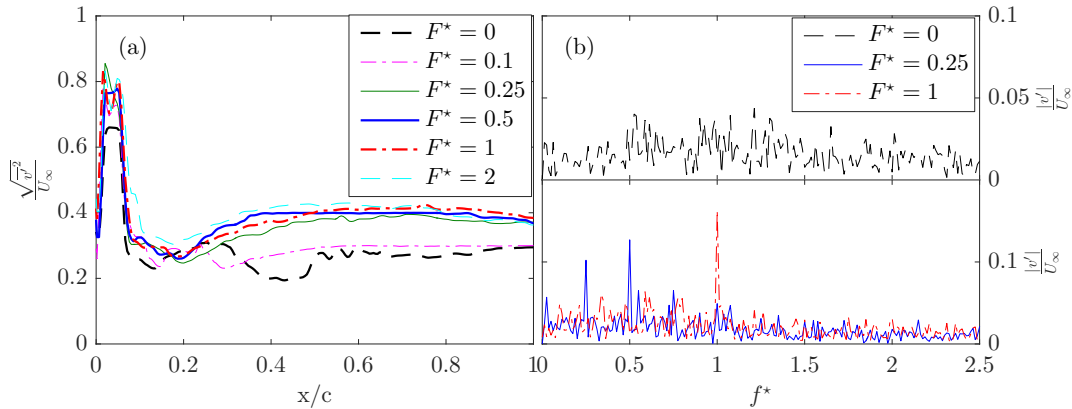


Figure 6.21: (a) Chordwise variation of the peak velocity fluctuation in  $y$ -direction,  $\overline{v'}$ , at  $\alpha = 15.5^\circ$  for varying frequencies. (b) Frequency spectra probed in the dividing streamline at  $x/c = 0.7$ .

The variation of the separation area at increasing frequency is shown in figure 6.22 (a). Comparing the variation of separation area at  $\alpha = 22^\circ$  with that at  $\alpha = 15.5^\circ$  (figure 6.15 (a)) one can see that actuation at  $F^* \leq 1$  is not able to achieve a stable separation area and is therefore constantly changing within an actuation cycle.  $F^* = 2$  does achieve a stable separation area albeit larger than  $F^* = 1$ . Looking at modulation at lower frequencies one can see that the time at which the minimum separation area occurs is moved forward to  $T^* \approx 1.3$ . Also the separation reset time,  $T_r$  has been decreased to about 3 time units. These latter effects can be due to the fact that the local velocity around the airfoil has increased due to the larger blockage at  $\alpha = 22^\circ$ , as the vortices are now convected by a faster flow around the airfoil. With this decrease in separation reset time the  $F^* = 0.1$  and  $0.25$  cases are now very similar as the corresponding cycle period, four time units, is large enough to reset the flow conditions,  $T_r \geq \frac{1}{F^*}$ , and cause two different pulses to be independent of each other. This means that within the range of  $F^* \leq \frac{1}{T_r}$  a frequency increase would result in a linear decrease of the average separation area

and therefore a higher lift coefficient, which is seen in figure 6.18 (a). When  $F^* \geq \frac{1}{T_r}$  the two individual jets and its resulting vortices will inevitably interact with each other removing the linear dependence on separation area and lift.

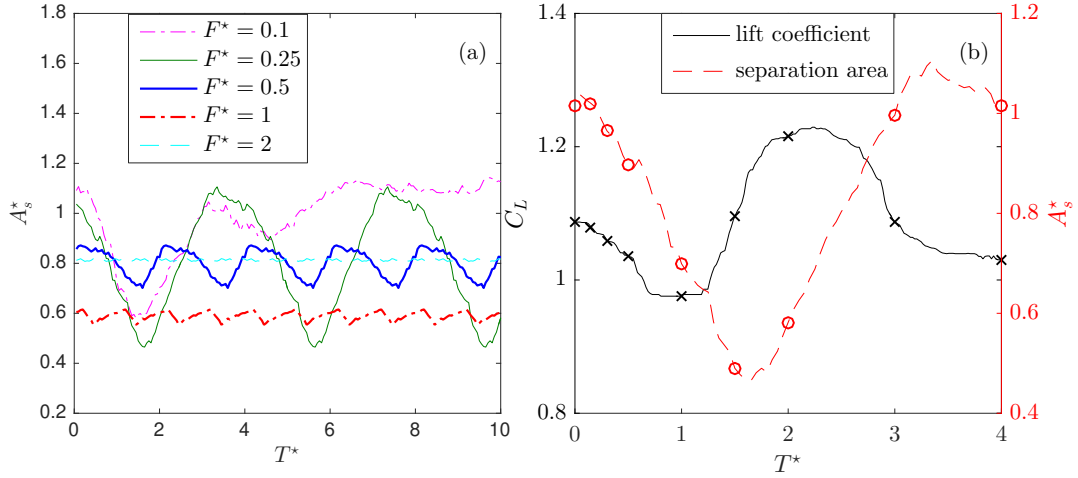


Figure 6.22: (a) Phased averaged separation area at  $\alpha = 22^\circ$ . (b) Comparison between the phase averaged separation area and dynamic lift coefficient at  $\alpha = 22^\circ$  and  $F^* = 0.25$ . The markings show the instances shown in figure 6.23

The phase averaged flow fields at  $F^* = 0.25$  is shown in figure 6.23 and figure 6.22 (b) shows the current separation area and lift coefficient as a reference to the flow fields. The overall response to plasma synthetic jet actuation  $F^* = 0.25$  and  $\alpha = 22^\circ$  is similar to actuation at  $\alpha = 15.5^\circ$ . At  $T^* = 0.2$  the vortex sheet is cut in two by the pulsed jet, which then rolls up into a concentrated vortex for  $0.5 \leq T^* \leq 2$ . However the two separation regions remain in each others vicinity, which was not the case for  $\alpha = 15.5^\circ$  where the two separation regions drift away from each other. This renders the new

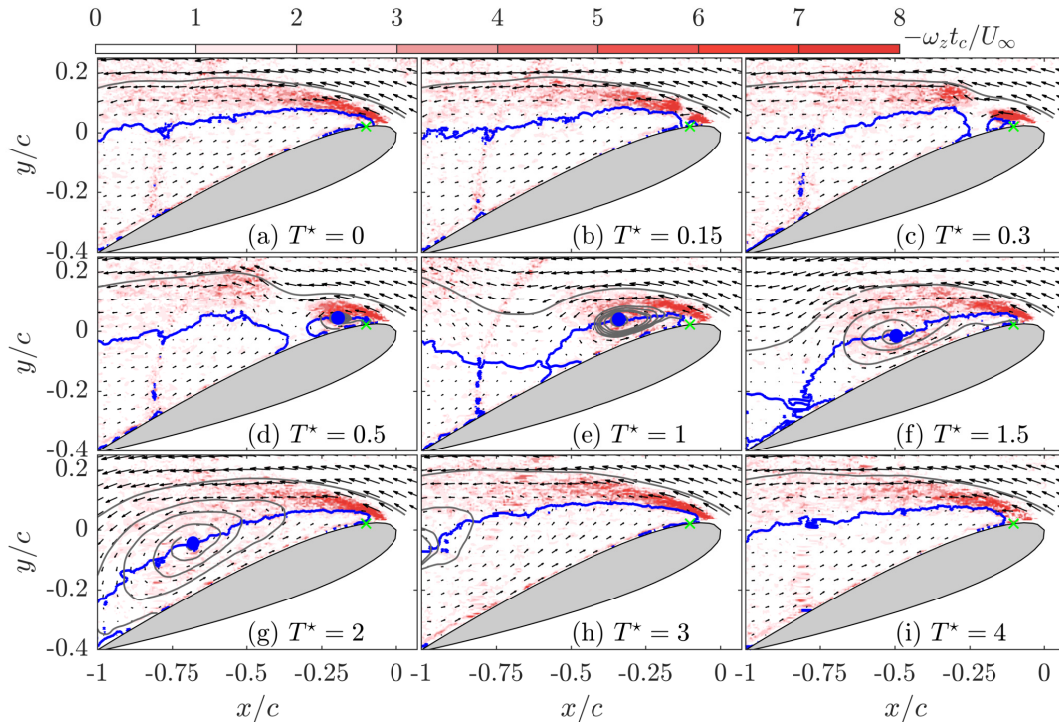


Figure 6.23: Phase averaged velocity fields at  $F^* = 0.25$  and  $\alpha = 22^\circ$ . The plotting methods are copied from figure 6.16

separation bubble unable to positively affect the virtual airfoil shape. This illustrates that the mixing of the free stream flow with that of the near-wall region is unable to withstand the large adverse pressure

gradient as the vortex is located too far away from the suction side to provide good mixing of high and low momentum flow. However, the separation area is reduced by moving the zero-velocity line closer to the suction surface of the airfoil as the vortex propagates downstream. From  $T^* > 2$  the zero velocity line moves away from the airfoil surface causing the separation area to grow again.

Looking at how the lift coefficient changes with separation area (figure 6.22 (b)) one can see that indeed lift grows significantly between  $1 \leq T^* \leq 2$ , where the new vortex suppresses the separation area as it is convected downstream. This large vortex causes the flow to locally accelerate resulting in a lower dynamic pressure, which results in the high lift experienced. This phenomenon is also observed in the case of dynamic stall and pitching airfoils where a stall vortex is shed from the leading edge once the pitching angle exceeds the static stall angle. This allows the lift to temporarily be higher than than the static peak for the time it takes for the vortex to be convected downstream[9]. Little et al.[32] achieved the above mentioned control mechanism by using nanosecond SDBDA where the compression waves resulted in coherent vortices being periodically shed. This result was to be expected as PSJAs, similarly to nanosecond SDBDA, are able to create significant compression waves[58].

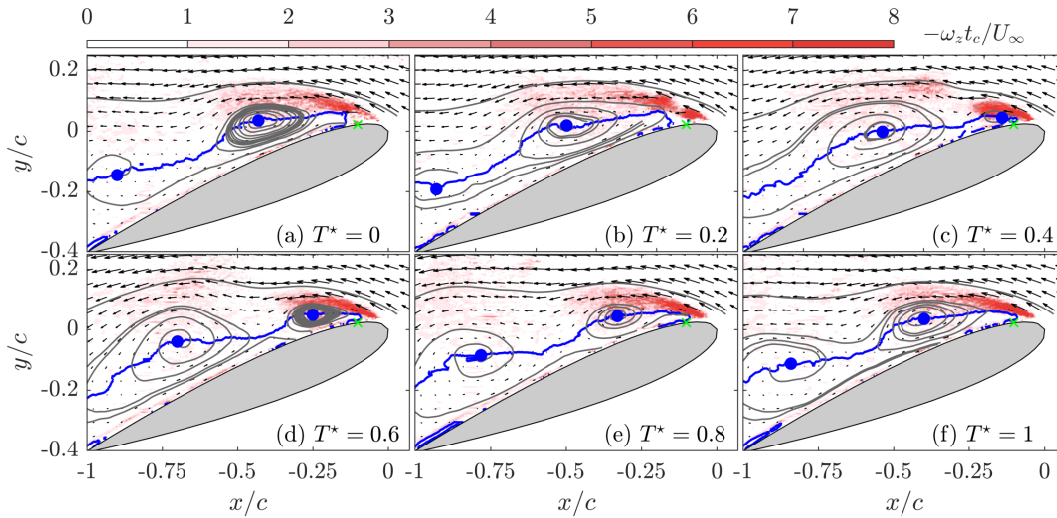


Figure 6.24: Phase averaged velocity fields at  $F^* = 1$  and  $\alpha = 22^\circ$ . The plotting methods are copied from figure 6.16

In order to see why a frequency of  $F^* = 2$  underperforms to  $F^* = 1$  the phase averaged flow fields for these two cases are shown in figures 6.24 and 6.25 respectively. From these figures it can be seen that at  $F^* = 1$  two vortices, approximately half a chord length apart, can be detected from the streamline patterns. As discussed earlier these vortices are created by ‘cutting’ the vortex sheet emanating from the leading edge by the pulsed jets. Once these sheets are cut they roll in onto themselves creating concentrated vortices as seen from these flow fields. The ability to push the zero-velocity lines towards the suction surface is greatly dependent by the size and strength of these vortices. For  $F^* = 1$  the distance between the vortices,  $0.5c$ , is large enough to reduce the interaction between individual vortices, allowing each vortex to grow and suppress the separation region.

When looking at  $F^* = 2$  there are three vortices, approximately  $0.3c$  apart. This causes significant interaction between the vortices inhibiting them to grow in size and strength. Since all vortices rotate counterclockwise the downwash effect of a new vortex can partially counteracted by upwash effect of the antecedent vortex while propagating downstream, resulting in a less efficient modulation of the separation area and hereby decreasing the lift coefficient for frequencies of  $F^* > 1$ .

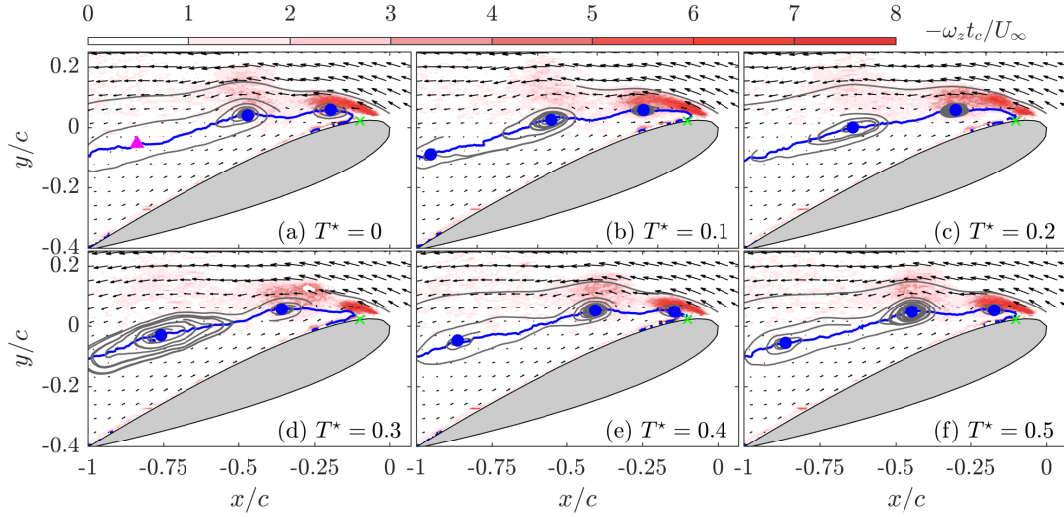


Figure 6.25: Phase averaged velocity fields at  $F^* = 2$  and  $\alpha = 22^\circ$ . The magenta triangle represents an estimated vortex based on other results, the remaining plotting methods are copied from figure 6.16

#### 6.2.4. Startup and quenching process of PSJ actuation.

In order to enhance understanding of PSJ actuation not only the steady stage, but also the startup and quenching process of PSJ actuation needs to be investigated such that the dynamic response of attached and separated flow is found. As mentioned, at  $\alpha = 15.5^\circ$  a transient process in which the lift remains enhanced when actuation is withdrawn is noticed as seen from figure 6.2.

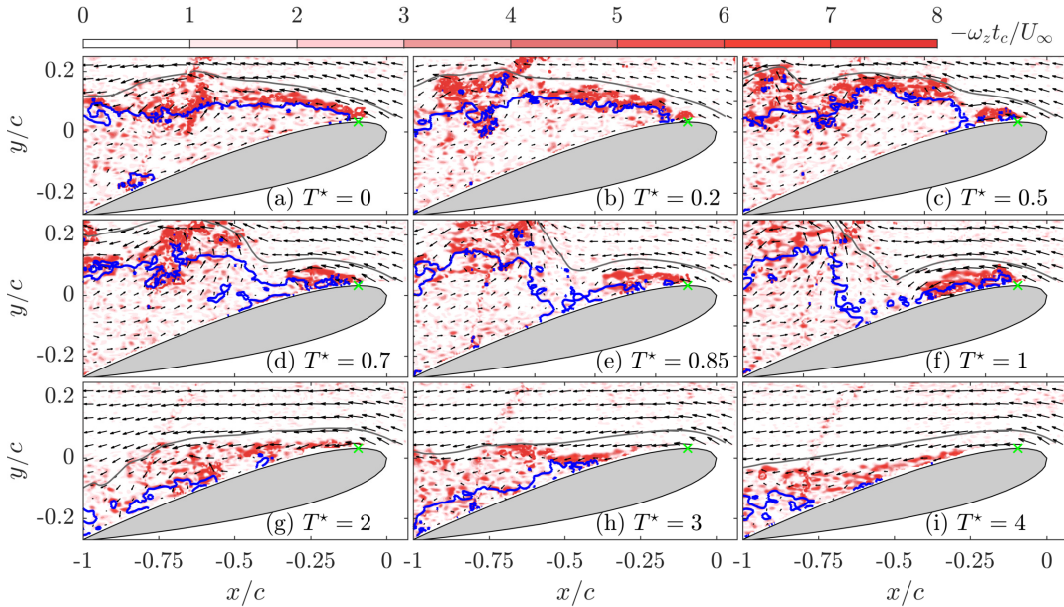


Figure 6.26: Instantaneous flow fields at  $F^* = 1$  and  $\alpha = 15.5^\circ$  during the startup phase of PSJ actuation. The plotting methods are copied from figure 6.16

Figure 6.26 shows the startup phase of actuation at  $F^* = 1$ . Before actuation,  $T^* = 0$ , a clear separated region is seen that emanates closely downstream from the actuation point. Once actuation is turned on the vortex sheet is cut in two causing the point of separation to move downstream ( $T^* = 0.2$ ). These two vortex sheet then drift away from each other resulting in two individual separation regions,  $T^* = 0.5$ , though these merge soon after,  $T^* = 0.7$ , before drifting apart again. As the vortex sheets drift apart the 'old' sheet rolls into itself resulting in a large concentrated vortex which is slowly convected downstream,  $T^* = 0.7 - 1$ . Meanwhile the 'new' vortex sheet remains close to the suction surface slowly

moving towards the trailing edge as the old separation region makes place for it to grow. At  $T^* = 1$  the flow has undergone a single actuation cycle and it can be seen that the old vortex sheet has moved to about half chord,  $x/c = 0.5$ . It takes about a second cycle,  $T^* = 2$ , for it to move outside the field of view all while the new sheet is slowly convected downstream. Once the old vortex sheet has moved away it takes about two more pulses for the separation region to be fully transitioned to localised trailing edge separation,  $T^* = 3 - 4$ .

A close up of the transient process that was noticed during the square wave test is shown in figure 6.27. The flow fields visualising this quenching process, where lift remains enhanced when actuation is withdrawn, are shown in figure 6.28, where  $T^* = 0$  is directly after the last electric pulse.

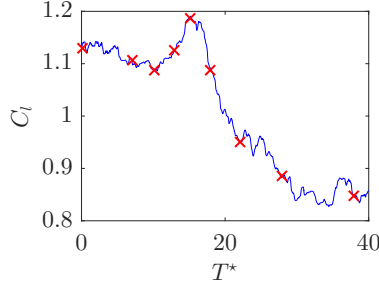


Figure 6.27: Quenching process for  $F^* = 1$  and  $\alpha = 15.5^\circ$ . The red markings correspond to the time instances from figure 6.28.

At  $T^* = 0$  the separation point is still located around  $x/c = 0.5$ , however as time passes the separation point creeps upstream until  $T^* \approx 10$ . During these stages the NACA 0015 airfoil still experiences localised trailing edge separation, but as the separation point moves upstream this region enlarges and negatively affects the lift as seen in figure 6.2. After the separation point has moved towards the leading edge the separation spans the entire chord, but it remains close to the suction surface of the airfoil, creating a separation bubble as also experienced by  $F^* = 0.25$  at  $\alpha = 15.5^\circ$  as seen in figure 6.16. As this bubble virtually affects the shape of the airfoil increasing its camber profile lift starts to increase again,  $T^* = 13 - 15$ , as was also observed by Mittal and Rumpungnoon[34]. However, as this local bubble bursts and the separation region increases in size the virtual shape is negatively affected resulting in the lift to drop,  $T^* = 18 - 28$ , as it transitions to the baseline case as seen in figure 6.9 (c),  $T^* = 38$ .

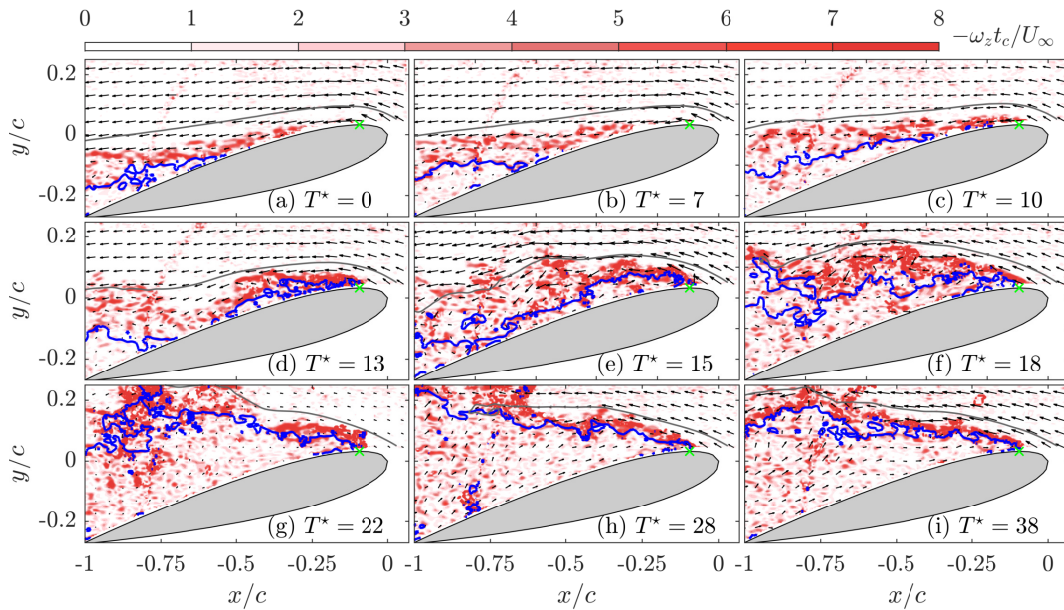


Figure 6.28: Instantaneous flow fields at  $F^* = 1$  and  $\alpha = 15.5^\circ$  during the cool down phase of PSJ actuation. The plotting methods are copied from figure 6.16

### 6.2.5. Increasing the free stream velocity.

As seen in section 6.1.2 free stream velocity negatively affects the ability of PSJ actuation to reestablish attached flow. Whereas at  $U_\infty = 10 \text{ m/s}$  PSJ actuation was able to delay separation by  $\Delta\alpha_s = 2^\circ$  and remove any hysteresis effect, see figure 6.3, at  $U_\infty = 20 \text{ m/s}$  the actuators are unable to delay separation and even experience a small hysteresis effect of  $\Delta\alpha_{hys} = 0.5^\circ$  for  $F^* = 1$  as seen in figure 6.5. Looking at the lift polars the maximum lift coefficient obtained remains very similar as both magnitude and angle of attack,  $\alpha_{C_{Lmax}}$ , hardly change when increasing the tunnel velocity. Thus, in order to see what the cause of this might be time averaged velocity fields are shown in figures 6.29 and 6.30, in which the velocity fields at  $F^* = 1$  are shown for both free stream velocities.

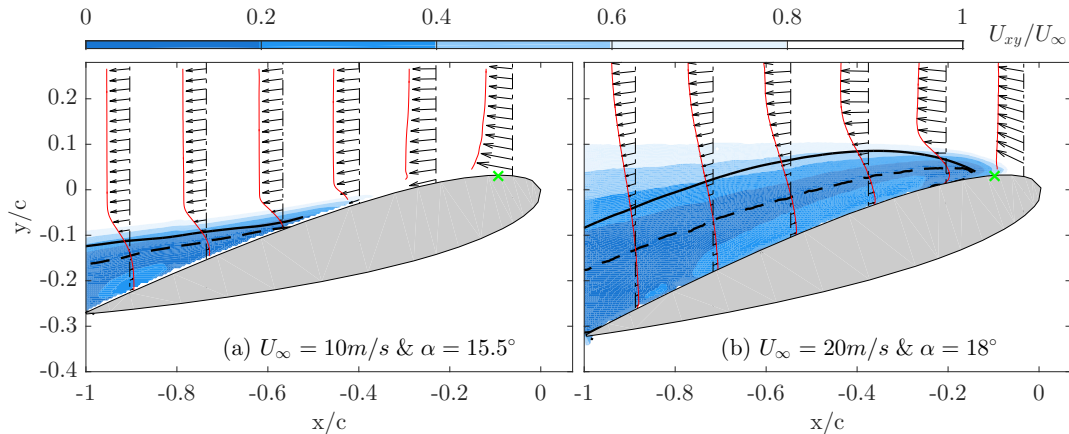


Figure 6.29: Time averaged velocity fields with actuation directly post stall at (a)  $\alpha = 15.5^\circ$  and  $U_\infty = 10 \text{ m/s}$  and (b)  $\alpha = 18^\circ$  and  $U_\infty = 20 \text{ m/s}$ . For both cases the non-dimensional frequency is  $F^* = 1$ . The remaining plotting methods are consistent with figure 6.9.

When comparing the flow fields directly post stall (figure 6.29) it becomes clear why the airfoil experiences hysteresis effects for  $U_\infty = 20 \text{ m/s}$  but not for  $U_\infty = 10 \text{ m/s}$  as at higher velocities plasma actuation is unable to effectively reattach flow. Whereas actuation at  $U_\infty = 10 \text{ m/s}$  yields in localised trailing edge separation, actuation at higher velocities is unable to push the separation region rearward in a similar fashion as seen in figure 6.10 (a), where actuation at  $F^* = 0.25$  is unable to push the separation region rearward. Comparing figures 6.10 (a) and 6.29 (b) show nearly identical dimensionless velocity magnitudes as well as the location of the zero-velocity line.

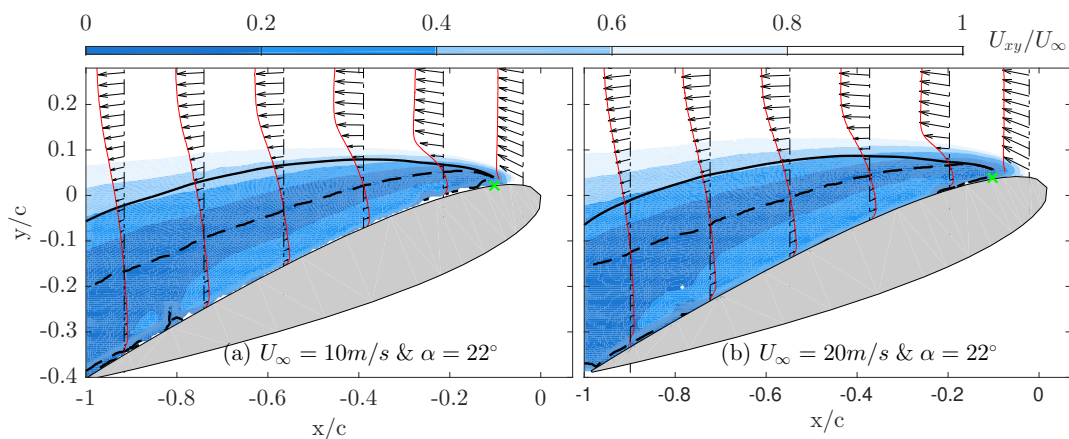


Figure 6.30: Time averaged velocity fields with actuation at  $\alpha_{C_{Lmax}}$  stall at (a)  $\alpha = 22^\circ$  and  $U_\infty = 10 \text{ m/s}$  and (b)  $\alpha = 22^\circ$  and  $U_\infty = 20 \text{ m/s}$ . The remaining plotting methods are consistent with figure 6.9.

Increasing the angle of attack to  $\alpha = 22^\circ$ , at which maximum lift is obtained for both  $U_\infty = 10 \text{ m/s}$  and  $20 \text{ m/s}$ , one can see that similar flow fields are obtained as the magnitude of both the non-dimensional velocities as well as the shape and size of the zero-velocity line are very similar. Both for

$U_\infty = 10 \text{ m/s}$  and  $20 \text{ m/s}$  the separation point has moved upstream of the actuators, which are unable to reattach the flow.

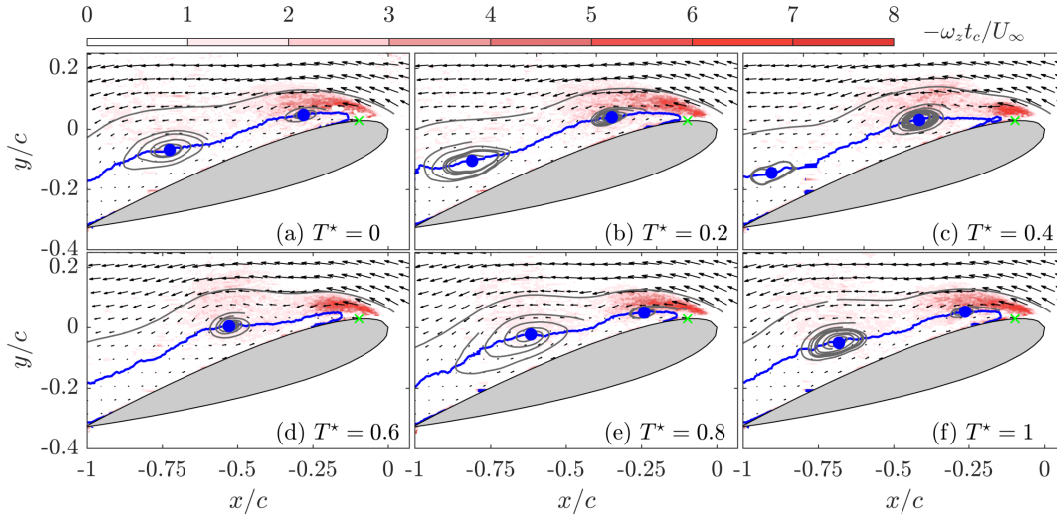


Figure 6.31: Phase averaged velocity fields at  $F^* = 1$  and  $\alpha = 18^\circ$ . The plotting methods are copied from figure 6.16

In order to see the mechanism behind the changed flow fields the phase averaged flow fields are shown in figures 6.31 and 6.32 for  $\alpha = 18^\circ$  and  $\alpha = 22^\circ$  respectively. Looking at the phase-locked flow fields at  $F^* = 1$  and  $\alpha = 18^\circ$  one can see that the jets are unable to ‘cut’ through the vortex sheet as was seen at  $U_\infty = 10 \text{ m/s}$ . Actuation is therefore unable to create two separation regions that drift apart from each other. Though at  $T^* = 0.4$  the vortex sheet is interrupted slightly creating a very small separation bubble directly downstream of the actuators, these two regions merge within the next time step. Because the separation cannot be separated into smaller ones it remains relatively large in size and is therefore unable to significantly increase the lift and drag characteristics as seen for upstream actuation at  $F^* = 1$  and  $U_\infty = 10 \text{ m/s}$ . This might be because of the low jet velocity achieved by the actuators rendering them unable to pierce through the boundary layer at high free stream velocities as the ratio of the peak jet velocity and the free stream is  $v_{jp}/U_\infty \approx 1.5$ , but due to the blockage the local velocity reached at the actuator location is higher resulting in a ratio of  $v_{jp}/u \approx 1$ . This phenomenon is also reported by Kim and Kim [29], where peak jet velocities of  $\frac{v_{jp}}{u} \mathcal{O}(1)$  were less useful when combating separation. This is likely due to the fact that synthetic jets with peak jet velocities similar to the free stream velocity do not supply sufficient jet momentum to disturb the separated flow at the trailing edge.

However, the reason why PSJ actuation still works is because of the same phenomenon discussed in section 6.2.3, where the concentrated vortices slightly push the zero-velocity line towards the airfoil surface. This mechanism is also the reason why actuation at  $\alpha = 22^\circ$  results in a higher lift. Though both frequencies have vortices approximately  $0.5c$  apart from each other resulting in negligible interference this larger distance from the wall allows for larger vortices, mixing the high and low momentum regions more effectively. Though the separation region has grown slightly from  $A_s^* = 0.705$  to  $A_s^* = 0.802$  this does not outweigh the increased pressure on the pressure side of the airfoil as the lift force grows between these two angles.

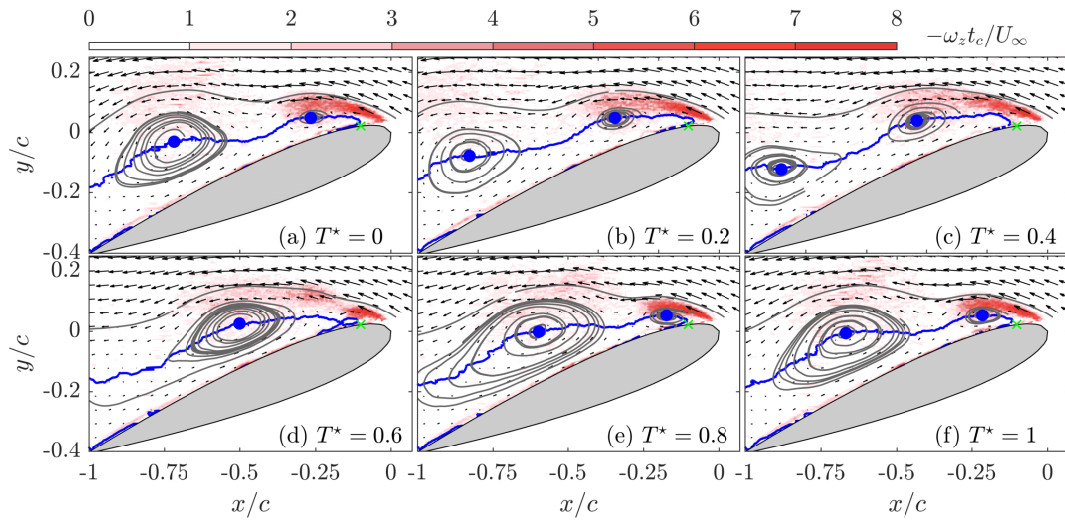


Figure 6.32: Phase averaged velocity fields at  $F^* = 1$  and  $\alpha = 22^\circ$ . The plotting methods are copied from figure 6.16

# 7

## Conclusion.

During the wind tunnel experiments the effects of PSJ actuation has been tested on two different NACA 0015 models, containing either 10 or 26 PSJ actuators. Both models, of which the actuator location was  $x/c = 0.12$  and  $x/c = 0.08$  for the first and second experiment respectively, were tested for the ability to control flow separation at moderate Reynolds numbers,  $Re = 1.65 \cdot 10^5$  &  $U_\infty = 10$  m/s. Balance measurements have been performed to find the overall airfoil performance and high-speed PIV cameras were used to capture the flow fields around the airfoil such that the underlying mechanisms responsible for the change in airfoil performance with actuators are found.

The range of dimensionless actuation frequencies were  $1 \leq F^* \leq 6$  and  $0.5 \leq F^* \leq 2$  for the first and second experiment respectively and in both cases were able to delay the stall angle of attack. During the second experiment the ‘linear’ part of the lift polar was extended from  $\alpha = 15^\circ$  to  $\alpha \approx 22^\circ$  accompanied by a maximum increase of lift of  $\Delta C_l = 0.232$  (23%) and a drag reduction, at  $\alpha = 15.5^\circ$ , of  $\Delta C_d = 0.1$  (40%). The first experiment showed a dependence on actuation frequency for the ability to extend the linear part of the lift polar, which was found to be between  $2^\circ - 3^\circ$ , resulting in a maximum lift improvement of  $\Delta C_l = 0.0945$  (11.5%) and a drag reduction, at  $\alpha = 13.25^\circ$ , of  $\Delta C_d = 0.0295$  (18%). Furthermore, the hysteresis loop experienced by the model without actuation, has been completely removed with the use of actuation. The power saving ratio at  $\alpha = 15^\circ$  and  $F^* = 0.5$ , which was similar as found for SDBDAs in cylinder flow control, was found to be insufficient for industrial applications as the energy input remains dominant over the energy output, however varying the duty cycle might be beneficial into decreasing the energy input to an extend where the energy output is dominant. Another factor that might prove more useful in the future is the implementation of tangential boundary layer PSJ actuation as suggested by Esmaeili Monir et al. [15], as the expelled momentum by the jets is solely deposited within the boundary layer, rather than in the free stream.

Increasing the free stream velocity has shows a similar picture as at  $U_\infty = 10$  m/s. Up to free stream velocities of  $U_\infty = 20$  m/s and Reynolds numbers of  $Re = 3.31 \cdot 10^5$  stall could be delayed to  $\alpha \approx 22^\circ$ . The ability to delay flow separation and remove hysteresis effects decreases with increasing Reynolds numbers and at  $U_\infty = 30$  m/s and  $Re = 4.96 \cdot 10^5$  actuation is no longer able to extend the lift polar.

The PIV measurements show that, at  $\alpha = 15.5^\circ$ , separation occurs closely downstream of the actuator position and when actuation is turned on at a sufficient frequency,  $F^* \geq 0.5$  large scale leading edge separation is converted to localised trailing edge separation, showing a similar flow field to the baseline case of  $\alpha = 15^\circ$ . The mechanism responsible for delaying separation is the energy mixing that has been provided by PSJ actuation, however the underlying mechanism responsible for this mixing, being either chordwise vortices created by the jets or the early transition to turbulent flow, still needs to be researched in more detail. When actuation occurs at lower frequencies,  $F^* \leq 0.25$ , leading edge separation cannot be converted to localised trailing edge separation, but these frequencies are still able to decrease the separation area and enhance the lift characteristics of the airfoil. At these frequencies, coherent spanwise vortices, which are generated by the interaction of the plasma induced pulsed jets and the separated shear layer emanating from the leading edge, result in a better mixing between the low momentum near-wall region and the high momentum free stream. The mixing caused by these spanwise vortices is responsible for the zero-velocity line to be pushed towards the suction surface of

the airfoil, which alters its virtual shape enhancing its lift characteristics.

Increasing the angle of attack to  $\alpha = 22^\circ$  results, when actuation is turned off, in the separation point to creep upstream of the actuator position. Though marginally moving the separation point downstream, frequencies of  $0.25 \leq F^* \leq 2$  are unable to convert this leading edge separation into localised trailing edge flow as seen at  $\alpha = 15.5^\circ$ . Increasing frequency initially allowed the separation to shrink but a minimum is found for  $F^* = 1$ , before increasing again, showing that, for lift characteristics, the optimum frequency is  $F^* = 1$ , as also observed from the balance measurements. The mechanism behind altering the flow characteristics at  $F^* \leq 1$  remains similar to the case of actuation at  $\alpha = 15.5^\circ$  and  $F^* \leq 0.25$  where the individual spanwise vortices generated allow for a better mixing of the high and low momentum regions. At  $F^* > 1$  this changes as the time between pulsed jets is too little resulting the spanwise vortices to be located too close to each other causing them to interact. This interaction takes form in counteracting their upwash/downwash not allowing them to grow to the appropriate size needed for thorough mixing, leading to a decline of the lift coefficient.

During the startup of PSJ actuation a similar process as seen in actuation at  $\alpha = 22^\circ$  and  $F^* \leq 1$  and  $\alpha = 15.5^\circ$  and  $F^* \leq 0.25$  is seen. A pulsed jet cuts the vortex sheet in two creating two individual separation regions that slowly drift apart. However, contrary to the cases reported in  $\alpha = 15.5^\circ$  and  $F^* \leq 0.25$  the newly created separation region is not allowed to grow to its full extent as a second pulse interacts with this separation bubble. As this process continues very small separation bubbles are created that are slowly convected downstream up to the point where leading edge separation is converted to localised trailing edge separation.

The cool down phase shows a reverse of the startup phase as flow initially rests in localised trailing edge separation. However, due to the absence of pulsed jets no more mixing between the high and low momentum regions is present which slowly causes the point of separation to move upstream. When the leading edge is reached a large bubble is formed temporarily increasing the virtual camber of the airfoil and enhancing its lift, before the bubble bursts and is restored to fully separated flow as seen in the baseline case of  $\alpha = 15.5^\circ$ .

# Bibliography

- [1] M. Amitay, M. Horvath, M. Michaux, and A. Glezer. Virtual aerodynamic shape modification at low angles of attack using synthetic jet actuators. *American Institute of Aeronautics and Astronautics*, 2001.
- [2] D.W. Bechert and W. Hage. Drag reduction with riblets in nature and engineering. *WIT Transactions on State of the Art in Science and Engineering*, 4, 2006.
- [3] N. Benard, L.N. Cattafesta, E. Moreau, J. Griffin, and J.P. Bonnet. On the benefits of hysteresis effects for closed-loop separation control using plasma actuation. *Physics of Fluids*, 23, 2011.
- [4] Y. Bouremel, J.M. Li, Z. Zhao, and M. Debiasi. Effects of ac dielectric barrier discharge plasma actuator location on flow separation and airfoil performance. *Procedia Engineering*, 67:270–278, 2013.
- [5] W.P. Breugem. Turbulence a. WB1424ATU, Q3-4 2016.
- [6] D. Caruana, F. Rogier, G. Dufour, and C. Gleyzes. The plasma synthetic jet actuator, physics, modeling and flow control application on separation. *AerospaceLab*, pages 1–13, 2013.
- [7] L.N. Cattafesta and M. Sheplak. Actuators for active flow control. *Annual Review of Fluid Mechanics*, 43:247–272, 2011.
- [8] E. Chatlynne, N. Rumigny, M. Amitay, and A. Glezer. Virtual aero-shaping of a clark-y airfoil using synthetic jet actuators. *American Institute of Aeronautics and Astronautics*, 2000.
- [9] T.C. Corke and F.O. Thomas. Dynamic stall in pitching airfoils: aerodynamic damping and compressibility effects. *Annual Review of Fluid Mechanics*, 47:470–505, 2015.
- [10] M.G. De Giorgi, C.G. De Luca, A. Ficarella, and F. Marra. Comparison between synthetic jets and continuous jets for active flow control: Application on a naca 0015 and a compressor stator cascade. *Aerospace Science and Technology*, 43:256–280, 2015.
- [11] M. DeSalvo, E. Whalen, and A. Glezer. High-lift enhancement using fluidic actuation. *American Institute of Aeronautics and Astronautics*, 2010.
- [12] G. Dimitriadis. Basic wind tunnel measurements and corrections. *Experimental Aerodynamics: Lecture 5*.
- [13] G. Eitelberg. *Experimental Simulations Reader*. 2018.
- [14] T.M. Emerick, M.Y. Ali, C.H. Foster, F.S. Alvi, and S.H. Popkin. Sparkjet characterisations in quiescent and supersonic flowfields. *Experimental Fluids*, 55, 2014.
- [15] H. Esmaili Monir, M. Tadjfar, and A. Bakhtian. Tangential synthetic jets for separation control. *Journal of Fluids and Structures*, 45:50–65, 2014.
- [16] L.H. Feng, K.S. Choi, and J.J. Wang. Flow control over an airfoil using virtual gurney flaps. *Journal of Fluid Mechanics*, 767:595–626, 2015.
- [17] R.H.M. Giepmans and M. Kotsonis. On the mechanical efficiency of dielectric barrier discharge plasma actuators. *Applied Physics Letters*, 98, 2011.
- [18] J.L. Gilarranz, L.W. Traub, and O.K. Rediniotis. A new class of synthetic jet actuators—part i: Design, fabrication and bench top characterization. *Journal of Fluids Engineering*, 127, 2005.

- [19] J.L. Gilarranz, L.W. Traub, and O.K. Rediniotis. A new class of synthetic jet actuators—part ii: Application to flow separation control. *Journal of Fluids Engineering*, 127:377–387, 2005.
- [20] D Greenblatt and I.J. Wygnanski. Control of flow separation by periodic excitation. *Progress in Aerospace Sciences*, 36(7), 2000.
- [21] B.R. Greene, N.T. Clemens, P. Magari, and D. Micka. Control of mean separation in shock boundary layer interaction using pulsed plasma jets. *Shock Waves*, 25:495–505, 2015.
- [22] J.W. Gregory, C.L Enloe, G.I. Font, and T.E. McLaughlin. Force production mechanisms of a dielectric-barrier discharge plasma actuator. *45th AIAA Aerospace Sciences Meeting and Exhibit*, 2007.
- [23] J.W. Gregory, J.C. Ruotolo, A.R. Byerley, and T.E. McLaughlin. Switching behavior of a plasma-fluidic actuator. *45th AIAA Aerospace Sciences Meeting and Exhibit*, 2007.
- [24] L. Henning. *Regelung abgelöster Scherschichten durch aktive Beeinflussung*. PhD thesis, Technischen Universität Berlin, 2008.
- [25] J. Jolibois, M. Forte, and E. Moreau. Application of an ac barrier discharge actuator to control airflow separation above a naca 0015 airfoil: Optimization of the actuation location along the chord. *Journal of Electrostatic*, 66:496–503, 2008.
- [26] S.N. Joshi and Y.S. Gajurathi. A review on active and passive flow control techniques. *International Journal on Recent Technologies in Mechanical and Electrical Engineering*, 3(4):1–6, 2016.
- [27] T.N. Jukes and K.S. Choi. Long lasting modifications to vortex shedding using a short plasma excitation. *Physical Review Letters*, 102(25), 2009.
- [28] J.M. Kay. Boundary-layer flow along a flat plate with uniform suction. *Reports and Memoranda*, 2628, 1948.
- [29] S.H. Kim and C. Kim. Separation control on naca23012 using synthetic jet. *Aerospace Science and Technology*, 13:172–182, 2009.
- [30] E. Koopmans and H.W.M. Hoeijmakers. Experimental research on flow separation control using synthetic jet actuators. 2014.
- [31] J.C. Lin. Review of research on low-profile vortex generators to control boundary-layer separation. *Progress in Aerospace Sciences*, 38:389–420, 2002.
- [32] J. Little, K. Takashima, M. Nishihara, I. Adamovich, and M. Samimy. Separation control with nanosecond-pulse-driven dielectric barrier discharge plasma actuators. *AIAA Journal*, 50(2):350–365, 2012.
- [33] E.C. Maskell. *A theory of blockage effects on bluff bodies and stalled wings in a closed wind tunnel*. Aeronautical Research Council, London: Her Majesty’s Stationery office., 1965.
- [34] R. Mittal and P. Rumpungnoon. On the virtual aeroshaping effect of synthetic jets. *Physics of Fluids*, 14, 2002.
- [35] E. Moreau, A. Debien, J.M. Breux, and N. Benard. Control of a turbulent flow separated at mid-chord along an airfoil with dbd plasma actuators. *Journal of Electrostatics*, 83:78–87, 2016.
- [36] D.J. Nani. Effect of orifice shape on synthetic jet efficiency. Master’s thesis, Utah State University, Logan, Utah, 2012.
- [37] V. Narayanaswamy, L.L. Raja, and N.T. Clemens. Control of unsteadiness of a shock wave/turbulent boundary layer interaction by using a pulsed-plasma- jet actuator. *Physics of Fluids*, 24, 2012.
- [38] F.T.M. Nieuwstadt. *Turbulentie: Theorie en toepassingen van turbulente stromingen*. Epsilon Uitgaven, Amsterdam, 4th edition, 2016.

- [39] S.H. Popkin, B.Z. Cybyk, H.B. Land, T.M. Emerick, C.H. Foster, and F.S. Alvi. Recent performance-based advances in sparkjet actuator design for supersonic flow applications. *51st Aerospace Sciences Meeting*, 2013.
- [40] S.H. Popkin, B.Z. Cybyk, H.B. Land, C.H. Foster, T.M. Emerick, and F.S. Alvi. Recent performance-based advances in sparkjet actuator design for supersonic flow applications. *AIAA*, 2013.
- [41] H. Schlichting. *Boundary-Layer theory*. McGraw-Hill, 6th edition, 1968.
- [42] A. Seifert, D Greenblatt, and I.J. Wygnanski. Active separation control: an overview of reynolds and mach numbers effects. *Aerospace Science and Technology*, 8:569–582, 2004.
- [43] A. Seifert and L.G. Pack. Oscillatory control of separation at high reynolds numbers. *AIAA Journal*, 37(9), 1999.
- [44] A. Seifert and L.G. Pack. Active flow separation control on wall-mounted hump at high reynolds numbers. *American Institute of Aeronautics and Astronautics*, 40(7):1363–1372, 2002.
- [45] D.M. Sharma. *Experimental Investigations of Dynamic Stall for and Oscillating Airfoil*. PhD thesis, Indian Institute of Technology, Kanpur, June 2010.
- [46] R.L. Simpson. Turbulent boundary-layer separation. *Annual Review of Fluid Mechanics*, 21(205–232), January 1989.
- [47] H. Tang, P. Salunkhe, Y. Zheng, J. Du, and Y. Wu. On the use of synthetic jet actuator arrays for active flow separation control. *Experimental Thermal and Fluid Science*, 57:1–10, 2014.
- [48] W. Tie, X. Liu, and S. Liu. Experimental study on the multichannel discharge characteristics of a multi-plasma-jet triggered gas switch. *IEEE Transactions on Plasma Science*, 43:937–943, 2015.
- [49] T. Van Buren, E. Whalen, and M. Amitay. Vortex formation of a finite-span synthetic jet: effect of rectangular orifice geometry. *Journal of Fluid Mechanics*, 745:180–207, 2014.
- [50] J.A. Vernet, R. Örlü, and P.H. Alfredsson. Separation control by means of plasma actuation on a half cylinder approached by a turbulent boundary layer. *Journal of Wind Engineering and Industrial Aerodynamics*, 145:318–326, 2015.
- [51] M. Watson, A.J. Jaworski, and N.J. Wood. A study of synthetic jets from rectangular and dual-circular orifices. *The Aeronautical Journal*, 2003.
- [52] Z. Xin, H. Yong, W. Xunnian, W. Wanbo, T. Kun, and L. Huaxing. Turbulent boundary layer separation control using plasma actuator at reynolds number 2000000. *Chinese Journal of Aeronautics*, 29(5):1237–1246, 2016.
- [53] D. You and P. Moin. Study of flow separation over an airfoil with synthetic jet control using large-eddy simulation. *Journal of Fluids and Structures*, 24:1349–1357, 2008.
- [54] S. Zhang and S. Zhong. An experimental investigation of turbulent flow separation control by an array of synthetic jets. *American Institute of Aeronautics and Astronautics*, 2010.
- [55] Z.B. Zhang, Y. Wu, M. Jia, H.M. Zhong, Z.Z. Sun, and Y.H. Li. Modeling and optimization of the multichannel spark discharge. *Chinese Physics*, 26(6), 2017.
- [56] Z.B. Zhang, Y. Wu, M. Jia, H. Zong, Z.Z. Sun, and Y.H. Li. The multichannel discharge plasma synthetic jet actuator. *Sensors and Actuators A: Physical*, 253:112–117, 2017.
- [57] Z.B. Zhang, Y. Wu, Z.Z. Sun, H.M. Song, M. Jia, H. Zong, and L. Yinghong. Experimental research on multichannel discharge circuit and multi-electrode plasma synthetic jet actuator. *Journal of Physics D: Applied Physics*, 50, 2017.
- [58] H. Zong and M. Kotsonis. Characterisation of plasma synthetic jet actuators in quiescent flow. *Journal of Physics D: Applied Physics*, 49, July 2016.

- 
- [59] H. Zong and M. Kotsonis. Electro-mechanical efficiency of plasma synthetic jet actuator driven by capacitive discharge. *Journal of Physics D: Applied Physics*, 49, 2016.
- [60] H. Zong and M. Kotsonis. Effect of slotted exit orifice on performance of plasma synthetic jet actuator. *Experiments in Fluids*, 58(17), 2017.
- [61] H. Zong and M. Kotsonis. Interaction between plasma synthetic jet and subsonic turbulent boundary layer. *Physics of Fluids*, 29(4), 2017.
- [62] H. Zong and M. Kotsonis. Realisation of plasma synthetic jet array with a novel sequential discharge. *Sensors and Actuators A*, 266, 2019.
- [63] H. Zong, Y. Wu, M. Jia, H.M. Song, H. Liang, Y.H. Li, and Z.B. Zhang. Influence of geometrical parameters on performance of plasma synthetic jet actuator. *Journal of Physics D: Applied Physics*, 49(2), 2015.
- [64] H. Zong, Y. Wu, H.M. Song, and M. Jia. Efficiency characteristic of plasma synthetic jet actuator driven by pulsed direct-current discharge. *AIAA Journal*, 54(11), 2016.